ADVANCED ENERGY MATERIALS
www.advenergymat.de

Sulfur Reduction Reaction in Lithium–Sulfur Batteries: Mechanisms, Catalysts, and Characterization

Lei Zhou, Dmitri L. Danilov, Fen Qiao, Junfeng Wang, Haitao Li, Rüdiger-A. Eichel, and Peter H. L. Notten**

Lithium–sulfur batteries are one of the most promising alternatives for advanced battery systems due to the merits of extraordinary theoretical specific energy density, abundant resources, environmental friendliness, and high safety. However, the sluggish sulfur reduction reaction (SRR) kinetics results in poor sulfur utilization, which seriously hampers the electrochemical performance of Li–S batteries. It is critical to reveal the underlying reaction mechanisms and accelerate the SRR kinetics. Herein, the critical issues of SRR in Li–S batteries are reviewed. The conversion mechanisms and reaction pathways of sulfur reduction are initially introduced to give an overview of the SRR. Subsequently, recent advances in catalyst materials that can accelerate the SRR kinetics are summarized in detail, including carbon, metal compounds, metals, and single atoms. Besides, various characterization approaches for SRR are discussed, which can be divided into three categories: electrochemical measurements, spectroscopic techniques, and theoretical calculations. Finally, the conclusion and outlook part gives a summary and proposes several key points for future investigations on the mechanisms of the SRR and catalyst activities. This review can provide cutting-edge insights into the SRR in Li–S batteries.

1. Introduction

The revival of electric vehicles and the implementation of wind and solar energies have increased demands for high-performance energy storage systems.[1–3] Currently, commercialized lithium-ion batteries with $LiCoO_2$ or $LiFePO_4$ cathodes suffer a relatively low energy density (200–300 Wh kg^{-1}) and safety hazards.[4] These drawbacks discourage practical applications of lithium-ion batteries on a large scale. Therefore, the development of rechargeable batteries with high energy density and reliability would be a priority. One of the most promising candidates is lithium–sulfur (Li–S) batteries, which have great potential for addressing these issues.[5–7] The conversion reaction based on the reduction of sulfur to lithium sulfides (Li_2S) yields a high theoretical capacity of 1675 mAh g^{-1} (S_8 + 16 Li = 8 Li_2S). Such a capacity is significantly higher than that of insertion cathode materials such as $LiCoO_2$ and $LiFePO_4$, which deliver capacities below 200 mAh g^{-1}. The 16-electron electrochemical charge transfer reaction with a working voltage of about 2.2 V allows a specific energy density of 2600 Wh kg^{-1} for Li–S batteries. With optimal configuration, a practical energy density of 500–600 Wh kg^{-1} would be achievable when considering additional battery components.[8] Moreover, sulfur possesses the merits of abundant resources, safety, and environmental friendliness. The breakthrough in Li–S batteries will promote the development and application of renewable energy.

Despite the great potential for replacing lithium-ion batteries, Li–S batteries still face several critical problems.[9] The principal one is the sluggish conversion kinetics of the sulfur reduction reaction (SRR) during discharging due to the low conductivity of sulfur species and complicated 16-electron conversion

L. Zhou, F. Qiao, J. Wang
School of Energy and Power Engineering
Jiangsu University
Zhenjiang 212013, China
E-mail: l.zhou@ujs.edu.cn

L. Zhou, D. L. Danilov, P. H. L. Notten
Department of Chemical Engineering and Chemistry
Department of Electrical Engineering
Eindhoven University of Technology
Eindhoven MB 5600, The Netherlands
E-mail: P.H.L.Notten@TUE.nl

The ORCID identification number(s) for the author(s) of this article can be found under https://doi.org/10.1002/aenm.202202094.

DOI: 10.1002/aenm.202202094

D. L. Danilov, Rüdiger-A. Eichel, P. H. L. Notten
Institute of Energy and Climate Research
Fundamental Electrochemistry (IEK-9)
Forschungszentrum Jülich
D-52425 Jülich, Germany

H. Li
Institute for Energy Research
School of Chemistry and Chemical Engineering
Jiangsu University
Zhenjiang 212013, China

Rüdiger-A. Eichel
Institute of Physical Chemistry
RWTH Aachen University
D-52074 Aachen, Germany

P. H. L. Notten
Centre for Clean Energy Technology
University of Technology Sydney
Broadway, Sydney, NSW 2007, Australia

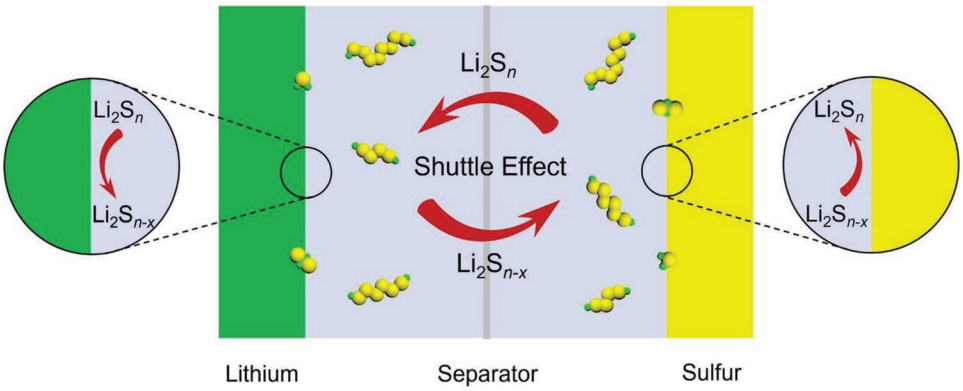

Figure 1. Schematic representation of the polysulfide shuttle effect in Li–S batteries.

process. SRR involves a series of phase transformations, i.e., the reduction from solid sulfur to various soluble intermediates and then to the final insoluble Li_2S_2/Li_2S products. The sluggish kinetics results in the inadequate reduction of sulfur during discharging, thus decreasing the specific capacity and rate capability of Li–S batteries. Another challenge is the dissolution and diffusion of lithium polysulfide intermediates (Li_2S_n, $3 \le n \le 8$) from cathodes to the electrolyte. The conversion reaction between sulfur and lithium generates various Li_2S_n that are soluble in common organic electrolytes. As illustrated in **Figure 1**, due to the electric field and concentration gradients, long-chain Li_2S_n ($6 \le n \le 8$) can penetrate through the separator and migrate to the anodes, where they will be reduced by lithium metal to form short-chain Li_2S_{n-x} ($2 < n-x < 6$) and insoluble Li_2S_2/Li_2S. This troublesome phenomenon causes two detrimental effects: 1) passivation of lithium anodes due to the deposition of an inactive Li_2S_2/Li_2S layer at the lithium surface; 2) accumulation of short-chain Li_2S_{n-x} at the passivated lithium anode. These short-chain polysulfides can diffuse back to the cathode and then react with long-chain Li_2S_n. This repeated process forms a shuttle effect, incurring rapid capacity decay and low Coulombic efficiency for Li–S batteries. Besides, lithium metal anodes also have critical challenges, such as severe side reactions and detrimental lithium dendrite growth. As this review focuses on the SRR at cathodes, lithium metal anodes have been published elsewhere, and are therefore not included here.[10–12]

Generally, the inadequate utilization of sulfur caused by the sluggish SRR kinetics aggravates the polysulfide shuttle. Tremendous efforts have been made to overcome these challenges over the past decades.[13–16] The groundbreaking research by Nazar and co-workers provided new insights into solving the problems of sulfur cathodes.[13] The introduction of mesoporous carbons (CMK-3) to sulfur cathodes as host material effectively constrained sulfur from diffusion and offered access to lithium ions for high reactivity with sulfur. This confinement ensured adequate redox reaction and enhanced sulfur utilization. From then on, materials with high confinement toward sulfur species have been developed as host, separator-modified layers, or additives for high-performance Li–S batteries.[17–19] However, the confinement strategy has not fundamentally resolved the sluggishness of the redox reaction and the shuttle effect since the confined polysulfides will accumulate in the cathode region, inevitably causing their diffusion to the anode side owing to concentration gradients in the electrolyte.

Therefore, accelerating the conversion kinetics of SRR has been proposed to be a promising strategy to achieve full utilization of sulfur cathodes. Catalyst materials, which can promote charge transfer and decrease the reaction energy barrier of sulfur cathodes, have shown great advantages in improving the SRR kinetics.[20–22] As a result, the polysulfide shuttle issue can be effectively addressed. However, although recent research on SRR has gained considerable achievements, the underlying conversion mechanisms are still elusive due to the complicated multistep electron transfer reaction. The catalytic effects on SRR for enhanced conversion kinetics should be further clarified, both from experimental and theoretical points of view. In addition, the structural evolution of sulfur species and catalyst activities during SRR should be accurately analyzed by proper characterization techniques, which allow to gain in-depth understanding of the SRR conversion mechanisms. It is therefore imperative to systematically summarize the fundamental reaction mechanisms, catalyst design, and characterization techniques to give a cutting-edge insight into SRR in Li–S batteries.

In this review, we focus on the critical issues of the SRR in Li–S batteries. The conversion mechanisms and reaction pathways of sulfur reduction will initially be introduced to give an overview of SRR. Then recent advances in catalyst materials that can accelerate the SRR kinetics are summarized, including carbon, metal compounds, metals, and single atoms. Besides, we discuss various characterization approaches used to evaluate the SRR kinetics in terms of electrochemical measurements, spectroscopic techniques, and theoretical calculations. Finally, the conclusion and outlook part provides a summary and proposes several key points for future investigations on the mechanisms of SRR and catalyst activities.

2. Mechanisms of Sulfur Reduction Reaction

2.1. General Principles of Li–S Batteries

The electrochemistry of Li–S batteries is based on the following reaction

$$S_8 + 16Li^+ + 16e^- \rightleftarrows 8Li_2S \quad (1)$$

where cyclo-S_8 (the thermodynamically stable form at room temperature) reacts with lithium ions and is reduced to Li_2S via a 16-electron pathway during discharging. The conversion mechanisms of SRR are rather complicated not only due to the multistep electron transfer but also because of the strong influence of the electrolyte system, e.g., the dielectric constant or donor number of solvents.[23] Although fundamental investigations on SRR have been carried out in different solvents[24–26] with various characterization techniques[27–30] and theoretical simulations,[31–35] the underlying mechanisms have still not been fully understood. In addition, as the Gibbs free energies of polysulfide intermediates are pretty close to each other, various chemical equilibrium reactions cause the coexistence of different sulfur species over a wide range of states-of-charge, resulting in the difficult detection of individual polysulfide (PS) species. Generally, as shown in **Figure 2**, the conversion mechanism of SRR according to the discharging curve of Li–S batteries can be summarized by two processes: the solid–liquid reduction from sulfur to polysulfides followed by liquid–solid Li_2S deposition. When considering the representative polysulfide species, the two processes can further be divided into four stages:

Stage I: two-electron reduction from S_8 to soluble long-chain Li_2S_8, corresponding to a solid–liquid two-phase reaction

$$S_8 + 2Li^+ + 2e^- \rightarrow Li_2S_8 \quad (2)$$

Stage II: a two-step reduction process of Li_2S_8 to soluble short-chain Li_2S_4, involving a liquid–liquid single-phase reaction, according to

$$3Li_2S_8 + 2Li^+ + 2e^- \rightarrow 4Li_2S_6 \quad (3)$$

$$2Li_2S_6 + 2Li^+ + 2e^- \rightarrow 3Li_2S_4 \quad (4)$$

Stage III: soluble Li_2S_4 is reduced to insoluble Li_2S_2 and Li_2S species at the long lower voltage plateau of about 2.1 V

$$Li_2S_4 + 2Li^+ + 2e^- \rightarrow 2Li_2S_2 \quad (5)$$

$$Li_2S_4 + 6Li^+ + 6e^- \rightarrow 4Li_2S \quad (6)$$

Stage IV: further reduction of Li_2S_2 to Li_2S suffers from a high polarization and slow redox kinetics due to the solid–solid transformation reaction, according to

$$Li_2S_2 + 2Li^+ + 2e^- \rightarrow 2Li_2S \quad (7)$$

Overall, the consecutive reduction of sulfur to Li_2S_2/Li_2S results in a gradually decreasing reaction kinetics. Especially for the deposition of insulating Li_2S, the conversion process becomes much more sluggish and higher overpotentials are needed. It is critical to seek solutions for accelerating the reaction kinetics and reducing the activation energy, which can achieve full utilization of sulfur cathodes. Catalysts for SRR have been proposed, which can block sulfur species from diffusion and regulate the reaction pathway to facilitate charge transfer.

2.2. Reaction Pathways of Sulfur to Polysulfides

The first discharging plateau of SRR involves the conversion of elemental sulfur to soluble polysulfides (including stages I and II). As the polysulfide species is dependent on the solvent system, the reaction pathway varies when choosing different solvents. By in operando UV–vis spectroscopy, Zou and Lu revealed major differences in the reaction pathways for high and low donor numbers (DNs) of solvents during sulfur reduction.[36] As shown in **Figure 3**a, the sulfur reduction mechanism in high DN solvents like dimethyl sulfoxide (DMSO) underwent multiple electrochemical and chemical reactions involving S_8^{2-}, S_6^{2-}, S_4^{2-}, and $S_3^{\bullet-}$ radicals. Among them, the most stable and dominant polysulfide intermediate was $S_3^{\bullet-}$. By contrast, in the low DN solvent, for instance, the mixed

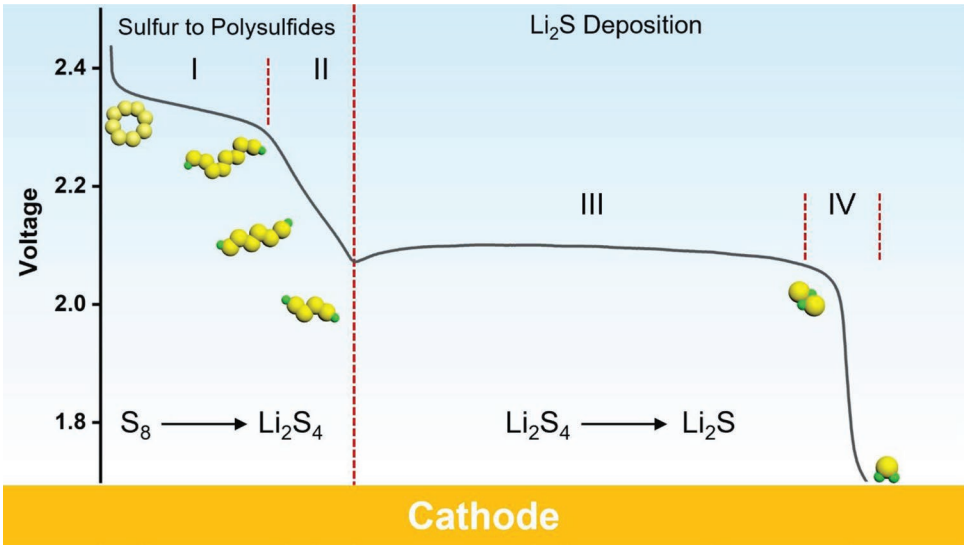

Figure 2. Schematic representation of the conversion mechanism of SRR during discharging.

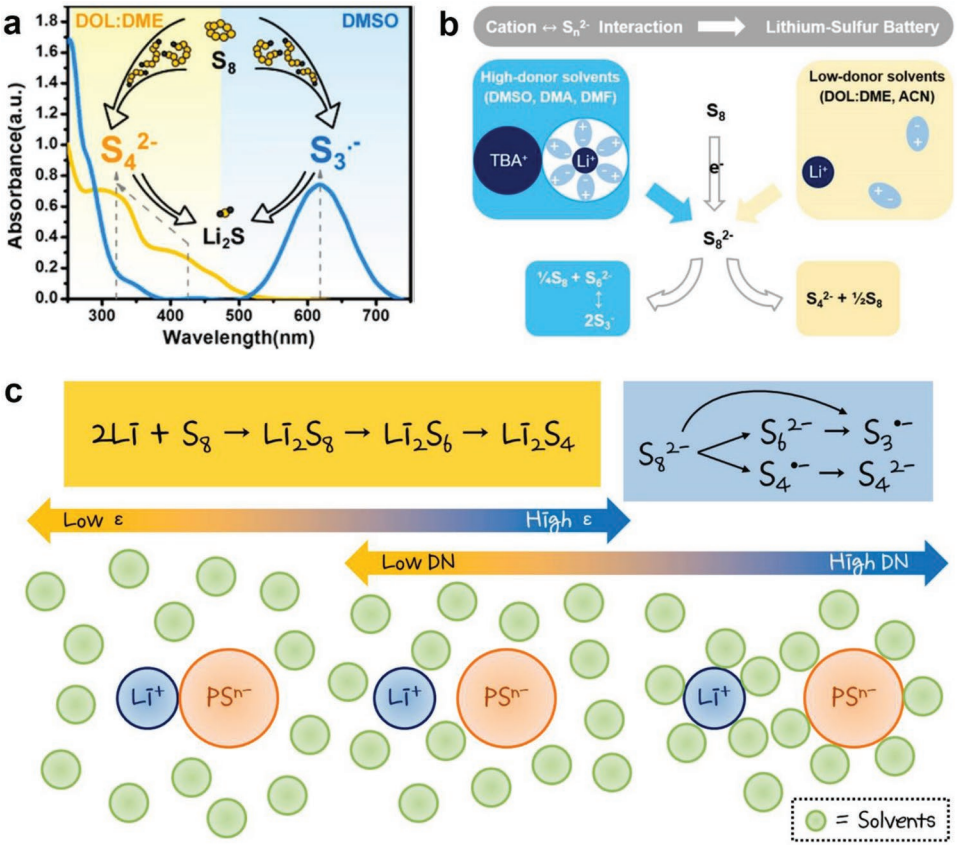

Figure 3. a) UV–vis spectra of S_4^{2-} and $S_3^{\bullet-}$ radicals in DOL:DME (1:1) and DMSO. Reproduced with permission.[36] Copyright 2016, American Chemical Society. b) Summary of how polysulfide stability/speciation is affected by its interaction with cations and solvent molecules. Reproduced under the terms of the CC-BY license.[23] Copyright 2018, The Authors, Published by ECS. c) Schematic representation of solvent interaction with polysulfide species and the corresponding reduction reaction mechanisms in different solvent systems. Reproduced under the terms of the CC-BY license.[32] Copyright 2020, The Authors, Published by MDPI.

solvent system, 1,3-dioxane:1,2-dimethoxyethane (DOL:DME), the dominant species was S_4^{2-}. Solvents with high DN can stabilize $S_3^{\bullet-}$, significantly reducing the electrode polarization and improving the reaction kinetics of Li–S batteries. Furthermore, they investigated the correlation between solvent properties and Li–S redox chemistry in nine nonaqueous electrolyte solvents involving three main properties, the dielectric constant (ε), DN, and acceptor number (AN).[23] Various analytical techniques demonstrated that the reduction potential of S_8 increased with increasing AN of solvents, which could be attributed to the higher solvation energy of S_8^{2-} in high-AN solvents. The interaction between the cation complex and polysulfide anions was found to be the most critical factor which affected the stability and speciation of polysulfides (Figure 3b). This can be regulated by the donicity of solvents, and concentration and type of cations in Li–S batteries.

Du et al. investigated the solvent-dependent polysulfide reduction mechanism in Li–S batteries using density functional theory (DFT) methods.[32] They illustrated that the DN and ε of the solvent system had a considerable effect on the stability of different polysulfide intermediates, which is summarized in Figure 3c. Generally, solvents with both high DN and ε were more beneficial to the dissociated polysulfide anions than to the bound polysulfides, and vice versa. A low DN but high ε solvent, such as acetone, favored the coexistence of the dissociated and bound states in chemical equilibrium. The coordination and solvation of polysulfides will determine the dominant species.

It is generally considered that the first step of SRR in high-dielectric solvents is based on Equation (2) (S_8 to S_8^{2-}), which can be explained by the two successive one-electron reduction steps and the two-electron reduction reaction.[27] However, the underlying mechanism is still debatable due to the lack of direct and clear experimental evidence. By in situ derivatization methods with high-performance liquid chromatography (HPLC), Zheng et al. found that the major polysulfide intermediates produced from the initial sulfur reduction were the S_4^{2-} and S_5^{2-} species, while the widely accepted reduction products of S_8^{2-} and S_6^{2-} were formed by the subsequent chemical reactions with elemental sulfur.[30] Based on the in situ analyses, the first step of SRR may involve multiple parallel pathways and the S—S bond cleavage with electron transfer. The complexity of the sulfur reduction to polysulfides indicates that a better understanding of the mechanism still needs more detailed characterization and studies.

Due to the close Gibbs free energies, various polysulfide intermediates, such as S_7^{2-}, S_5^{2-}, and $S_3^{\bullet-}$, experience many disproportionation or comproportionation reactions, which

can simultaneously exist in the electrolyte. A standard solution with specific polysulfide species is hard to obtain, which poses difficulties in studying the sulfur reduction mechanisms. Based on the unstable properties of polysulfide species, HPLC has been employed to analyze polysulfide ions quantitatively and qualitatively, and electron spin resonance (ESR) spectroscopy offers reliable approaches to identify the possible formation of polysulfide radicals during SRR.[37] Combining HPLC with UV–visible absorption and ESR, Barchasz et al. investigated the electrolyte composition at different discharge potentials in a tetraethylene glycol dimethylether-based electrolyte.[38] The authors proposed a possible mechanism for SRR with a three-step process. The first step involved the slow reduction of elemental sulfur to S_8^{2-}, while S_8^{2-} was not stable in the electrolyte and may rapidly convert to S_6^{2-} and S_5^{2-} under disproportionation. In the second step, S_6^{2-} involved two (electro)chemical equilibriums, resulting in the formation of S_4^{2-} ions and $S_3^{\bullet-}$ radicals, respectively. Finally, HPLC results indicated that the gradual reduction produced short-chain polysulfides. S_3^{2-}, S_2^{2-}, and S^{2-} were identified, which was due to electrochemical and disproportionation reactions.

By monitoring the real-time changes in sulfur and polysulfide species during discharging and charging, the SRR mechanism can be well recognized. Zheng et al. proposed another three-step reduction mechanism based on quantitative HPLC methods, which included two chemical equilibrium reactions.[39] When discharging started, sulfur was reduced to long-chain polysulfides (mainly S_7^{2-}, S_6^{2-}, and S_5^{2-}), while S_8^{2-} was produced from the subsequent reaction between sulfur and polysulfides. A chemical equilibrium occurred between S_7^{2-}, S_6^{2-}, and S_5^{2-}. The reduction potential started decreasing until the significant consumption of S_7^{2-} and S_6^{2-} at about 2.3 V. During the following reaction process from 2.3 to 2.1 V, a sloped discharge profile indicated that almost all the polysulfides S_n^{2-} with $4 \le n \le 7$ coexisted in the electrolyte. Since the polysulfide concentration varied independently in this stage, no apparent equilibrium was not observed. At about 2.1 V, the second reduction plateau emerged and almost all the polysulfides S_n^{2-} with $n \ge 6$ were consumed. In this reduction process, the reduction rates of S_5^{2-}, S_4^{2-}, and S_3^{2-} maintained almost the same, indicating the presence of a chemical equilibrium between these three species. Although the concentration ratio of the three polysulfides was nearly unchanged during the reduction stage, the total amount of polysulfides decreased, implying the formation of insoluble Li_2S_2/Li_2S. Besides, Kawase et al. investigated the conversion of polysulfides in Li–S batteries using LC/mass spectrometry (MS) and NMR combined with an organic conversion technique.[40] They revealed that the reduction proceeded via four distinct stages. The second discharge plateau was the most important step, dominated by the Li_2S_3 reduction. The results also indicated that the long-chain polysulfides S_n^{2-} with $6 \le n \le 8$ were responsible for the shuttle effect, causing serious capacity decay of sulfur cathodes.

Vijayakumar et al. studied the dissolution mechanisms and chemical stability of polysulfide species in an aprotic solvent medium combining experimental and computational analyses.[41] Multinuclear NMR, variable temperature ESR, and sulfur K-edge X-ray absorption spectroscopy (XAS) analyses revealed that the first step in the dissolution process involved the lithium exchange between polysulfides and solvent molecules. Due to the lithium exchange, delithiated polysulfides S_6^{2-} were generated, resulting in the formation of highly reactive $S_3^{\bullet-}$ radicals through dissociation reactions. It was concluded that the polysulfide shuttle may include $S_3^{\bullet-}$ radicals which caused parasitic reactions with the lithium anode. Furthermore, to understand the reaction pathways of sulfur species during discharging and charging, Wang et al. used the in situ electron paramagnetic resonance (EPR) technique to directly monitor the formation and evolution of $S_3^{\bullet-}$ radicals during the electrochemical process.[42] It was found that $S_3^{\bullet-}$ radicals changed periodically at different potentials, implying the temporal equilibrium among different polysulfides, instead of generating an individual polysulfide. The chemical and electrochemical reactions in Li–S batteries drove each other to proceed via sulfur radicals, resulting in two completely different reaction pathways during discharging and charging.

2.3. Reaction Pathways of Li_2S Deposition

The Li_2S deposition in SRR corresponds to the second discharging plateau (stages III and IV), which contributes to the whole capacity of 75% of sulfur cathodes. Owing to the insulating nature of Li_2S, this reduction process needs to overcome huge energy barriers with high overpotentials, resulting in rather sluggish reduction kinetics. In addition, the uneven Li_2S deposit may be detached from the cathode side, forming electrically isolated and dead Li_2S. The control of Li_2S deposition in accelerated and uniform ways is the key to achieving full sulfur utilization. Theoretical calculations, modeling, and experimental analyses have been carried out to reveal the mechanism of Li_2S deposition and the dependence on electrode substrates.[31,35,43–45] The Li_2S deposition is also affected by the solvent systems. Cuisinier et al. reported a Li_2S deposition mechanism in electron-pair donor electrolytes with the partial solvation of Li_2S.[46] Pan et al. found that the deposition morphology of Li_2S varied along with the donor numbers of solvents.[47] Flower-like Li_2S, Li_2S films, and small Li_2S particles were formed in solvents with medium-DN, low-DN, and high-DN, respectively.

Chiang and co-workers systematically investigated the mechanism of Li_2S deposition in Li–S batteries combining the kinetic analyses and direct observations of the Li_2S morphology by electron microscopy at various stages of deposition.[48] Glyme-based Li_2S_8 solutions were employed to carry out the Li_2S deposition onto carbon substrates. Based on the morphological and kinetic observations, the authors proposed a mechanism for Li_2S growth, as illustrated in **Figure 4**a. The Li_2S deposition was dominated by a 2D island nucleation and growth process at the three-phase boundary between the precipitate, substrate, and electrolyte, as the low conductivity of Li_2S failed to allow the growth along the outer surface. This fact meant that the growth of Li_2S in the thickness direction could not occur by bulk chemical diffusion. The nucleation and growth of Li_2S occurred at different overpotentials (Figure 4b). The nucleation of Li_2S needed a higher driving force than growth, as the surface energy barriers must be overcome. For different solvent systems, the nucleation overpotential may

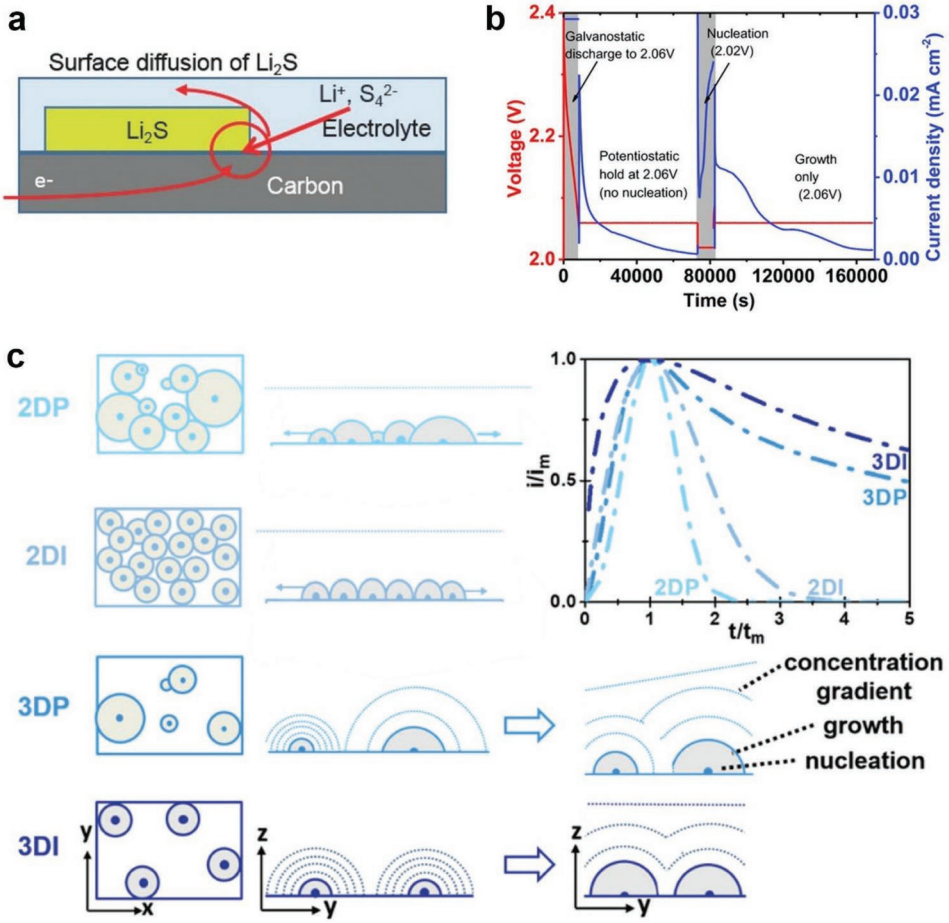

Figure 4. a) Proposed mechanism for the reduction of polysulfides at the three-phase boundary between carbon, Li_2S, and electrolyte. b) Current density and voltage versus time. Reproduced with permission.[48] Copyright 2015, Wiley-VCH. c) Schematic illustration of 2DP/2DI (BFT models) and 3DP/3DI (SH models) (*x*–*y* is parallel to the substrate; *y*–*z* is vertical to the substrate). Reproduced with permission.[50] Copyright 2019, Wiley-VCH.

vary. Furthermore, they found that the Li_2S precipitation morphologies varied according to the current. Specifically, at high currents, high overpotentials generated a high nuclei density, resulting in a continuous Li_2S morphology composed of many small crystallites. Low currents produced fewer but larger Li_2S precipitates. Therefore, high storage capacities via Li_2S precipitation can be achieved by regulating the conductive substrate, solvent species, and overpotential for nucleation and growth. Followed by this work, the authors further quantified the effects of the electrolyte/sulfur (E/S) ratio on the kinetics of the Li_2S deposition process.[49] At higher polysulfide concentrations, Li_2S deposition became remarkably sluggish with island nucleation and growth rates up to 75% less than at low concentrations. The slower electrodeposition kinetics resulted in significantly higher polarization and lower capacity and rate capability in Li–S batteries with reduced electrolytes.

Li et al. developed quantitative solvent-mediated Li_2S growth models.[50] The authors revealed three solvent properties and their role in the Li_2S deposition: 1) donicity, which governed the stability of the polysulfide anions through Li^+–polysulfide interactions; 2) polarity (dielectric constant), which governed the solvation ability of the final product Li_2S; 3) viscosity, which strongly affected the diffusivity of polysulfide and dissolved Li_2S. Four classical models were considered to fit the current–time responses of the Li_2S deposition (Figure 4c): i) 2D progressive nucleation (2DP) or ii) 2D instantaneous (2DI) nucleation, based on Bewick, Fleischman, and Thirsk (BFT) models, which were followed by the incorporation of adatoms into the lattice interface; iii) 3D progressive (3DP) nucleation or iv) 3D instantaneous (3DI) nucleation, based on Scharifker–Hills (SH) models, which were followed by a volume diffusional controlled growth. According to the four models, the peak fitting of the current–time transient profiles indicated that Li_2S deposition in glyme-based and high-donicity solvents followed the 2DI and 3DP models, respectively. Therefore, the nucleation rate of Li_2S in glyme-based electrolytes was higher than that in high-donicity solvents (instantaneous vs progressive). The Li_2S growth was governed by surface diffusion of adatoms and bulk diffusion of precursors in glyme-based and high-donicity solvents, respectively. The Li_2S solubility was higher in high-donicity solvents than in glyme, which meant that the diffusion of solvated Li_2S increased in the solution before precipitating onto the Li_2S clusters along the 3D directions. However, the extremely low solubility of Li_2S in glymes caused the instant precipitation on the substrate of the generated Li_2S, hampering the further growth by the lattice incorporation of

adatoms nearby. Such Li_2S growth models can serve as a guide to searching for new and efficient electrolytes for Li–S batteries.

3. Catalysts for Sulfur Reduction Reaction

Considering the conversion mechanisms of SRR discussed above, the role of catalysts for SRR is to 1) effectively adsorb sulfur species at the surface and 2) decrease the reaction activation energy. Adsorption (physical adsorption and chemical adsorption) and catalysis are critical to mitigating the shuttle effect and accelerating the conversion kinetics. Specifically, physical adsorption involves weak van der Waals forces, while chemical adsorption involves chemical bonding. The chemical adsorption of materials, e.g., sulfur host, toward sulfur species indicates the formation of chemical bonding at the interface. Such interaction effectively anchors sulfur species at the surface of host materials, which is beneficial in preventing polysulfides from dissolving and diffusing into the electrolyte. However, chemical adsorption is typically considered to anchor sulfur species thermodynamically. It does not involve changing the reaction kinetics of sulfur species. In other words, chemical adsorption alone cannot accelerate the redox conversion of sulfur species. Regarding catalysis, it is a process that alters the rate of chemical reactions by catalysts. Catalysis can change the reaction pathways and activation energies of SRR, usually accelerating the reaction kinetics.

Chemical adsorption has strong connections with catalysis in Li–S batteries. Catalysis typically involves a series of processes, including mass transfer of reactants, chemical adsorption, charge transfer, and desorption. Since the electrocatalytic SRR occurs at the interface between sulfur species and catalysts, in which sulfur species are adsorbed at the surface of catalysts. Proper chemical adsorption is therefore a necessary step for the catalytic conversion of sulfur species. In this case, chemical adsorption is a critical prerequisite for sulfur utilization in high-performance Li–S batteries. To estimate a catalyst for SRR, the binding energy of catalysts toward sulfur species has been considered a key parameter for efficient SRR kinetics, which has been examined by experimental and theoretical methods.

Based on these analyses, the design of high-performance catalysts for SRR should meet the following criteria. 1) Good electrical conductivity for fast charge transfer: as sulfur and discharging products Li_2S_2/Li_2S are electronically insulated, catalysts with high electrical conductivity are needed, which provide rapid access to electron/ion transport and benefit the effective deposition of solid products. 2) Proper adsorption toward sulfur species for anchoring them within the cathode: sulfur species should be effectively adsorbed at the surface of catalysts to mitigate the shuttle effect and proceed with catalytic reactions. 3) Abundant active sites for accelerating sulfur conversion kinetics: catalysts need to offer adequate active sites to enhance catalytic activities and efficiency. This property will reduce the amount of used catalysts, increase the energy density of batteries, and help the uniform deposition of discharging products. 4) High structural stability for prolonged use: catalysts should maintain intrinsic stability during the reactions to achieve the long-term catalytic effects on SRR. 5) Low cost for large-scale applications: low-cost catalytic materials are desirable, like carbon and oxides, since they enhance the potential for commercialization of future Li–S batteries. It is challenging to find SRR catalysts that can meet all five criteria, especially when the research on electrocatalytic SRR is still in its infancy. However, research has been done to develop different materials that have catalytic activities with respect to the SRR.

3.1. Carbon

Carbon materials, such as porous carbon, graphene, and carbon nanotubes (CNTs), possess excellent physical, chemical, and mechanical properties. The high electrical conductivity and large specific surface area allow their applications in Li–S batteries for enhanced charge transfer and polysulfide confinement.[13,51,52] However, two main defects of carbon prevent them from improving the SRR kinetics. Due to the weak polarity of pure carbon materials, they can only confine sulfur species by physical blocking instead of chemical adsorption, which means that the diffusion of polysulfides cannot be fully eliminated. The intrinsic chemical inertness of carbon atoms impedes catalytic activities. Therefore, carbon alone fails to accelerate the SRR kinetics. An alternative is to modulate the electronic structure of carbon materials either by decorating functional groups or by so-called heteroatom doping. Especially, the introduction of nonmetal heteroatoms, such as N, P, B, and S, has been demonstrated to significantly improve the SRR kinetics, despite the underlying mechanism still being indefinite.[53–56] Early research generally focused on the adsorption ability between sulfur species and heteroatom-doped carbon materials. Currently, increasingly clear evidence reveals that heteroatom-doped carbon materials possess catalytic effects on SRR.[16] This fact can be demonstrated by experimental and theoretical results (e.g., the change in reaction overpotential, activation energies, and pathways). **Table 1** summarizes the electrochemical performance of Li–S batteries based on various doped carbon materials.

N-doped carbon materials, such as N-doped porous carbon,[57,58] N-doped graphene,[59] and N-doped carbon fibers,[60] have been reported for enhanced SRR kinetics. N-doping enhances the electrical conductivity and chemical adsorption toward polysulfides, promoting the convention kinetics of sulfur species through catalytic effects. Du et al. reported N-doped carbon nanocages with hierarchical structures for enhanced sulfur utilization.[61] The N-doped sp^2-carbon catalyzed the sulfur conversion reactions. That was concluded from Tafel plots and DFT calculations. The calculated free energy profiles of the sulfur reduction process were compared between the isolated state and the adsorbed states on six typical configurations of pyridinic N@zigzag edge, pyridinic N@armchair edge, graphitic N, zigzag edge, armchair edge, and graphite plane. In the adsorbed states, the reduction from sulfur to Li_2S_2 revealed decreased free energy profiles. The conversion from Li_2S_2 to Li_2S was also exothermic for the pyridinic N@zigzag edge, implying the promoted catalytic effects on Li_2S deposition. The high N-doping content will increase the active sites, improving the adsorption and catalysis effects on sulfur species. This phenomenon has been validated by Xu et al., who designed a N-doped carbon/graphene (NC/G) sheet

Table 1. Summary of doped carbon catalysts increasing the performance of Li–S batteries.

Catalysts	Sulfur content[a)] [wt%]	Sulfur loading [mg cm^{-2}]	Current rate [C]	Cycle number	Initial capacity [mAh g^{-1}]	Retained capacity [mAh g^{-1}]	Refs.
N, S-doped carbon	67	4.0	1.0	500	≈800	≈700	[16]
N, S-doped carbon	60	1.6–2.0	0.2	100	1372	891	[53]
			2.0	500	975	647	
P-doped carbon foam	56	–	1.0	1500	1072	432	[54]
B, N-doped graphene	–	1.4–1.6	0.2	80	1133	977	[56]
			2.0	700	855	387	
N-doped carbon sphere	56	2.0	0.1	50	1535	≈1400	[57]
			1.0	1000	1104	647	
N-doped porous carbon	43	1.2	0.2	300	1535 (0.1 C)	718	[58]
N-doped graphene	48	1.3–1.5	0.2	200	1296	770	[59]
			0.5	500	920	503	
N-doped carbon fiber	70	7.0	1.0	600	738	609	[60]
N-doped carbon	60	0.8	1 A g^{-1}	100	1400	1058	[61]
			10 A g^{-1}	1000	≈800	438	
N-doped carbon	56	1.0	0.2	100	1380	980	[62]
			2.0	500	885	721	
N-doped carbon	51	1.0	0.1	100	1410	1338	[63]
			1.0	1000	1250	1003	
N, O, S-doped carbon	54	1.1	0.5	400	1122	754	[64]
		2.7	0.2	100	2.9 mAh cm^{-2}	2.0 mAh cm^{-2}	
N, O-doped carbon	53	1.5	0.2	200	1123	794	[65]
			1.0	800	863	467	
N, O-doped carbon	69	2.0	1.0	500	≈1000	481	[66]
		7.4	0.2	50	7.35 mAh cm^{-2}	≈5.3 mAh cm^{-2}	
O-doped carbon	64	1.5	0.1	100	1385	925	[67]
			2.0	1000	≈550	375	

[a)]Sulfur content in cathodes.

with a N-content of 17.1% as sulfur host materials.[62] Benefiting from the high electrical conductivity and good chemical adsorption, NC/G showed fast catalytic conversion of polysulfides. The energy barrier for the conversion of Li_2S_2/L_2S products has been significantly reduced. The sulfur composite cathode delivered a capacity of 721 mAh g^{-1} after 500 cycles with a capacity decay of only 0.037% per cycle at 2.0 C. Another pomegranate-like sulfur-/N-doped carbon composite structure (S@N−C@N−C nanosheets (NSs)) has been designed to expedite the solid–solid conversion of Li_2S_2 to Li_2S.[63] An ultralow capacity decay rate of about 0.016% per cycle over 1000 cycles at 4.0 C was achieved.

Dual doping or multiple doping would reveal more catalytic activities for SRR.[64–66] Peng et al. systematically investigated the SRR kinetics from an electrocatalytic point of view.[16] As shown in **Figure 5**a, the initial reduction of sulfur to soluble polysulfides needed relatively low activation energies, implying an easy conversion process. Nonetheless, the following conversion to Li_2S_2/Li_2S suggested increased activation energies with more sluggish kinetics. The authors built a model system comprising heteroatom-doped holey graphene framework (HGF) electrocatalysts to regulate the SRR kinetics. N, S-HGF displayed the improved catalytic activities for SRR, which exhibited a higher exchange current density, larger electron transfer number, lower charge transfer resistance, and lower activation energies compared with nondoped or single-doped counterparts (Figure 5b–e). The larger electron transfer number from N, S-HGF catalysts implied a faster sulfur reduction and rapid conversion from polysulfides to the final discharging products. By contrast, sulfur was reduced to a mixture of long- and short-chain polysulfides by single-doped catalysts, and the main reduction products in the pristine HGF catalyst system was determined to be Li_2S_4.

To better understand the fundamental origin of the SRR catalytic activities by heteroatom-doped HGFs, DFT calculations have been performed to elucidate the heteroatom doping effects on their catalytic activity. The analyses indicated that the carbon atoms adjacent to the heteroatoms would be the optimal adsorption sites and most probable catalytic sites for SRR due to the redistributed charge induced by the heteroatoms. The reduction of Li_2S_2 to Li_2S with high activation energies was assumed to be the rate-determining step involving the formation of LiS radicals. A volcano plot in Figure 5f represents the relationship between the overpotential and the adsorption energies of LiS radicals. The N, S dual doping pushed the N, S-HGF system nearly to the top of the volcano plot with negligible

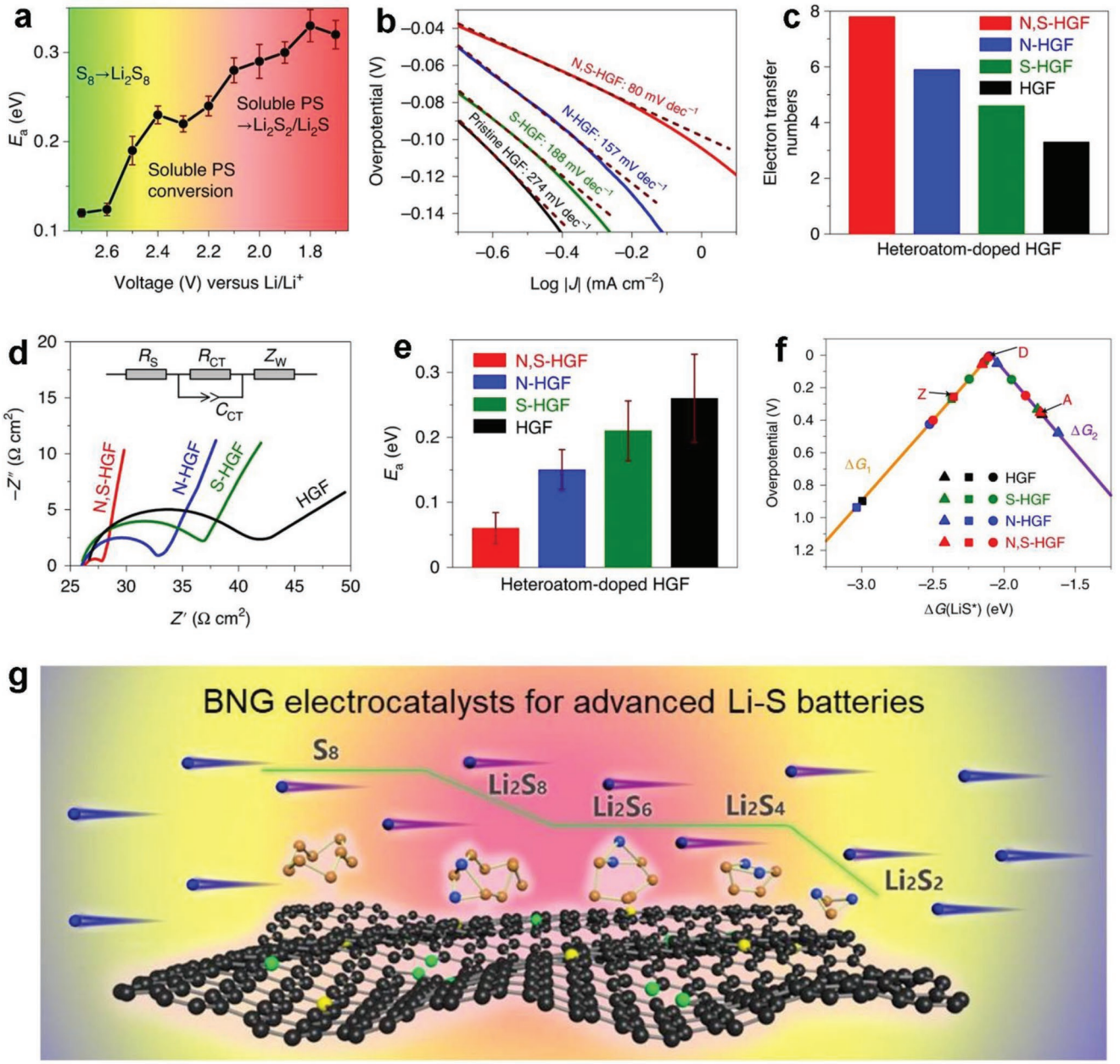

Figure 5. a) Activation energy profiles at various voltages. b) Tafel plots of heteroatom-doped HGFs. c) An electron transfer number comparison among heteroatom-doped HGFs. d) Electrochemical impedance spectroscopy of heteroatom-doped HGFs in SRR. e) Activation energies for the SRR process among various heteroatom-doped HGFs at the onset potential. f) Volcano plot linking the overpotential to the adsorption energies of LiS radicals at different active sites. Reproduced with permission.[16] Copyright 2020, Springer Nature. g) Schematic illustration of BNG electrocatalysts applied for advanced Li–S batteries. Reproduced with permission.[56] Copyright 2022, Elsevier.

overpotentials. This study indicates that heteroatom doping is a promising strategy to address the sluggish SRR kinetics.

Another dual-doping graphene containing heteroatoms of B and N has been developed as bifunctional mediator for durable Li–S batteries. Ci et al. realized the controllable synthesis of 3D B/N dual-doped graphene (BNG) particles with sulfiphilic and lithiophilic features.[56] As the separator modified layers, BNG mitigated the polysulfide shuttle effect and suppressed dendritic growth at lithium anodes. BNG offered a convenient platform to clarify sulfur and lithium electrochemistry (Figure 5g). The polysulfide adsorption implied that the incorporated B and N into graphene further augmented the adsorption energies compared with their single-doped counterparts. Moreover, the Bader charge analysis indicated that N atoms gained more charge in the dual-doped systems, resulting in stronger interaction with polysulfides. The catalytic effects were experimentally confirmed by Li_2S deposition tests. The nucleation capacity of BNG–carbon paper (CP)-based cells was larger than BG–CP, NG–CP, G–CP, and bare CP counterparts. The assembled BNG-based batteries with a high sulfur loading of

5.6 mg cm^{-2} and a low E/S ratio of 5 µL mg^{-1} delivered a high areal capacity of 5.4 mAh cm^{-2}.

Compared with N- and S-doping, P-doping owns unique properties, since the valence electrons of P atoms display lower ionization energy, allowing a higher electron-donating ability. Besides, P-doping will produce structural defects in the carbon lattice due to the larger atomic diameter. These characteristics ensure that P-doping in carbon has good adsorption and catalysis effects on sulfur species. Zou et al. proposed a template-free strategy to fabricate P-doped carbon foam (PCF), which presented superior adsorption and catalytic conversion abilities to polysulfides.[54] The introduction of the P-dopant significantly tailored the electronic structure and chemical activity of the carbon skeleton, expediting the sulfur conversion kinetics. When used in sulfur cathodes, PCF accelerated the lithium diffusion and alleviated the polarization. P-doped carbon was also used as interlayer for Li–S batteries.[55] A flexible cell can deliver a stable specific capacity of 850 mAh g^{-1} over 100 cycles, corresponding to high gravimetric and volumetric energy densities of 387 Wh kg^{-1} and 395 Wh L^{-1} on cell level, respectively. Besides, O-doped carbon has also been reported as catalyst for Li–S batteries.[67]

3.2. Metal Compounds

Metal compounds, such as oxides,[68] sulfides,[69] and nitrides,[70] have been extensively studied to chemically anchor sulfur species by polar–polar or redox interactions. Their structural characteristics like high polarity and abundant active sites enable the effective mitigation of shuttle effects and accelerate the electrochemical charge transfer kinetics of sulfur cathodes. Considering the favorable conductivity and support function of carbon, metal compounds are often integrated with various carbon nanostructures, such as graphene and CNT, to enlarge the catalytic activities of SRR. A summary of the battery performance based on metal compounds is presented in **Table 2**.

3.2.1. Oxides

Oxides for enhanced SRR kinetics were initially revealed by Nazar and co-workers, who mediated the polysulfide redox reaction by insoluble thiosulfate species in a two-step process.[71] The ultrathin MnO_2 nanosheet host first reacted with the produced polysulfides to form surface-bound thiosulfate groups. When the reduction proceeded further, the surface thiosulfate groups anchored the newly produced polysulfides and converted them into lithium sulfides. MnO_2 nanosheets not only anchored polysulfides but also promoted the conversion process, which can therefore also be considered as catalysts for SRR. This work gives a new insight into the complex Li–S electrochemistry. From then on, research on accelerated sulfur conversion kinetics has been successively performed on various oxides, including VO_2,[72] Co_3O_4,[73] Fe_3O_4,[74] Fe_2O_3,[75] $ZnFe_2O_4$,[76,77] $CuFe_2O_4$,[78] SnO_2,[79] ZnO,[80] and CoOOH.[81]

Based on the structural analyses, Wang et al. found that paramontroseite VO_2 had good electrical conductivity at room temperature, which would benefit the reaction kinetics of sulfur cathodes.[72] The introduction of VO_2 to Li–S batteries gave rise to a similar mechanism as Nazar and co-workers' report on MnO_2, catalyzing the sulfur conversion.[71] By intercalating Li ions into tetrahedral V_2O_5, Yang et al. developed a ω-$Li_3V_2O_5$ (ω-LVO)/carbon nanotube macrofilm (CMF) catalytic network for enhanced SRR kinetics.[82] Compared with typical V_2O_5, the ω-LVO network contained multiple centers of polarity trapping polysulfides, allowing Li (0.51 eV) and V (0.57 eV) with strong positive electrical potentials to anchor the sulfur in polysulfides, and O (–0.57 eV) with a strong negative electrical potential to absorb the lithium from polysulfides. As catalytic interlayer for Li–S batteries, the ω-LVO/CMF demonstrated excellent sulfur conversion effects. As shown in **Figure 6**a–f, the electrolyte for the cathodes with ω-LVO/CMF interlayer exhibited the darkest color from 2.30 to 2.10 V and was significantly decolored in the further reduction process (Figure 6c). The color change implies that the ω-LVO/CMF interlayer accelerated sulfur reduction to polysulfides and finally to solid lithium sulfides. This fact was further confirmed by the synchronous ultraviolet–visible spectrophotometry (UV–vis), which indicated a considerable blueshift for the electrolyte for the cathodes with ω-LVO/CMF. In addition, the ω-LVO/CMF interlayer resulted in the smallest Tafel slopes for the two reduction plateaus of sulfur cathodes among the three battery configurations. The electron transfer number calculated from the Koutecky–Levich plots was 14.1, which was close to the theoretical value of 16 for the redox reaction of Li–S electrochemistry. These advantages successfully enabled a 750 mAh pouch cell with low internal resistance, high-rate capability, and a long lifespan for practical applications.

By investigating the electronic structures of various sulfur species involved in Li–S batteries, Liu et al. constructed an electronic energy diagram to illustrate the reaction pathways and reveal the origin of the sluggish reaction kinetics at a molecular level (Figure 6g,h).[83] Based on DFT calculations, they proposed that Nb_2O_5 can work as electron–ion reservoirs to regulate the SRR process. During discharging, the lithium intercalation reaction of Nb_2O_5 converting to $LiNb_2O_5$ can provide electrons and Li^+ cations to the sulfur species, prompting the conversion from polysulfides to Li_2S_2/Li_2S. Iron oxides were also investigated for SRR applications. The fabrication can be direct pyrolysis of Fe-based metal–organic frameworks (MOFs), which resulted in carbon-encapsulated Fe_3O_4@C composites.[74] Alternatively, Fe_2O_3 nanocrystals were in situ grown on graphene by hydrothermal methods.[75] The introduction of carbon increases the number of active sites at iron oxides, catalyzing the reduction of sulfur.

As SRR involves complicated solid–liquid–solid phase transition processes, selective catalysis for the conversion reactions would be a favorable strategy to mitigate the polysulfide shuttle, which was proposed by Hua et al.[84] The authors used indium oxide nanoparticles as a proof-of-concept catalyst (In-based catalyst) to demonstrate the selective catalysis for SRR. The In-based catalyst with strong adsorption toward sulfur decelerated the solid–liquid reduction of sulfur to soluble polysulfides, but it accelerated the liquid–solid conversion with the enhanced Li_2S deposition. In this case, the accumulation of soluble polysulfides in the electrolyte was fundamentally reduced, thus preventing the shuttle effect. The selective catalysis was

Table 2. Summary of metal compound catalysts increasing the performance of Li–S batteries.

Catalysts	Sulfur content[a)] [wt%]	Sulfur loading [mg cm^{-2}]	Current rate [C]	Cycle number	Initial capacity [mAh g^{-1}]	Retained capacity [mAh g^{-1}]	Refs.
Fe_2O_3	68	1.0–1.4	2.0	1600	818	491	[75]
$ZnFe_2O_4$	56	1.4	0.5	300	860	613	[77]
CoOOH	49	1.0–3.0	1.0	450	616	502	[81]
ω-$Li_3V_2O_5$	80	2.5	3.0	500	≈800	771	[82]
$NiMoO_4$	–	2.0	1.0	500	682	654	[86]
FeS	53	≈1.0	2.0	500	596	560	[96]
MoS_2	–	10	0.1	200	1181	1137	[98]
			1.0	500	~900	540	
B-doped MoS_2	56	≈1.5	0.2	100	1228	1035	[102]
			5.0	1300	726	537	
Co_3S_4	74	7.4	5.0	1000	850	720	[96]
V_5S_8	66	≈2.0	5.0	1500	370	348	[98]
$CoSe_2$	51	1.2	0.2	100	1200	831	[101]
			1.0	400	786	503	
Co_3Se_4	43	3.1	0.2	800	1150	531	[105]
CoSe	58	–	1.0	300	912	716	[112]
			2.0	1200	797	414	
$MoSe_2$	58	1.2–1.5	0.2	120	1144	740	[115]
			1.0	300	851	585	
WSe_2	59	1.0	1.0	500	923	750	[116]
Mo_2C	64	2.1–2.5	1.0	1200	895	691	[119]
Fe_3C	70	2.0	0.2	100	1087	941	[121]
			1.0	250	1040	804	
Ti_3C_2	60	–	0.2	100	1206	104	[123]
			1.0	500	1028	803	
Co_4N	60	1.5	0.1	100	1246	1102	[126]
			5.0	400	786	658	
VN	64	1.3–1.5	0.2	100	1200	1008	[129]
TiO_2—TiN	51	1.0–3.0	2.0	500	766	640	[131]
MoS_2—MoN	–	1.2	0.2	100	≈1600	1100	[136]
			2.0	1000	778	459	
C_2N@$NbSe_2$	56	1.0	1.0	500	905	752	[137]
$CoSe_2/Co_3O_4$	61	2.0	0.2	200	1084	881	[140]
			2.0	500	780	602	
$CoNiO_2/Co_4N$	53	1.0	0.5	100	993	896	[141]
			4.0	600	688	389	
Ti_nO_{2n-1}	56	2.2	0.1	100	976	878	[152]
			2.0	1000	751	660	
RuO_{2-x}	67	2.0	0.2	100	1279	978	[156]
			1.0	600	1158	602	
$LaNiO_{3-x}$	–	4.4	0.2	100	1007	962	[158]
			0.5	500	714	707	
Se vacancy—$MoSe_2$	65	–	0.5	100	1196	≈1000	[163]
			2.0	400	981	785	
$WSe_{1.51}$	58	1.5	0.2	200	≈1100	886	[164]
			1.0	1000	926	741	
Tubular CoFeP@	60	1.0	1.0	200	844	814	[170]
CN		1.0	4.1	400	694	608	
rGO—PANI/MoS_2	70	1.0	0.5	200	1233	827	[90]
			5.0	700	947	524	
$CoSn(OH)_6$	49	1.0	1.0	600	≈700	≈415	[169]
nanocages		3.2	0.1	100	1156	775	

[a)]Sulfur content in cathodes.

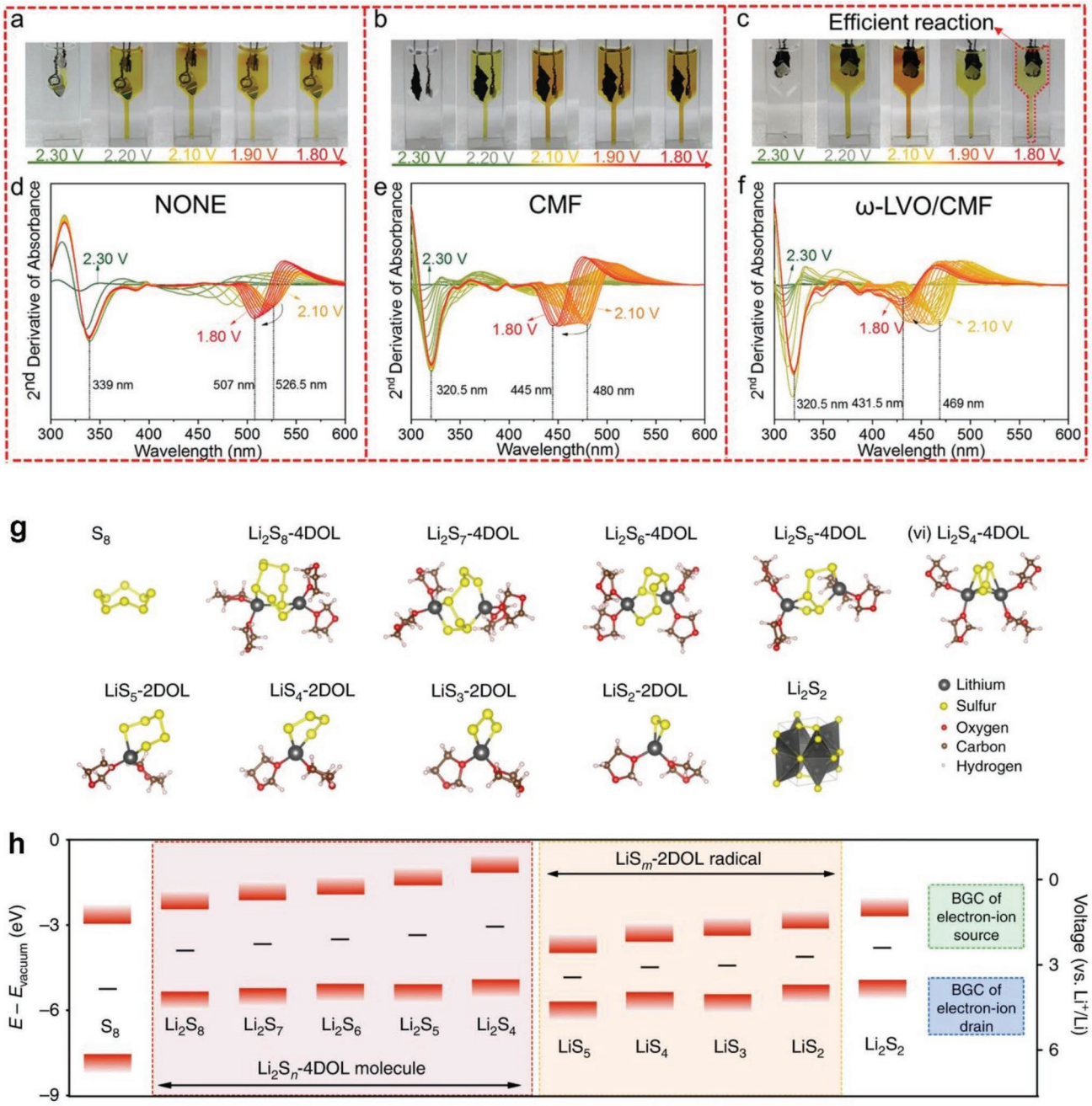

Figure 6. a–c) Synchronous UV–vis to investigate the conversion and diffusion of sulfur species in cuvettes, d–f) the 2nd derivative of the obtained UV–vis results. Reproduced with permission.[82] Copyright 2022, Wiley-VCH. g) Geometric structure of various sulfur species. h) Electronic band edges (the highest occupied and the lowest unoccupied levels, red bars) and bandgap centers (black lines) of solvated sulfur species aligned with respect to vacuum energy. Reproduced under the terms of the CC-BY license.[83] Copyright 2020, The Authors, Published by Springer Nature.

demonstrated by the change in activation energies (E_a) for the phase transition processes. Sulfur cathodes with In-based catalyst presented increased E_a for the reduction of S_8 to polysulfides compared to that with the In-free counterpart, meaning the sluggish formation of polysulfides. However, a decreased E_a for the following Li_2S deposition was observed from In-based catalyst, indicating the accelerated conversion kinetics. As a result, sulfur cathodes with In-based catalyst stabilized over 1000 cycles at 4.0 C and delivered an initial areal capacity up to 9.4 mAh cm^{-2} with a sulfur loading of about 9.0 mg cm^{-2}.

Moreover, combining different sulfur hosts with specific catalytic effects is another promising attempt. Li et al. designed hierarchical and defect-rich Co_3O_4/TiO_2 p–n heterojunctions (p-Co_3O_4/n-TiO_2-heterojunctions) to regulate the sequential conversion of S_8 to Li_2S_4, and to Li_2S.[85] Co_3O_4 sheets with abundant sites effectively adsorbed the pristine sulfur and facilitated

the rapid reduction of sulfur to Li_2S_4. Benefiting from the interfacial built-in electric field from the Co_3O_4/TiO_2 p–n junctions, the generated polysulfides resulted in the directional migration to TiO_2 dots, which accelerated the Li_2S precipitation. Therefore, the consecutive solid–liquid–solid conversion was improved. Consequently, sulfur cathodes with such p–n junctions delivered an initial capacity of 610 mAh g^{-1} at 10 C and maintained a favorable capacity decay of 0.07% per cycle over 500 cycles.

Mixed metal oxides have been applied in Li–S batteries to obtain enhanced reaction kinetics. Their catalytic activities for SRR depend on the substitution metals. For example, He et al. designed a nanoscale $CuFe_2O_4$ uniformly decorated on N-doped carbon nanofibers (CF/NC) as highly efficient catalysts for polysulfide conversion.[78] The mixed metal $CuFe_2O_4$ possessed better electronic conductivity than the single-metal counterparts due to the synergistic interface effect between the metal ions. The reaction activation energies for SRR have been dramatically reduced by CF/NC. CF/NC-based cells with sulfur loading of 5.75 mg delivered a capacity of 609 mAh g^{-1} after 300 cycles at 0.2 C. Sun et al. employed a dual transitional metal oxide ($NiMoO_4$) to facilitate the reduction of polysulfides.[86] Due to the intercalated Mo atoms, $NiMoO_4$ showed stronger metallic properties than NiO. The $NiMoO_4$ nanosheets lengthened the S—S bond distance of Li_2S_4 and reduced the free energy of polysulfide conversion, which was more beneficial to the thermodynamical sulfur reduction. In addition, $ZnCo_2O_4$ and $MnCo_2O_{4.5}$ have also been reported as electrocatalysts for SRR.[87,88]

Recently, our group developed a novel carbon-free $ZnFe_2O_4$ hollow rod as effective sulfur host to improve the performance of Li–S batteries.[77] $ZnFe_2O_4$ hollow structures were formed by urea-assisted etching of the MIL-88A rod precursors, followed by a calcination process (**Figure 7**a). Due to the abundant active sites, hollow $ZnFe_2O_4$ rods effectively anchored sulfur species and rapidly converted them to discharging products. The favorable catalytic effects improved the liquid–liquid and the liquid–solid conversion for SRR. Compared with sulfur cathodes with carbon black as host (S/C), the composite sulfur cathodes ($S@ZnFe_2O_4$) exhibited lower overpotential both in the high-voltage and low-voltage discharging plateaus. Besides, $ZnFe_2O_4$ rods also enabled a high Li_2S deposition capacity. The accelerated SRR kinetics by $ZnFe_2O_4$ has been validated by activation energy studies. As shown in Figure 7b–g, electrochemical impedance spectroscopy (EIS) tests were performed at various temperatures and at different states-of-charge (SoCs) to determine the temperature dependence of charge transfer resistance (R_{ct}). The calculated activation energies in SRR increased gradually for both S/C and $S@ZnFe_2O_4$, revealing that the reaction kinetics became more difficult due to the increased energy barriers. However, the activation energies for $S@ZnFe_2O_4$ showed significantly smaller values than S/C at all SoCs, indicating that $ZnFe_2O_4$ has effectively activated the sulfur reduction reaction, improving the charge transfer kinetics of sulfur cathodes under all conditions. The introduced $ZnFe_2O_4$ rods significantly enhanced the utilization of sulfur cathodes with better cycle life.

3.2.2. Sulfides

Owing to the excellent catalytic activity for water splitting,[89] sulfides have also been explored to catalyze the reduction process of sulfur cathodes. Various metal sulfides, such as MoS_2,[90] MoS_3,[91] SnS_2,[92] VS_4,[93] ReS_2,[94] CdS,[95] and FeS,[96] have been demonstrated as efficient catalysts for SRR.

Babu et al. performed a comprehensive investigation into the preferential active sites of XS_2 (X = Mo, W) for polysulfide electrocatalysis.[97] The authors demonstrated that the preferential adsorption of polysulfides and subsequent reduction to solid sulfur species were in the form of dendrite-like structures at the edge sites of XS_2 due to the unsaturated sulfur atoms. This was supported by Lin et al., who showed that MoS_{2-x}/reduced graphene oxide (MoS_{2-x}/rGO) catalyzed the reduction of polysulfides with improved battery performance.[21] Microstructural characterization confirmed that sulfur deficiencies at the surface significantly enhanced the polysulfide conversion kinetics. MoS_2 with metastable octahedral (1T) and distorted octahedral (1T′) phases exhibits (semi) metallic properties for promising applications in catalysis, but the intrinsic aggregation of 2D layered MoS_2 hampers the exposure of active sites. The design of 3D composite structures combined with porous carbon would be an alternative to improve catalytic activities. He et al. designed a novel free-standing 3D graphene/1T MoS_2 (3DG/TM) heterostructure to improve the reduction kinetics of sulfur cathodes.[98] The few-layered graphene nanosheets were sandwiched by hydrophilic, metallic, few-layered 1T MoS_2 nanosheets with abundant active sites. Along with the rich porosity of 3DG/TM, charge transfer and electrolyte penetration were greatly accelerated. The resulting cells with 3DG/TM delivered a high reversible capacity of 1181 mAh g^{-1} with the retention of 96.3% after 200 cycles. The catalytic activities for SRR can be further improved by introducing heteroatom doping to carbon, by which MoS_2 and doped carbon can both provide excellent chemical adsorption and efficient catalytic conversion of sulfur species.[99] This was validated by Yu et al., who reported 1T-MoS_2 nanotubes wrapped with N-doped graphene as highly efficient absorbent and electrocatalyst for Li–S batteries.[100] The cathode can maintain a superior reversible capacity of 1219 mAh g^{-1} after 200 cycles at 0.2 C.

Another promising approach is to tailor the heteroatom doping of MoS_2 to enhance the catalytic activities. By regulating Co and P heteroatom codoping of MoS_2 nanotubes, Lin et al. first explored the enhanced effects of doped MoS_2 catalysts on sulfur conversion kinetics.[101] It was confirmed that the Co-doping caused the conversion of MoS_2 from 2H to metallic 1T phase, improving the electrical conductivity of catalysts. Meanwhile, P-doping led to the formation of Co—P coordinated sites at the surface of catalysts, efficiently catalyzing the conversion of polysulfides. Consequently, sulfur cathodes with optimized Co, P-codoped MoS_2 catalysts achieved a low-capacity fade rate of 0.046% per cycle for 600 cycles at 1.0 C.

Considering the inert catalytic activities of the coordinatively saturated sites at the MoS_2 basal planes, Tian et al. developed B-doped MoS_2 nanosheets on CNT (CNT@MoS_2—B) to modulate the feasible orbital orientation of the basal plane.[102] Theoretical calculations revealed that B in MoS_2—B was sp^3 hybridized with a vacant σ orbital perpendicular to the basal plane, which can act as an active electron acceptor. The electron localization function (ELF) analysis in **Figure 8**a shows the covalent link between MoS_2—B

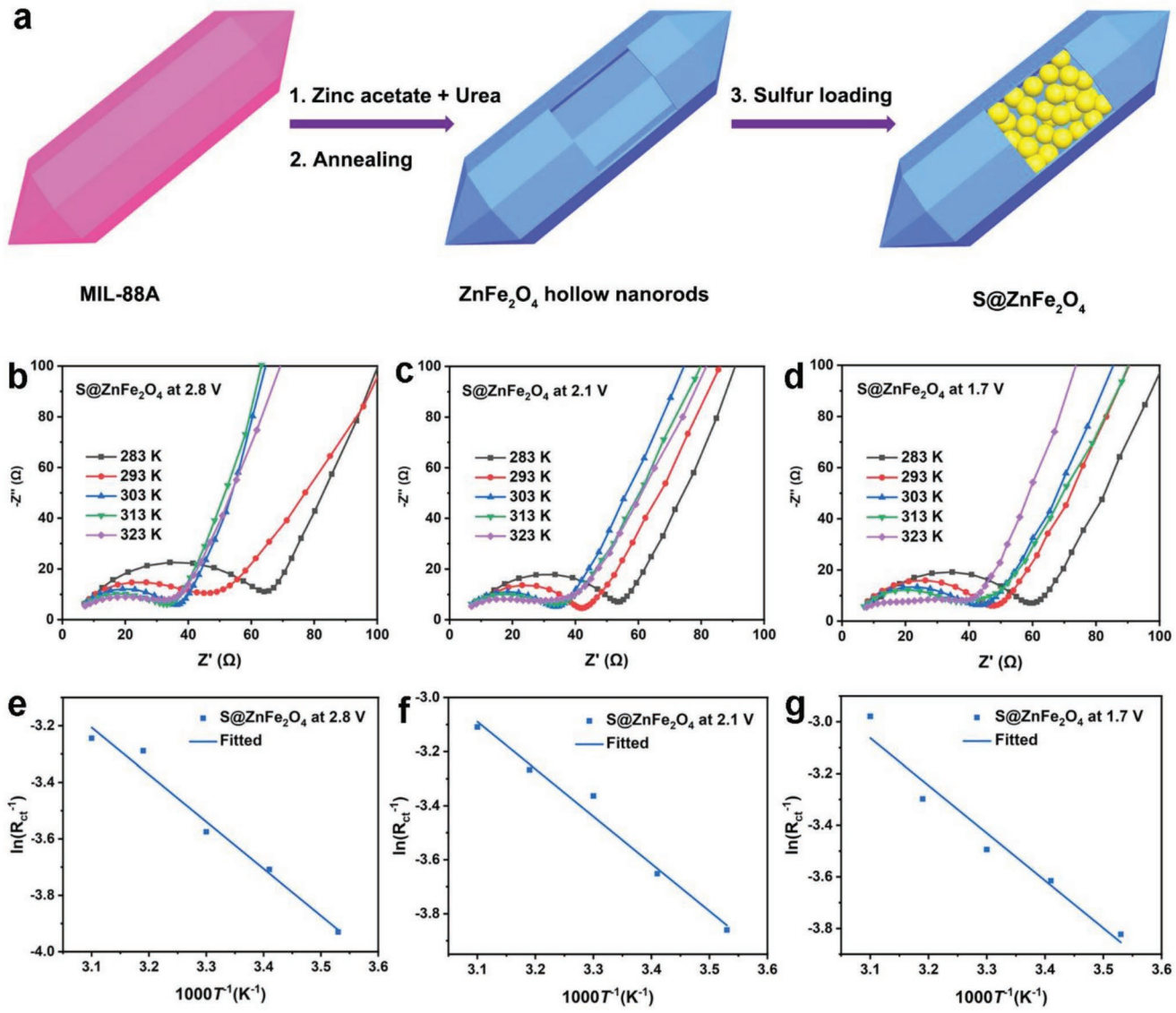

Figure 7. a) Schematic representation of the fabrication process of $S@ZnFe_2O_4$ composite materials. Nyquist plots of $S@ZnFe_2O_4$ cathodes at b) 2.8, c) 2.1, and d) 1.7 V at various temperatures. Arrhenius plots for $S@ZnFe_2O_4$ cathodes showing the relation between the charge transfer resistance and temperature at e) 2.8, f) 2.1, and g) 1.7 V, respectively. Reproduced under the terms of the CC-BY license.[77] Copyright 2022, The Authors, Published by Elsevier.

and S_8 to form the B—S bond. The same bonding was also traced between MoS_2—B and Li_2S_4 in Figure 8b. That can be explained by the Lewis acid–base interaction in Figure 8c. The lowest unoccupied molecular orbital of B can accept an electron pair from the highest occupied molecular orbital of S, forming a coordinate covalent bond. The density of state (DOS) projected onto p_z orbitals of the two adsorption systems indicated the intensive *z*-directional orbital coupling validated by the significant electronic state overlap between B and S (Figure 8d). This was due to the perpendicularly vacant σ orbital of B, allowing the maximized head-on orbital overlap with occupied orbital of S, efficiently activating the basal plane of MoS_2 (Figure 8e). The suitable orbital orientation of the basal plane significantly increased the binding energies of MoS_2—B toward sulfur species (Figure 8f) compared with pristine MoS_2. Meanwhile, the whole discharging process of sulfur at MoS_2—B showed more negative Gibbs free energy change than that at MoS_2, implying that MoS_2—B enabled a more thermodynamically favorable reduction of sulfur (Figure 8g). Therefore, the incorporation of B significantly increased the reactivity of the MoS_2 basal plane and facilitated the sulfur reduction kinetics.

In addition to MoS_2, many other sulfides with various morphologies have been developed. Xu et al. designed ZnS nanospheres as SRR catalysts, which simultaneously promoted the conversion of the liquid–liquid and liquid–solid reactions during discharging.[103] Shen et al. reduced the size of ZnS to quantum dots and grew them on graphene nanosheets. The active sites were significantly enlarged.[104] They demonstrated

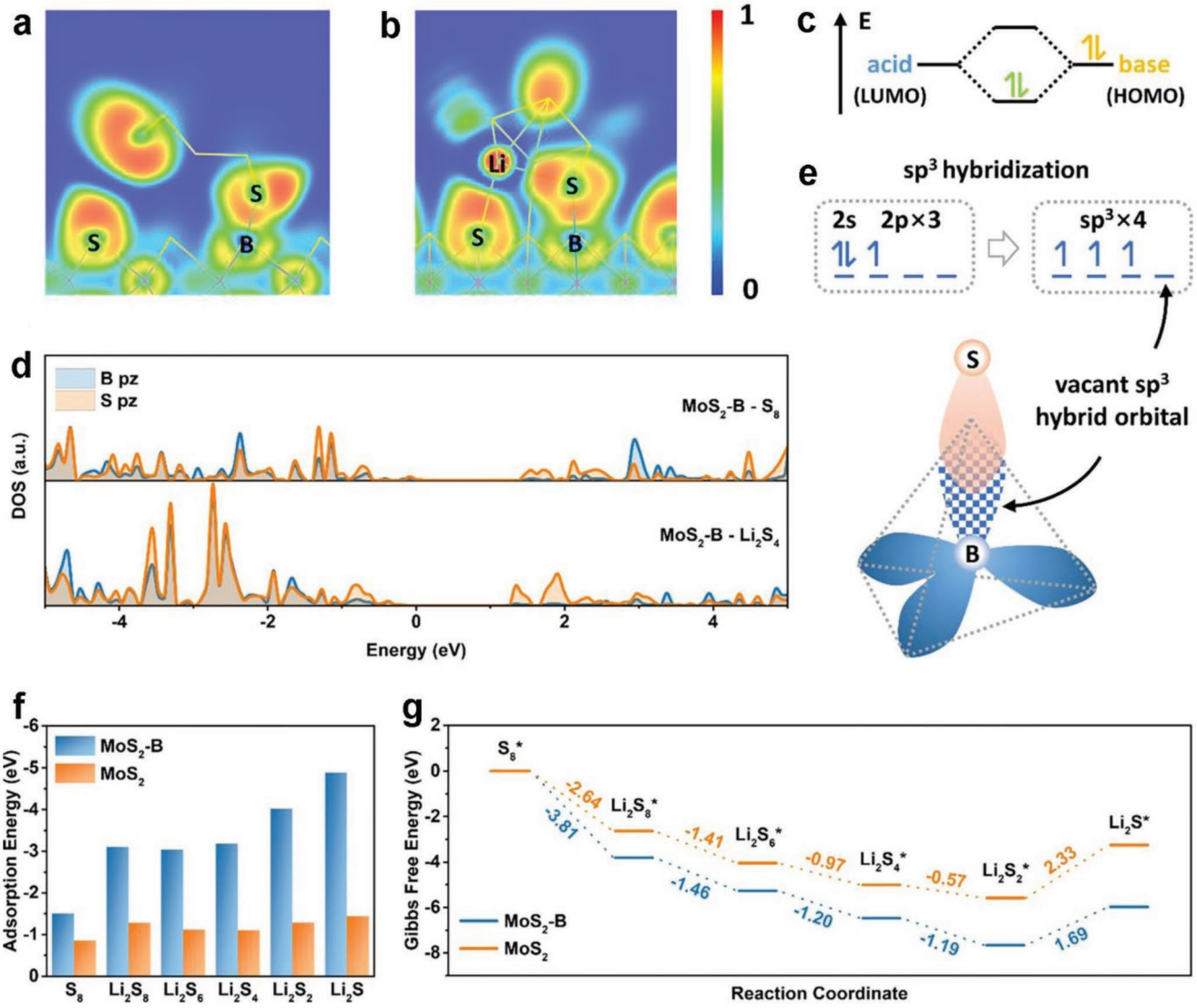

Figure 8. ELF plots of a) the MoS_2—B—S_8 and b) the MoS_2—B—Li_2S_4 adsorption systems. c) Schematic representation of the Lewis acid–base interaction. d) DOS projected onto p_z orbitals for the MoS_2—B—S_8 and MoS_2—B—Li_2S_4 adsorption system. e) Schematic for the sp^3 hybridization of B in MoS_2—B and the head-on orbital overlap between B and S. f) Adsorption energies of sulfur species and g) Gibbs free energy changes of sulfur reduction processes on MoS_2—B and MoS_2. Reproduced with permission.[102] Copyright 2021, American Chemical Society.

that the interfacial electronic interactions between conductive carriers and ZnS quantum dots enhanced the charge transfer, strengthened the binding to polysulfides, and accelerated the redox kinetics of sulfur. The introduction of conductive carbon carriers can also enhance the catalytic activities of cobalt sulfides for sulfur conversion, because they possess the large specific surface area and high conductivity. The large specific surface is beneficial to the uniform dispersion of catalysts. The high conductivity improves charge transfer for catalytic reactions. Co-based MOF is an excellent precursor to obtaining Co_3S_4- or Co_4S_3-embedded carbon nanostructures by a facile calcination process.[105,106] Moreover, integrating carbon substrates with vanadium sulfides will display synergistic effects on the SRR kinetics. Zhang et al. reported thin V_5S_8 nanoflakes with size of 30–50 nm decorated at the surface of carbon nanofibers.[107] The unit cell of V_5S_8 was distorted due to the occupation of V atoms in the interlayer spacing of VS_2 monolayers, which achieved enhanced catalytic activities on the redox reaction of polysulfides. Zhao et al. fabricated a functional layer consisting of VS_4 and tannin acid to synergistically catalyze the sulfur conversion.[108]

It is believed that metal compounds, instead of carbon carriers, are responsible for catalyzing SRR.[98] Metal ions can interact with sulfur species by anchoring them at the surface of catalysts and decreasing the reaction barriers, thus resulting in accelerated conversion kinetics. Spectroscopic characterization and theoretical calculations also support the claim.[103] In principle, catalysts can display favorable catalytic activities without a carbon support, since they possess intrinsic catalytic sites. However, synergistically enhanced effects can be obtained when combining conductive carbon carriers.

3.2.3. Selenides

Generally, selenides exhibit higher conductivities than sulfides, allowing them to be promising candidates applied in Li–S batteries. Besides, given the good catalytic activities of Co atoms, cobalt selenides are investigated in detail to enhance the SRR kinetics. Yuan et al. proposed a triple-phase interface model containing the electrolyte, $CoSe_2$ catalyst, and a reduced graphene oxide substrate to synergistically regulate the SRR kinetics.[109] The $CoSe_2$ nanodots with abundant exposure of active sites intimately adsorbed soluble polysulfides and enabled the uniform nucleation and growth of Li_2S. Meanwhile, the metallic $CoSe_2$ also benefited the fast electron transport. These merits for triple-phase interfaces allowed sulfur cathodes an initial capacity of 916 mAh g^{-1} at 6.0 C. Furthermore, He et al. found that the stable (111) surface of $CoSe_2$ possessed both nucleophilic and electrophilic centers based on first-principle calculations.[110] The bipolar (111) surface was beneficial to the adsorption and conversion of polysulfides. $CoSe_2$ nanocrystals with a specific (111) surface embedded in porous carbon nanocages were fabricated according to theoretical predictions. The bipolar (111) surface of $CoSe_2$ effectively promoted the conversion kinetics of polysulfides by decreasing the reaction energy barriers.

Properties of the synthesized cobalt selenides vary due to differences in reaction templates and selenylation processes. Selenylation at 650 °C of immersed N-doped carbon networks at the $Co(NO_3)_2$ solution resulted in highly conductive Co_3Se_4 nanoparticles.[111] The obtained composite sulfur cathodes delivered a high initial capacity of 1150.3 mAh g^{-1} at 0.2 C with a reversible capacity of 531.0 mAh g^{-1} after 800 cycles. Ye et al. used zeolitic imidazolate framework-67 (ZIF-67) as precursor to fabricate CoSe embedded in hierarchically porous polyhedron (CS@HPP).[112] The CS@HPP with high crystal quality and abundant active sites boosted the anchoring of polysulfides and catalyzed the rapid Li_2S deposition. A high areal capacity of 8.1 mAh cm^{-2} was achieved by the freestanding CC@CS@HPP cathode with 8.1 mg cm^{-2} sulfur loading. Besides, introducing another metal to cobalt selenides can also modulate the catalytic activities. Combining the metallic nature and the synergetic effects of Ni and Co atoms, Zhang et al. designed urchin-shaped $NiCo_2Se_4$ (u-NCSe) nanostructures to accelerate the conversion kinetics of sulfur species.[113] The resulting S@u-NCSe cathodes reached a low-capacity decay rate of 0.016% per cycle over 2000 cycles at 3.0 C.

Like cobalt selenides, $MoSe_2$ has also been proposed to catalyze the reduction of sulfur. Tian et al. synthesized a hybrid composed of sulfiphilic few-layered $MoSe_2$ nanoflakes decorated with reduced graphene oxide ($MoSe_2$@rGO) by a facile hydrothermal method.[114] Sulfiphilic $MoSe_2$ effectively alleviated the electrode polarization and benefited the fast nucleation and uniform deposition of Li_2S. $MoSe_2$@rGO enabled the sulfur cathode to deliver a high initial capacity of 1608 mAh g^{-1} at 0.1 C. Another 1D $MoSe_2$@C nanorod with core–shell structures was developed by Li et al. via a facile hydrothermal and subsequent selenylation reaction.[115] As an electrocatalyst, $MoSe_2$@C nanorods greatly improved the redox kinetics of sulfur species, thus boosting the performance of Li–S batteries. Compared with graphene, the $MoSe_2$ catalyst significantly decreased the activation energies of the SRR. This fact resulted from the effective adsorption of sulfur species at the $MoSe_2$ surface via the Se—Li bond, which weakened the S—S bond and accelerated the breakage. The enhanced SRR kinetics by $MoSe_2$ was supported by the DFT calculations. As illustrated in **Figure 9**a, the Gibbs free energies of the reaction pathway for SRR at the surface of $MoSe_2$ and graphene were compared. For the reduction of S_8 to Li_2S_8 and to Li_2S_6, both $MoSe_2$ and graphene showed a negative Gibbs free energy change, indicating an exothermic and spontaneous reaction. The more negative energy change at $MoSe_2$ than on graphene revealed a more advantageous reduction kinetics. The following reduction to solid Li_2S on $MoSe_2$ and graphene displayed, however, an endothermic and unspontaneous process due to the positive free energy change. $MoSe_2$ significantly reduced the Gibbs free energy barriers compared with graphene. The above results suggested that the whole SRR kinetics has been accelerated by $MoSe_2$ due to the excellent catalytic activity.

The application of WSe_2 in Li–S batteries was reported by Zhang et al. They developed a simple solution-based method to prepare N-doped graphene/WSe_2 (NG/WSe_2) superlattices.[116] As shown in Figure 9b, the first step involved a solvothermal reaction of ammonium metatungstate (AMT) and selenium powder in the presence of polyvinylpyrrolidone. The obtained products were then annealed at 800 °C in inert atmosphere, converting them to NG/WSe_2 superlattices. The continuously adjustable interlayer space in the range from 10.4 to 21 Å allowed NG/WSe_2 superlattices a metallic character with outstanding electrical conductivity. The resulting S@NG/WSe_2 cathodes exhibited a superior rate performance at 5.0 C with a capacity of 569.5 mAh g^{-1}.

3.2.4. Carbides and Nitrides

Due to the metallic characteristics and strong polarity, carbides and nitrides have been employed to catalyze the electrochemical reaction of Li–S batteries. Razaq et al. found that Mo_2C nanoparticles anchored on CNT showed strong adsorption and activation toward polysulfides.[117] The accelerated redox kinetics of polysulfides effectively mitigated the shuttle effect. By dispersing ultrafine Mo_2C nanoparticles on 3D hollow N-doped carbon flowers, Razaq et al. further accelerated the electrocatalytic conversion of polysulfides.[118] The uniformly distributed Mo_2C nanoparticles provided abundant catalytic active sites for efficient sulfur adsorption and conversion. Yu et al. in situ fabricated Mo_2C-quantum-dot (QD)-decorated CNT networks (MCNs) as absorbent and electrocatalyst for Li–S batteries.[119] In situ Raman spectroscopy confirmed only weak Li_2S_8, Li_2S_6, and Li_2S_4 signals detected at the side of the separator near the lithium anodes during the entire discharging process of MCN/S cathodes. The in situ analyses indicated that MCN enabled the rapid catalytic conversion of sulfur species to alleviate the shuttle effect. Besides, MoC nanocrystals were embedded in N-doped carbon microspheres as sulfur hosts by Li et al.[120] The distributed MoC nanocrystals enhanced the adsorption toward polysulfides by forming the Mo—S bonds and catalyzed the rapid formation of Li_2S clusters to accelerate the sulfur conversion kinetics. The composite sulfur cathodes attained a reversible capacity of 1370 mAh g^{-1} at 0.1 C.

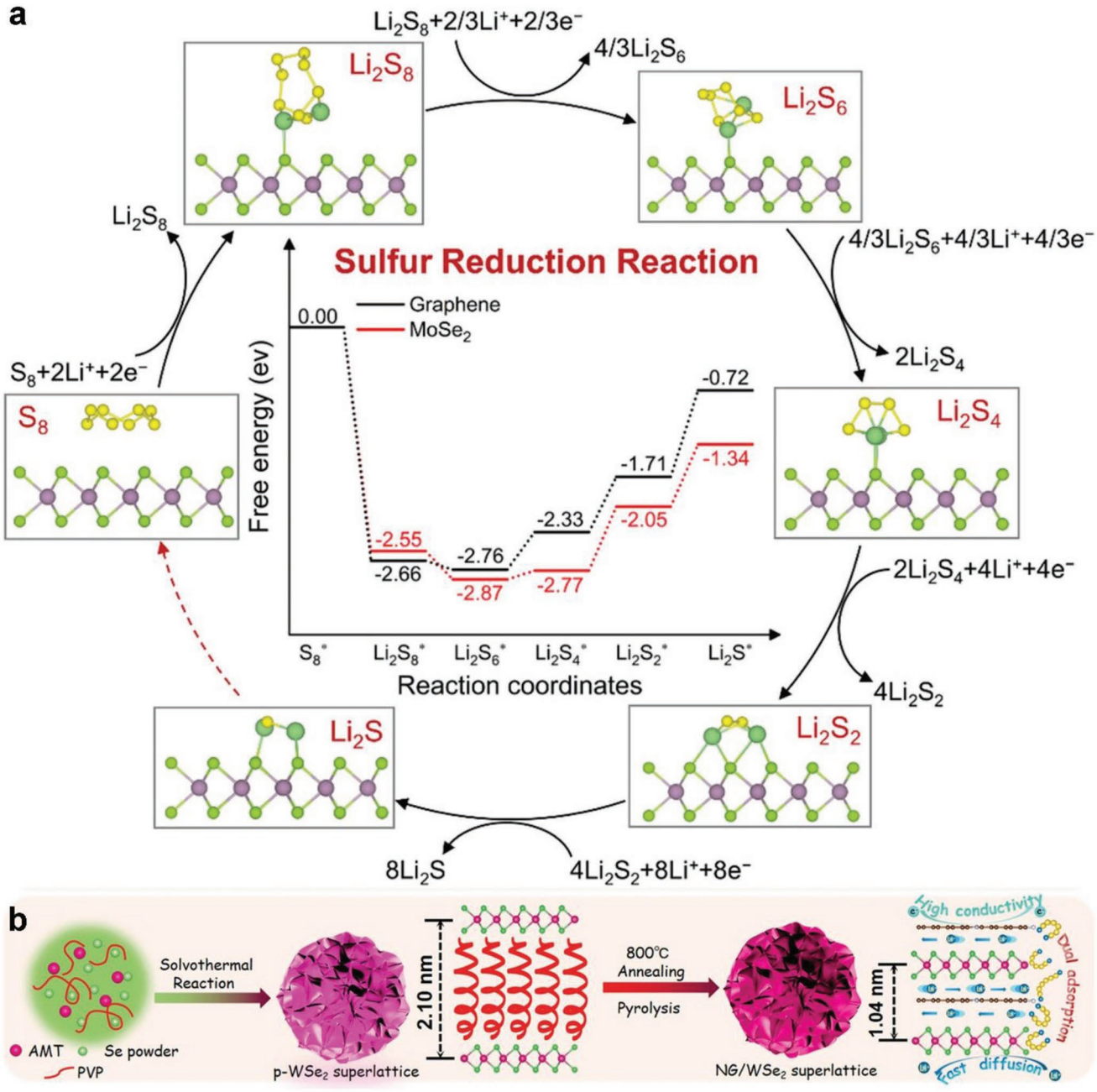

Figure 9. a) DFT calculated free energy diagram for SRR of graphene and $MoSe_2$. Insets show the corresponding optimized structural configurations. Reproduced with permission.[115] Copyright 2022, Wiley-VCH. b) Schematic illustration of the synthetic process used to produce a NG/WSe_2 superlattice. Reproduced with permission.[116] Copyright 2022, Wiley-VCH.

Other carbides like Fe_3C and Ti_3C_2 have also revealed an enhanced conversion kinetics for Li–S batteries. For example, Wu et al. developed a 3D network-like Fe_3C–carbon nanofiber interlayer, in which the uniformly distributed Fe_3C nanoparticles effectively reduced the interfacial resistance and enhanced the redox kinetics of sulfur species.[121] Hong et al. combined the sulfophilic sites of Ni and lithophilic sites of Zn to prepare bimetal carbide $Ni_3ZnC_{0.7}$ for high-rate Li–S batteries.[122] The authors found that $Ni_3ZnC_{0.7}$ could efficiently anchor polysulfides and facilitate their transformation to Li_2S. The synergistic effect of Ni and Zn allowed a high initial capacity of 1275 mAh g^{-1} at 1.0 C.

Recently, Wang et al. fabricated hierarchically porous Ti_3C_2 MXene microspheres as multifunctional electrocatalyst.[123] They first predicted that the edge sites of Ti_3C_2 showed more significant adsorption and catalytic activity for sulfur species by DFT calculations. Then enriched edge-site Ti_3C_2 (e-Ti_3C_2) was synthesized by a combined spray drying and chemical etching method. As illustrated in **Figure 10**a, the spray drying process resulted in Ti_3C_2/polymethyl methacrylate (PMMA)

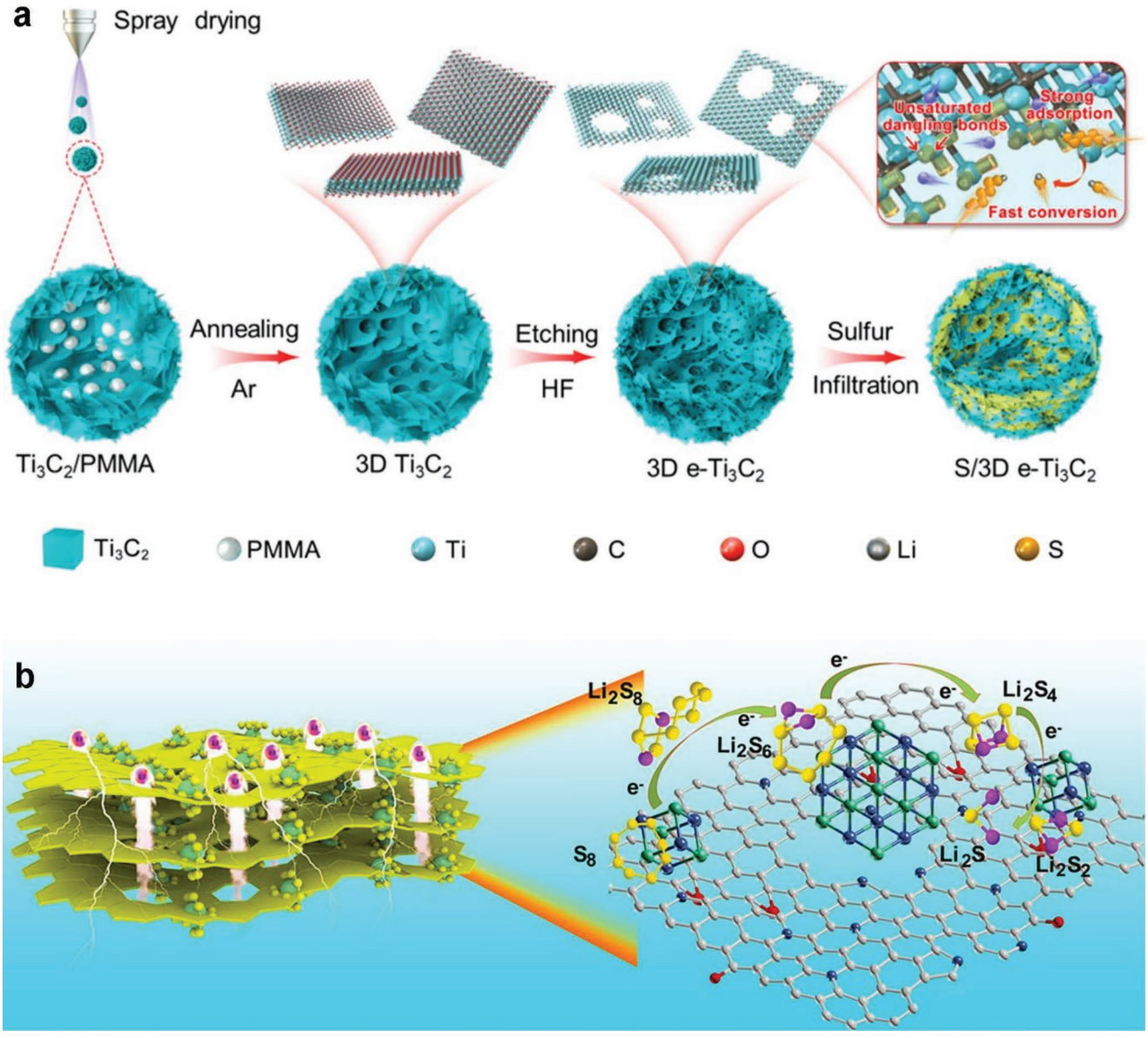

Figure 10. a) Schematic illustration of the fabrication of S/3D e-Ti_3C_2 microspheres. Reproduced with permission.[123] Copyright 2021, American Chemical Society. b) VNQD—HG simultaneously promoting trapping, anchoring, and catalyzing sulfur species. Reproduced with permission.[129] Copyright 2021, American Chemical Society.

microspheres with oxygen terminated sites. An annealing treatment removed PMMA, leading to the formation of 3D macroporous microspheres (3D Ti_3C_2). Selective etching of O—Ti bonds exposed abundant active edge sites with coordinatively unsaturated Ti and generated abundant pores within the framework. The hanging bonds at the surface of Ti atoms with the unsaturated coordination bonds formed strong adsorption sites for polysulfides, accelerating the catalytic conversion of sulfur species. The coordination bonding configuration and electronic state effect of Ti were further demonstrated by X-ray absorption near edge structure spectroscopy (XANES) and extended X-ray absorption fine structure (EXAFS). These structural advantages allowed composite sulfur cathodes a high discharge capacity of 1206 mAh g^{-1} at 0.2 C.

Polar TiN with high conductivity can adsorb polysulfides and promote redox conversion. For example, Hao et al. constructed a S-doped oxidation layer at the surface of TiN nanoparticles to enhance the catalytic activities of nitrides for the sulfur electrochemical conversion reaction.[124] The introduction of sulfur formed an integrated heterointerface composed of Ti—S, Ti—O, and Ti—N bonding, greatly enhancing the polysulfide conversion kinetics. By incorporating Fe, Zhao et al. converted hexagonal Ni_3N nanoparticles into a highly active cubic Ni_3FeN phase, promoting the SRR kinetics.[125] Ni_3FeN enabled sulfur cathodes with 4.8 mg cm^{-2} sulfur loading a high capacity of 822 mAh g^{-1} at 3.0 C.

The increased conversion kinetics of sulfur cathodes can also be achieved by Co_4N. Sun et al. designed Co_4N nanoparticles

embedded in N-doped carbon, giving rise to a decreased polarization for the sulfur conversion reaction.[126] A reversible capacity of 658 mAh g^{-1} after 400 cycles with a low capacity-fading rate of 0.04% per cycle was obtained at 5.0 C. Zhang et al. proposed another sulfur host based on Co_4N nanoparticles decorated on vertically aligned wood-derived carbon plates.[127] The Co_4N nanoparticles decreased the energy barriers for sulfur conversion, which was validated by DFT calculations and experimental observations. In addition, integrating vanadium nitrides (VN) with conductive carbon as catalysts for SRR has been reported. Yang et al. developed a one-pot strategy for the synthesis of N-doped porous graphitic carbon with bound VN nanocrystals (3D VN@N−PGC).[128] The electrocatalytic centers of N−Li^+ and V−S^{2-} species confirmed by XANES gave rise to synergistic electrocatalytic effects on the sulfur conversion kinetics. Sulfur cathodes based on 3D VN@N−PGC host materials delivered a high capacity of 1442 mAh g^{-1} at 0.1 C. Li et al. innovatively synthesized a VN quantum dots/holey graphene matrix (VNQD−HG) as alternative sulfur host.[129] The abundant edge catalytic sites of VNQD and in-plane nanopores of graphene enabled strong anchoring toward polysulfides and solid Li_2S, and fast conversion kinetics of SRR (Figure 10b). The resulting sulfur cathode delivered an initial capacity of 1320 mAh g^{-1} at 0.1 C.

3.2.5. Heterostructures

Heterostructures can integrate the merits of different components to achieve synergetic effects on electrocatalytic SRR due to the intrinsic drawbacks of a single component. For example, oxides show a strong adsorption of sulfur species but unfortunately have a low conductivity. By contrast, carbides and nitrides are highly conductive but less adsorptive. Therefore, heterostructures combining these advantages have been widely studied to enhance the SRR kinetics. Early research on TiO_2−TiN heterostructures has validated the synergetic effects, enabling strong adsorption of polysulfides by TiO_2 and subsequently accelerating conversion into Li_2S by TiN.[130] Xue et al. further enhanced the function of TiO_2−TiN heterostructures in both promoting the electrocatalysis of SRR and inhibiting the dendrite growth at lithium anodes.[131] Other titanium-oxide-based heterostructures, such as TiO_2−MXene,[132] TiO_2−CoS,[133] and Ti_4O_7−TiN,[134] have revealed good kinetic enhancement in the conversion of sulfur cathodes. Moreover, nitride-based heterostructures also displayed synergically enhanced effects on adsorbing sulfur species and boosting the conversion. Yao et al. designed TiN−VN in situ embedded on freestanding carbon nanofibers (TiN−VN@CNFs) as sulfur host. The structural advantages of this heterostructure allowed Li–S batteries to enhance sulfur utilization with a high-rate performance at 5.0 C.[135]

Similarly, Wang et al. reported MoS_2−MoN heterostructure nanosheets grown on CNT arrays as freestanding sulfur cathodes.[136] MoN provided coupled electrons to accelerate the redox reaction of polysulfides. Meanwhile, MoS_2 facilitated fast Li^+ diffusion. The adsorption–diffusion-controlled catalytic conversion of polysulfides was enhanced by the synergetic function of MoS_2−MoN. An in situ grown C_2N@$NbSe_2$ heterostructured catalyst was designed by Yang et al. via a facile and effective two-step strategy.[137] Theoretical calculations and experimental results validated that the suitable electronic structure and charge rearrangement of these heterostructures strongly accelerated the conversion kinetics of sulfur species. C_2N@$NbSe_2$/S cathodes showed an impressive cycling stability with only 0.012% capacity decay per cycle over 2000 cycles at 3.0 C. In addition, iron- and vanadium-nitride-based heterostructures like Fe_3C−Fe_3N and V_2O_3−VN have revealed effective adsorption and electrocatalytic activities for sulfur species.[138,139]

The excellent catalytic activity of active Co sites allows Co-based heterostructures to be widely applied in Li–S batteries. Co_3O_4 exhibits a good adsorption capacity for sulfur species, but the poor conductivity is detrimental to electron transport. Combining Co_3O_4 with another high electrical conductive component would benefit the electrochemical kinetics. $CoSe_2$/Co_3O_4 heterostructures encapsulated into a N-doped carbon layer and a CNT framework (NC−CNT) were therefore prepared by Chu et al.[140] The pyrolysis process formed abundant CNTs with high porosity and hollow nanostructures, generating a high surface area for catalytic conversion (**Figure 11**a,b). Highly crystalline fringes were found at the heterostructure interfaces (Figure 11c). The generated CNTs with a small diameter of 11 nm provided conductive channels for electron transport (Figure 11d). Two different domains of $CoSe_2$ and Co_3O_4 are shown in Figure 11e, indicating the successful formation of $CoSe_2$/Co_3O_4 heterostructures. This was further validated by the lattice fringe spacings of 0.259 and 0.243 nm in Figure 11f, associated with (111) and (311) facets of $CoSe_2$ and Co_3O_4, respectively. The uniform distribution of various elements in Figure 11g demonstrated the high quality of the heterostructure. The above structural advantages allowed the effective adsorption of polysulfides by Co_3O_4 and accelerated conversion by $CoSe_2$. Moreover, $CoSe_2$/Co_3O_4 heterostructures with sulfiphilic active sites regulated a uniform precipitation of Li_2S. Such a heterostructure gave the sulfur cathode a high initial capacity of 1457 mAh g^{-1} at 0.1 C.

Pu et al. fabricated homogeneous $CoNiO_2$/Co_4N nanowire heterostructures (Figure 11h), which greatly enhanced the reaction kinetics of polysulfides.[141] The uniform nanowires were 8–12 nm average in diameter (Figure 11i,j). Clear lattice fringes were revealed at the (200) planes of NiO and (111) planes of $CoNiO_2$ (Figure 11k) by high-resolution transmission electron microscopy (HRTEM), in agreement with the selected area electron diffraction (SAED) results (Figure 11l). The strong adsorptive and catalytic properties of $CoNiO_2$ and electrical conductivity of Co_4N contributed to synergistic enhancement effects on the SRR kinetics, leading to a high-rate capacity of 688 mAh g^{-1} at 4.0 C.

Due to the synergistically enhanced effects on controlling sulfur species deposition, heterostructures can effectively induce the Li_2S nucleation and facilitate the precipitation. For example, Cai et al. combined MoO_2 and α-MoC to construct a heterostructure MoO_2/α-MoC catalyst to improve the Li_2S deposition.[142] The minor difference in electronic conductivity between MoO_2 and α-MoC showed distinct trapping–diffusion–conversion effects on sulfur species. DFT calculation revealed the enhanced affinity to polysulfides and Li_2S by the MoO_2/α-MoC heterogeneous interfaces compared to the individual component. The heterogeneous interfaces enabled the

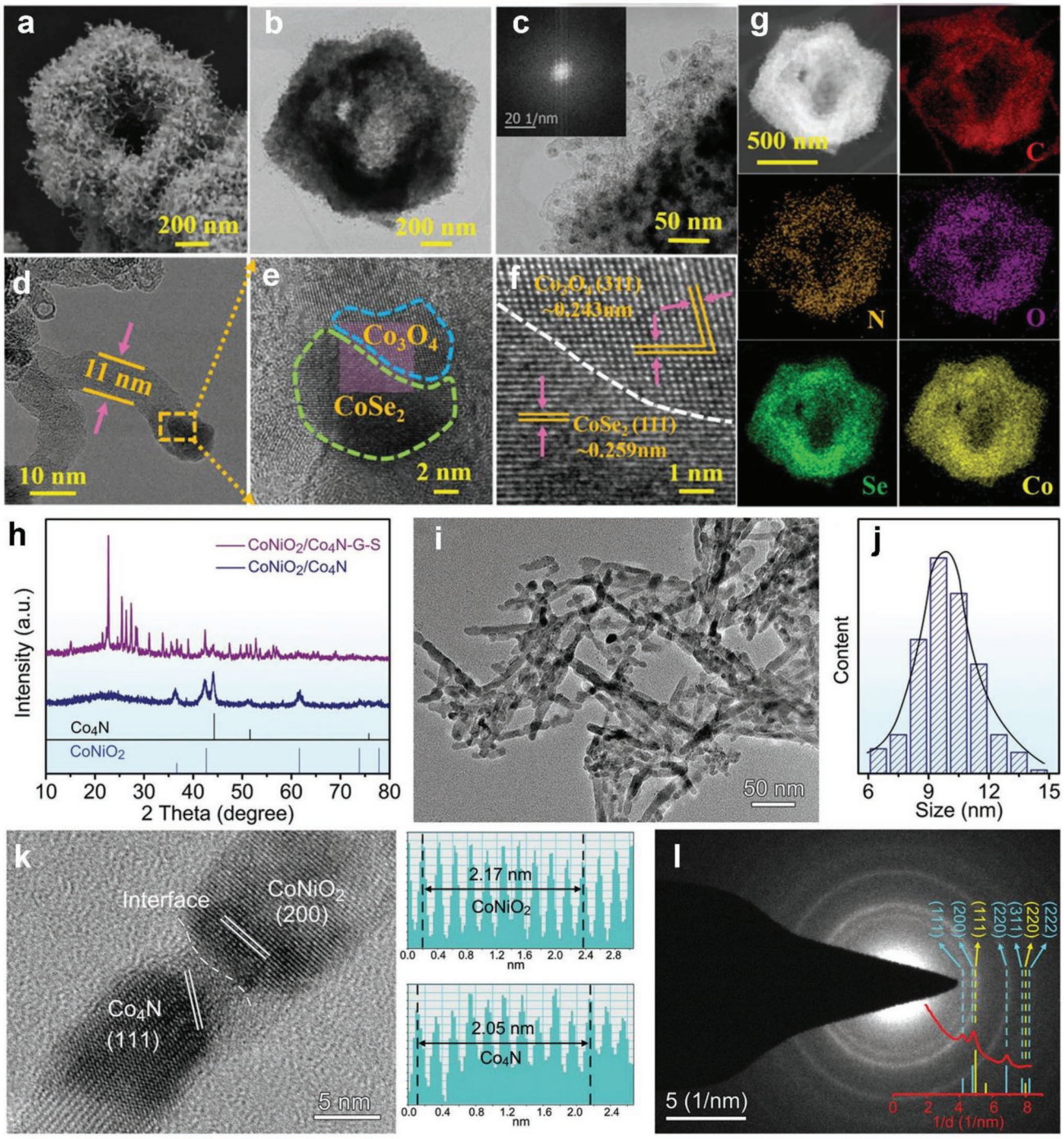

Figure 11. a) SEM image, b,c) TEM images, d–f) HRTEM image of the $CoSe_2/Co_3O_4$@NC—CNT heterostructure, g) scanning transmission electron microscopy (STEM) image and elemental mapping show the distribution of C, N, O, Se, Co, respectively. Reproduced with permission.[140] Copyright 2022, Wiley-VCH. h) XRD patterns. i,j) TEM image and diameter distribution. k) HRTEM result and the corresponding lattice spacing. l) SAED pattern and rotational integral. Reproduced with permission.[141] Copyright 2022, Wiley-VCH.

beneficial Li_2S nucleation sites and resulted in its 3D precipitation, improving the deposition capacity of Li_2S. As the electrocatalyst, heterostructure MoO_2/α-MoC allowed sulfur cathodes to achieve a high specific capacity of 1177 mAh g^{-1} at 0.2 C and 695 mAh g^{-1} at 3.0 C with a low-capacity fading. By modifying Mo_2N microbelt with SnO_2 nanodots, Yang et al. prepared a heterostructure catalyst (SND—Mo_2N) with rich heterointerfaces to regulate the Li_2S deposition.[143] The metallic Mo_2N microbelt displayed high electrical conductivity and good catalytic activity, which was beneficial to the reaction kinetics of polysulfides and the Li_2S deposition. Meanwhile, the SnO_2 nanodots showed moderate adsorption ability to trap

polysulfides. The rich interfaces with strong synergistic effects provided abundant nucleation sites to guide the Li_2S growth in a 3D model, significantly preventing the catalyst surface from passivation. As a result, sulfur cathodes with SND—Mo_2N additives delivered a high capacity of 738 mAh g^{-1} at 0.5 C after 550 cycles with an ultralow capacity decay of 0.025% per cycle.

Other heterostructures, including Nb_2O_5—NbC,[144] MoS_2—MoO_3,[145] $MoSe_2$—MXene,[146] ZnS—SnS,[147] and Mo_2C—MoO_3,[148] have also been reported. Heterostructures generally improve the electrochemical performance of Li–S batteries by combining a high adsorption and strong catalytic activity from the individual components. Therefore, choosing the proper component is the key to obtaining highly efficient heterostructures. Preparation is, however, another important factor, determining the interface/surface properties of the heterostructures.

3.2.6. Vacancies

Vacancy design is a practical approach to regulating the surface deficiency of materials and modulating the electronic structures for enhanced chemical activities. Catalytic materials with anion vacancies, such as oxygen, sulfur, and selenium, present less coordination number of surface atoms and more exposure of active sites, which may strongly interact with other components. In this case, vacancy structures play a crucial role in sulfur adsorption and conversion for Li–S batteries.[149]

Oxygen vacancies have been widely investigated because of the low formation energy. By tailoring oxygen vacancies, the conductivity of oxides can be improved due to the reduced bandgap. Oxygen vacancies may also generate new catalytic sites for SRR. Due to the facile synthesis and good catalytic activities of oxygen-deficient WO_3, Lin et al. controlled the oxygen deficiency content by heating treatment of $WO_3 \cdot H_2O$ nanoplates in hydrogen.[150] Two asymmetric cell configurations confirmed that surface oxygen deficiency in WO_{3-x} noticeably increased the polysulfide conversion kinetics. The introduction of oxygen vacancies to TiO_2 can further increase the conductivity and adsorption of polysulfides, which was demonstrated by Wang et al.[151] They designed nest-like CNT@TiO_{2-x} nanosheets for Li–S batteries with high energy density. Theoretical calculations indicated that the introduced oxygen vacancies strengthened the binding with polysulfides and accelerated the surface electron transport for fast redox. The surface vacancies in TiO_{2-x} nanosheets allowed abundant active sites for polysulfide adsorption and conversion. Another Ti_nO_{2n-1} quantum dot catalyst with high content of oxygen vacancies distributed on the porous carbon nanosheets was in situ prepared by Zhang et al. from an MXene precursor.[152] Oxygen vacancies boosted the catalytic conversion kinetics of polysulfides, achieving long-term cycling stability with 88% capacity retention over 100 cycles at 2.0 C.

Ferric oxides with oxygen vacancies own the merits of low cost, enhanced conductivity, and high catalytic activities, showing promising applications in Li–S batteries. Lv et al. synthesized Fe_2O_{3-x} nanoparticles by a facile solid lithiothermic reduction strategy.[153] By changing the lithium content, the concentration of oxygen vacancies was effectively tuned. Fe_2O_{3-x} nanoparticles displayed strong adsorption toward polysulfides and fast conversion, as illustrated in **Figure 12**a by a symmetric cell configuration. Compared with Fe_2O_3, Fe_2O_{3-x} decolored the Li_2S_6 solution after 12 h exposure, indicating the enhanced polysulfide adsorption by oxygen vacancy in Fe_2O_3 (Figure 12b). The cycle voltammetry (CV) of symmetric cells in Figure 12c shows that Fe_2O_{3-x} enabled a higher and sharper redox peak current than Fe_2O_3, implying the enhanced catalytic activity for the sulfur conversion kinetics. This observation was also validated by the EIS shown in Figure 12d. A smaller charge transfer resistance (R_{ct}) was found from the Fe_2O_{3-x} symmetric cell, implying facilitated charge transfer and improved conductivity by the oxygen vacancy in Fe_2O_{3-x}. Owing to the structural advantages, a small amount of Fe_2O_{3-x} nanoparticles can significantly increase the sulfur utilization of Li–S batteries. The resulting composite cathodes delivered an initial capacity of 1385 mAh g^{-1} at 0.1 C and a reversible capacity of 512 mAh g^{-1} over 500 cycles at 4.0 C with the capacity fade rate of 0.049% per cycle.

Wang et al. proposed another oxygen defect-rich Fe_2O_3 nanoparticle catalyst for the enhanced electrochemical kinetics in Li–S batteries.[154] The oxygen defect-rich Fe_2O_3 (ODFO) nanoparticles were uniformly distributed in a 3D S, N-codoped graphitic carbon matrix by a multi-ion-modulated hydrothermal reaction. ODFO nanoparticles significantly improved the lithium-ion transport in Li_2S. As a result, the ODFO-enhanced sulfur cathode exhibited a high capacity of 1489 and 644 mAh g^{-1} at 0.1 and 10.0 C, respectively. Moreover, sulfur cathodes with 11 mg cm^{-2} sulfur loading still delivered an areal capacity of 8.7 mA h cm^{-2} at 0.5 C, reaching the highest among reported metal-oxide-catalyzed sulfur cathodes. Other oxides with oxygen vacancies, like oxygen defect Co_3O_4,[155] RuO_{2-x},[156] In_2O_{3-x},[157] and $LaNiO_{3-x}$,[158] have also been employed as catalysts for Li–S batteries.

Sulfur vacancies have been introduced to Li–S batteries. Generally, the intrinsic conductivity of sulfides is higher than oxides, but their adsorption interaction with sulfur is relatively soft. Sulfur vacancies produce active sites for anchoring and catalyzing sulfur species and increase conductivity for fast electron transport. These two merits benefit the reaction kinetics of Li–S batteries. Lin et al. found that sulfur deficiencies on the surface of MoS_{2-x} nanoflakes significantly enhanced the polysulfide conversion kinetics.[21] A small amount of prepared MoS_{2-x}/reduced graphene oxide (4 wt%) catalysts enabled sulfur cathodes to deliver a high capacity of 827 mAh g^{-1} at 8.0 C. The enhanced SRR kinetics by sulfur-deficient MoS_{2-x} has been theoretically supported by Zhang et al. using DFT calculations.[159] Furthermore, Lin et al. moved on to the design of sulfur-deficient Co_9S_{8-x}.[160] Sulfur deficiencies were incorporated into the shell of Co_9S_8 nanospheres, resulting in a sulfur-deficient Co_9S_{8-x} shell with the Co_9S_8 core. When decorated on CNT, the obtained Co_9S_{8-x}/CNT can work as a catalytic interlayer for enhanced SRR kinetics, which effectively blocked the polysulfide diffusion and accelerated their conversion to discharging products. Sulfur cathodes with the Co_9S_{8-x}/CNT interlayer showed a low-capacity fade rate of 0.049% per cycle for 1000 cycles at 0.3 C. Other few-layered MoS_{2-x} nanosheets anchored inside the hollow mesoporous carbon were designed by Wang et al.[161] The ultrathin sulfur-deficient MoS_{2-x}

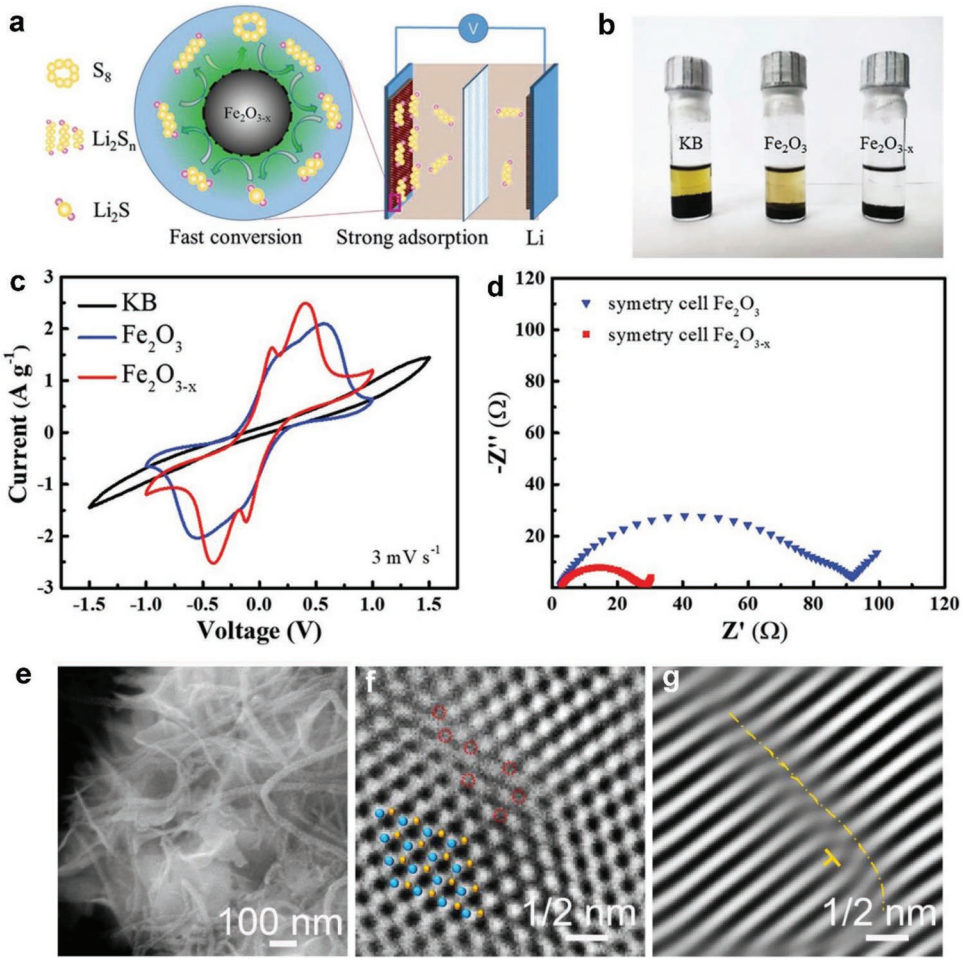

Figure 12. a) Schematic representation of a symmetric cell. b) Optical photograph of Li_2S_6 adsorption tests. c) Cyclic voltammograms of various symmetric cells. d) EIS of symmetric cells. Reproduced with permission.[153] Copyright 2020, Wiley-VCH. e) SEM image of $WSe_{1.51}$/CNT. f,g) IFFT patterns of a selected area ((f) in the overlaid crystal structures, blue circles represent W atoms, yellow circles Se atoms, and red circles Se defects; (g) yellow line marks a dislocation). Reproduced with permission.[164] Copyright 2022, Elsevier.

nanosheets chemically adsorbed polysulfides and catalyzed the fast redox conversion.

Selenides with selenium vacancies have been widely applied in Li–S batteries. Tian et al. synthesized Sb_2Se_{3-x} nanorods wrapped in rGO as sulfur barriers.[162] The introduction of selenium vacancies in Sb_2Se_{3-x} enhanced the intrinsic conductivity, promoted the chemical affinity to polysulfides, and catalyzed the rapid conversion of sulfur. Wang et al. revealed that $MoSe_2$ with selenium vacancies (SeVs−$MoSe_2$) properly worked as a precatalyst for SRR.[163] The interaction between polysulfides and SeVs−$MoSe_2$ induced the formation of MoSeS, which was responsible for the catalytic conversion of sulfur species. The reduction kinetics from Li_2S_2 to Li_2S can be promoted by MoSeS, hence achieving high sulfur utilization. Li et al. quantitatively investigated defective 2D WSe_2 with different W/Se ratios to reveal the effects of defects on the electrochemical kinetics of Li–S batteries.[164] With moderate defects, $WSe_{1.51}$ showed the optimal performance for adsorbing polysulfides and catalyzing the reduction conversion of sulfur species. $WSe_{1.5}$ was synthesized by a solvothermal method with CNT as conductive materials. The scanning electron microscopy (SEM) image in Figure 12e shows a 3D interlinked structure containing 2D $WSe_{1.5}$ and 1D CNT. The inverse fast Fourier transform (IFFT) results demonstrated the observable atomic point defects (Se vacancies) shown in Figure 12f. Besides, linear defects (edge dislocations) were found in the basal planes of $WSe_{1.5}$ with a strain field (Figure 12g). However, excessive defects led to the decreased catalytic activities because of the transformation of defect site configuration. Sulfur cathodes with $WSe_{1.51}$/CNT catalysts attained a high areal capacity of 11.3 mAh cm^{-2} when the sulfur loading was 12.7 mg cm^{-2}. A prolonged cycling stability over 1000 cycles at 1.0 C was achieved with a capacity fading rate of 0.025% per cycle. Other novel vacancies, like $Fe_{1-x}S$,[165] CoP with P vacancies,[166] and $NiTe_2$ with Te vacancies,[167] have been validated to accelerate the conversion kinetics of sulfur.

3.2.7. Morphology Engineering

Since catalytic efficiency is highly determined by the exposed actives sites on the surface of catalysts, the morphology

regulation of catalyst materials is vital to achieving optimized catalytic effects on SRR. Catalysts with various morphologies have been developed to improve the SRR kinetics, such as 1D nanotubes, 2D nanosheets, and 3D nanospheres/nanoboxes.[93,168,169] These structures with large specific areas and uniform pore distribution offer accessible space for the catalytic reactions of sulfur species. Moreover, they can also work as the support of catalyst materials to achieve the enhanced exposure of active sites.

1D nanostructures own high aspect ratios, which can provide a large surface area for catalytic reactions. Zhang et al. designed nanostructured VS_4 anchored on defect-rich carbon nanofibers as separator-modified layers to catalyze the conversion of sulfur species.[93] The defect-rich carbon nanofibers provided abundant active sites for the Li_2S deposition and enlarged the chemical adsorption of VS_4 toward polysulfides. Sulfur cathodes with 80% sulfur content delivered a high initial capacity of 1135 mAh g^{-1} at 0.2 C when using this separator-modified layer. In addition to 1D nanocarbon, carbon nitride (CN) nanotubes were adopted as matrices to load bimetallic CoFeP nanocrystals as Mott–Schottky catalysts (CoFeP@CN) for SRR.[170] The tubular geometry of CoFeP@CN composites facilitated the Li-ion transport, mitigated the volume variation during the battery cycling, and provided abundant lithiophilic/sulfiphilic sites for effective anchoring of polysulfides. As a result, CoFeP@CN catalysts enabled sulfur cathodes to achieve a high-rate capability of 630 mAh g^{-1} at 5 C. By coaxial electrospinning and selective vulcanization, Li et al. developed CoS_2—TiO_2@C core–shell fibers as sulfur host.[133] The porous core–shell structures offered a large space for sulfur loading. The TiO_2@C shells realized fast electron conduction and enhanced the chemical adsorption of polysulfides, while the CoS_2 cores promoted the redox kinetics of sulfur cathodes. Benefiting from the combined effects, sulfur cathodes with CoS_2—TiO_2@C delivered an initial capacity of 1181 mAh g^{-1} at 0.2 C and maintained a high capacity of 737 mAh g^{-1} at 1.0 C after 300 cycles.

Various 2D structures have been designed to enlarge the exposure of catalytic sites.[132,171] Owing to the excellent conductivity and tunable surface structures, 2D MXenes exhibit good acceleration for the SRR kinetics. Combining the strong anchoring of TiO_2 toward polysulfides, Jiao et al. designed in situ built TiO_2—MXene heterostructures to achieve the effective capture and catalytic conversion of polysulfides.[132] Moreover, 2D MOF nanosheets have been proposed by Meng et al. as catalysts for SRR because of the highly exposed catalytic active surfaces and rapid charge transport along the 2D sheets.[168] The developed bimetal CoNi—MOF possessed two catalytic centers, resulting in synergistic catalytic activities for the reduction of long-chain polysulfides and Li_2S deposition. CoNi—MOF considerably decreased the reaction activation energies of SRR, which was attributed to the charge redistribution between Ni and Co via bridge O. Sulfur cathodes with CoNi—MOF showed a high reversible capacity of 1450 mAh g^{-1} at 0.1 C. Based on the excellent properties of graphene, Yu et al. anchored MoP quantum dots on N, P-doped graphene (MPQ@G) as efficient catalysts for the polysulfide conversion.[171] The N, P-doped graphene worked as a conductive substrate to load MoP QDs, which significantly enlarged the catalytic sites of MoP QDs for the enhanced conversion kinetics of polysulfides. The resulting MPQ@G/S cathodes delivered an initial capacity of 1220 mAh g^{-1} at 0.2 C.

Shi et al. further exploited the advantages of graphene as catalyst substrates. They designed a Mott–Schottky heterogeneous layer of rGO—polyaniline (PANI)/MoS_2 (RPM) to achieve successive "trapping–interception–conversion" toward polysulfides.[90] The fabrication and structures of RPM are shown in **Figure 13**a. The 2D MoS_2 nanosheet arrays were vertically anchored at the surface of rGO—PANI substrates via Mo—N/Mo—S bonds, which formed a heterointerface layer of MoS_2/MoN. When working as separator-modified layers in Li–S batteries (Figure 13b), RPM greatly enhanced the sulfur utilization by the synergistic effects. The vertical MoS_2 nanosheet arrays generated a "reservoir" structure to accommodate sulfur. The MoS_2/MoN heterointerfaces provided strong adsorption toward sulfur species, increasing the trapping and interception effects. Furthermore, such heterointerfaces accelerated the liquid–solid conversion from polysulfides to Li_2S, resulting in fast SRR kinetics. Besides, the conductive rGO—PANI substrates provided rapid access to continuous electron transport. Benefiting from these structural advantages, the RPM-modified separators exhibited an excellent rate stability and capability for Li–S batteries. At 5.0 C, an initial capacity of 947 mAh g^{-1} was achieved and remained at 524 mAh g^{-1} after 700 cycles. A high capacity of 553 mAh g^{-1} was obtained even at 10 C.

The diversity of 3D structures enables various strategies to develop efficient catalysts for SRR. Wang et al. designed perovskite bimetallic hydroxide $CoSn(OH)_6$ nanocages wrapped by rGO as catalysts (G@CSOH) for SRR.[169] As shown in Figure 13c, $CoSn(OH)_6$ nanocubes were initially fabricated by a coprecipitation method. Then, an etching process resulted in the formation of hollow nanocages. Followed by the graphene coating, the final G@CSOH was prepared. The hollow structure can be observed from the TEM image in Figure 13d. $CoSn(OH)_6$ nanocages were tightly wrapped by the interconnected rGO nanosheets (Figure 13e). Sn, Co, and C elements were uniformly dispersed in nanocages (Figure 13f). Due to the balanced valence states of Co and Sn in $CoSn(OH)_6$, the bimetallic hydroxide exhibited moderate adsorption ability toward polysulfides and enhanced catalytic activities for SRR. In addition, the hollow structure and the wrapped rGO worked as double physical barriers and provided continuous electrical pathways, effectively suppressing the shuttle effect and enhancing charge transfer. Li–S batteries with this sulfur host delivered a high capacity of 644 mAh g^{-1} at 2.0 C, as well as a prolonged cycling stability over 600 cycles at 1.0 C with only the 0.068% capacity decay per cycle.

Hollow spheres is another promising catalyst support. Yang et al. synthesized hollow N-doped carbon spheres (NHCS) decorated with nanosized SnS_2 (NHCS—SnS_2) to catalyze the electrochemical conversion of sulfur.[92] Highly conductive NHCS provided a porous 3D network to accelerate electron transport and electrolyte infiltration. The high dispersion of nanosized SnS_2 at the NHCS surface enlarged the number of active sites for adsorbing polysulfides and facilitated the Li_2S deposition. Consequently, the resulting NHCS—SnS_2/S cathodes delivered a high capacity of 1344 mAh g^{-1} at 0.2 C. Moreover, Yu et al. designed amorphous N-doped carbon/MoS_3

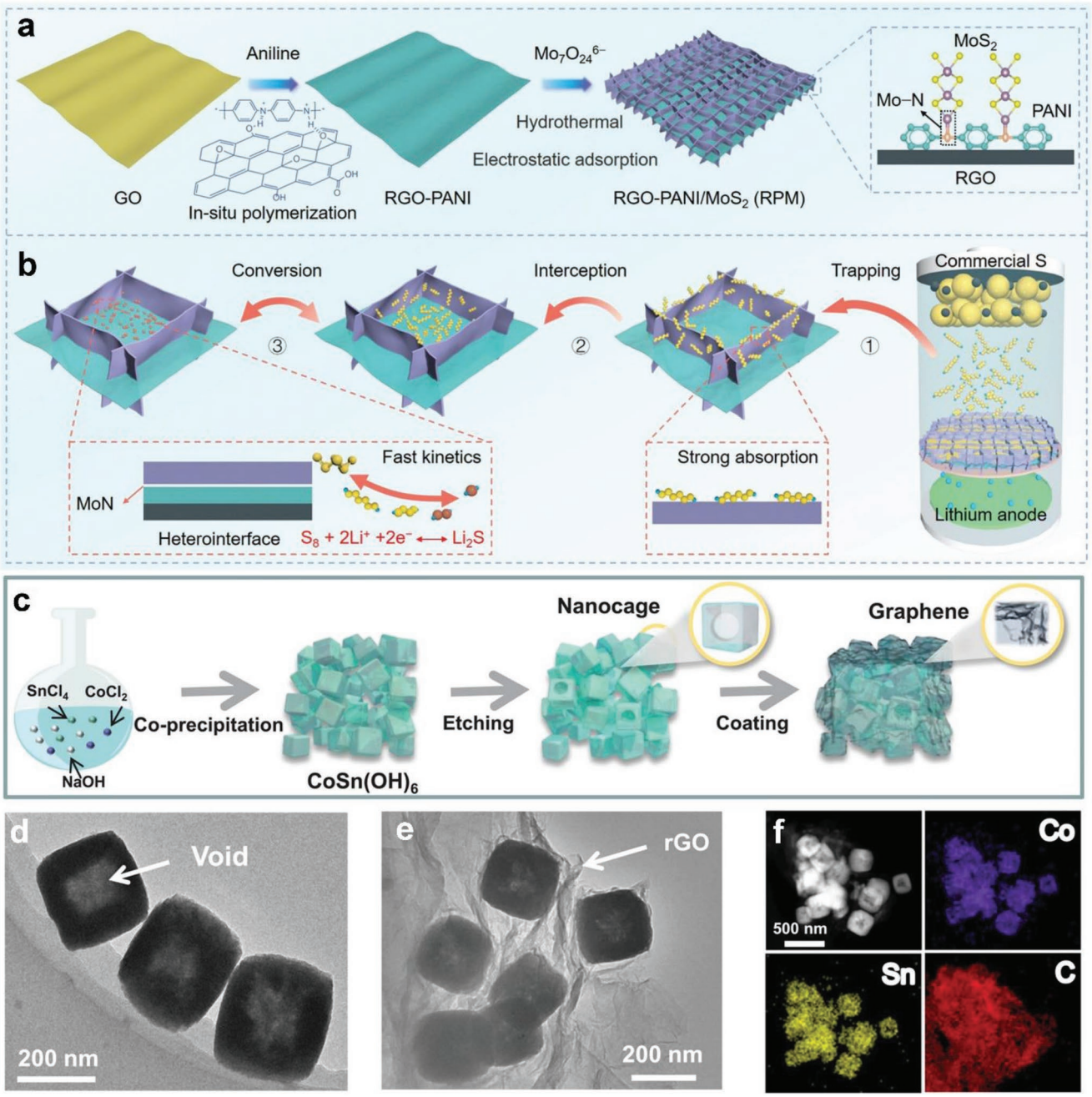

Figure 13. a) Schematic illustration of the fabrication of RPM. b) RPM-modified separator for the enhanced sulfur utilization. Reproduced with permission.[90] Copyright 2022, Wiley-VCH. c) Schematic illustration of the G@CSOH synthesis. TEM images of d) CSOH and e) G@CSOH. f) HAADF-STEM and the corresponding elemental mappings of G@CSOH. Reproduced with permission.[169] Copyright 2021, Wiley-VCH.

(NC/MoS_3) nanoboxes with hollow porous structures as catalysts for SRR.[91] The hollow nanoboxes guaranteed high sulfur loading and physically confined the diffusion of polysulfides. Meanwhile, the amorphous MoS_3 possessed the unsaturated coordination of Mo and electron-rich S, causing the strong binding capability toward polysulfides and the improved catalytic effects on SRR. As a result, sulfur cathodes with NC/MoS_3 nanoboxes maintained a capacity of 752 mAh g^{-1} after 500 cycles at 0.5 C.

3.3. Metals

Metals show excellent catalytic activities for many reactions. Noble metals, like Pt, were initially investigated for accelerating the conversion kinetics of polysulfides.[20] From then on, other noble or transition metals, such as Ir,[172] Ru,[173] Co,[174] and Fe,[175] have demonstrated improved catalysis effects on sulfur conversion kinetics. The enhanced battery performance obtained with various metals is summarized in **Table 3**.

Table 3. Summary of metal catalysts increasing the performance of Li–S batteries.

Catalysts	Sulfur content[a)] [wt%]	Sulfur loading [mg cm^{-2}]	Current rate [C]	Cycle number	Initial capacity [mAh g^{-1}]	Retained capacity [mAh g^{-1}]	Refs.
Co clusters	61	1.8	0.1	100	1380	1150	[179]
			1.0	500	912	780	
Co nanoparticles	–	2.0	0.2	200	1093	986	[180]
			3.0	500	627	508	
Co nanoparticles	60	≈1.5	1.0	500	909	657	[182]
Co nanoparticles	60	1.0	0.2	100	1172	980	[186]
			1.0	500	≈1100	660	
Co nanoparticles	70	1.0	0.2	100	1393	1035	[187]
			1.0	1000	1261	625	
Fe nanoparticles	64	–	0.5	300	≈1050	827	[175]
			2.0	500	750	526	
Bi nanoparticles	56	1.2–1.6	0.5	100	1157	970	[188]
			1.0	500	1010	811	
Ag nanoparticles	53	≈1.3	0.5	200	1294 (0.1 C)	849	[189]
			2.0	550	918	652	
CoFe alloy	53	1.0	0.1	100	1226	1158	[192]
			1.0	300	890	770	
CoFe alloy	–	1.0	0.2	100	1300	1170	[193]
			5.0	300	1034	870	
CoFe alloy	70	1.0	0.2	100	1264	986	[195]
			1.0	1000	914	457	
NiFe alloy	73	4.1	0.2	200	≈1000	≈800	[197]
			1.0	800	≈950	≈600	
ZnPd alloy	60	1.2	1.0	500	916	627	[198]
High-entropy alloy	80	1.0–2.0	2.0	500	816	680	[199]

[a)]Sulfur content in cathodes.

3.3.1. Cobalt Metals

Co is the most investigated metal as a catalyst for Li–S batteries. Generally, Co is combined with N as dopants in carbon to enlarge the number of active sites. MOFs are excellent precursors to fabricate carbon nanostructures with Co, N doping by facile pyrolysis. Fang et al. employed Co—MOF (ZIF-67) to prepare a Co, N-doped carbonaceous composite.[176] Co and N heteroatoms strengthened the interaction with polysulfides and accelerated the reaction kinetics. The conclusion was also supported by Li et al., who developed honeycomb-like mesoporous Co, N-doped carbon NSs (MC-NSs) using the same ZIF-67 precursors.[177] Similarly, a Co—N—C sulfur host (Co—-NGC@NCNF) comprising Co-embedded N-doped graphitic carbon (Co—NGC) decorated at freestanding N-doped carbon nanofibers (NCNF) was reported.[174] The authors grew ZIF-67 layers at the surface of polyacrylonitrile nanofibers produced by electrospinning. Followed by pyrolysis, the targeted Co—NGC@NCNF was obtained. The Co-embedded N-doped graphitic carbon acted as bifunctional catalytic center, which simultaneously accelerated the kinetics of SRR and Li_2S oxidation.

Qian et al. pyrolyzed melamine sponge loaded with ZIF-67 to prepare functional interlayers for enhanced polysulfide conversion.[178] The Co nanoparticles embedded in the skeleton exhibited high catalytic activities, effectively promoting the Li^+ transfer, polysulfide reduction, and Li_2S deposition. The improved SRR kinetics under the lean electrolyte (E/S ratio of 7 mL g^{-1}) was achieved. In addition, pyrolysis of ZnCo—ZIF can also lead to Co nanoparticles decorated on carbon. For example, N-doped porous carbon nanocages with uniformly dispersed Co clusters can be fabricated by carbonizing glucose adsorbed ZnCo—ZIF.[179] Moreover, Wang et al. annealed CoZn—ZIF-loaded melamine foam composite monolith, forming interconnected 3D conductive Co/Co—N_x-codoped CNT arrays on carbon foam (Co—NCNT@CF).[180] Both materials exhibited enhanced catalytic conversion kinetics of polysulfides and improved sulfur utilization with high electrochemical performance in Li–S batteries.

SRR involves multistep reaction processes. An individual catalyst may not achieve the whole catalytic conversion. Ye et al. therefore combined Fe—N- and Co—N-codoped carbons to specifically catalyze sulfur reduction to polysulfides and subsequent Li_2S deposition, respectively.[181] Both catalysts can be readily prepared from the pyrolysis of their Prussian blue precursors. The two catalysts operated in sulfur cathodes in a dual-layer configuration, where polysulfides formed in the inner layer were catalytically reduced to Li_2S by the outer layer facing the electrolyte. As shown in **Figure 14**a, Fe—N@C catalysts presented an elevated and longer first discharging plateau, indicating the promoted reduction kinetics from sulfur to polysulfides. This phenomenon can also be confirmed by the positive shift of the first cathodic peak in the linear sweep

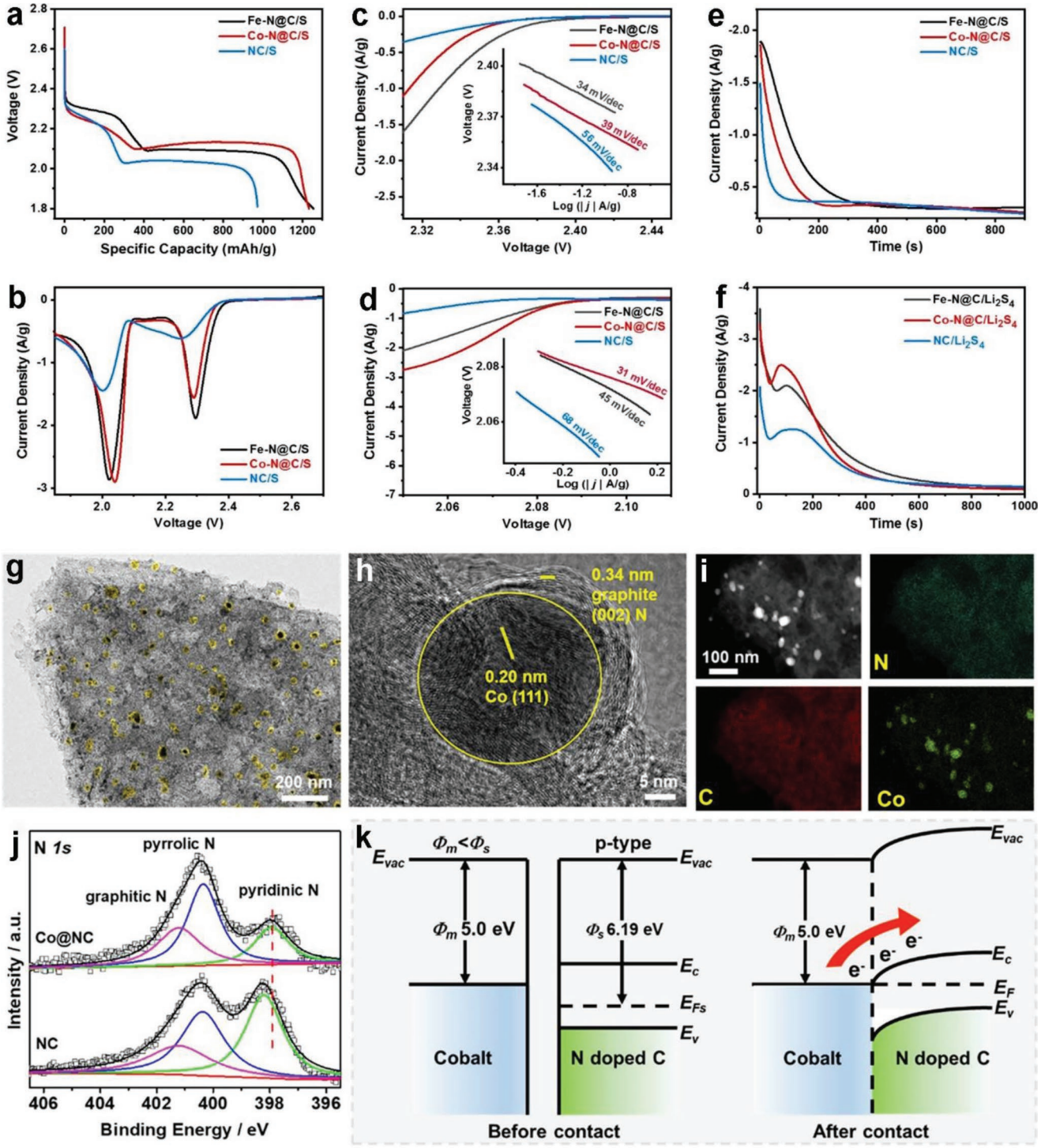

Figure 14. a) Voltage profiles of Fe—N@C, Co—N@C, and NC at 0.1 C. b) LSV between 1.8 and 2.8 V at a scan rate of 0.2 mV s^{-1}. c,d) Polarization curves from the LSV measurements with the derived Tafel plots as insets. e) Potentiostatic (2.2 V) discharge with sulfur as active initial material. f) Potentiostatic (2.0 V) discharge with Li_2S_4 as active initial material. Reproduced with permission.[181] Copyright 2019, American Chemical Society. g) TEM, h) HRTEM, i) HAADF images, and the corresponding EDX mapping results of the Co@NC heterostructure. j) N 1s XPS spectra of NC and Co@NC. k) Schematic illustration of a Mott–Schottky type contact of Co@NC before and after contacting. Reproduced with permission.[182] Copyright 2021, American Chemical Society.

voltammetry (LSV) and a smaller Tafel slope (Figure 14b,c). Nevertheless, Co—N@C catalysts were more efficient in reducing polysulfides to Li_2S with a longer second discharging plateau, a positive shift of the second cathodic peak, and a smaller Tafel slope (Figure 14b,d). Based on the potentiostatic discharging transients shown in Figure 14e,f, it can be concluded that

Fe—N@C catalysts showed the largest capacity of Li_2S_4 reduction and Co—N@C revealed the largest capacity for Li_2S deposition. Therefore, Fe—N@C and Co—N@C synergistically accelerated the kinetics of SRR.

Co metals coupled with other semiconductors form Mott–Schottky heterojunctions, which can act as good catalyst with optimized interfacial electronic interactions. To reveal the Mott–Schottky effects on the conversion kinetics of Li–S batteries, Li et al. designed a paradigmatic Co@NC heterostructure consisting of Co nanoparticles encapsulated in a porous N-doped carbon matrix as sulfur host.[182] The 2D Co@NC displays a porous and rough surface in Figure 14g. HRTEM of Co@NC in Figure 14h indicates the (111) plane of metallic cobalt with a lattice fringe of 0.20 nm. Co nanoparticles were uniformly distributed inside the porous carbon matrix, as found by energy-dispersive X-ray spectroscopy (EDX) in Figure 14i. The N 1s X-ray photoelectron spectroscopy (XPS) spectrum in Figure 14j confirms the successful incorporation of N into the carbon matrix. As the N-coped carbon possessed a p-type semiconductor structure with a calculated work function of 6.19 eV, the electron will spontaneously flow to the N-coped carbon after coming into contact with the metallic Co with a smaller work function of 5.00 eV (Figure 14k). This Mott–Schottky effect caused the self-driven charge density distribution at the interface of the heterostructures. The electron injection from the surface Co atoms to adjacent N atoms of N-doped carbon formed a built-in electric field toward N-doped carbon, which benefited the chemical binding to polysulfides, enhanced charge transport, and reduced the energy carriers of SRR. The catalytic merits of Co@NC due to the Mott–Schottky effect helped Li–S batteries to reach a gravimetric energy density of 308 Wh kg^{-1} under the ultrahigh 10.7 mg cm^{-2} sulfur loading and lean electrolyte conditions of only 5.9 µL mg^{-1}. Other SRR catalysts involving Co metals, included NCNT@Co—Co_3O_4 nanowire array,[183] Co nanoparticles embedding in N-doped ultrathin carbon nanosheets,[184] N-doped carbonaceous scaffold anchored with Co nanoparticles,[185] Co-embedded hierarchically porous hollow carbon microspheres,[186] and Co nanoparticles embedded into N-doped hierarchical porous carbon.[187]

3.3.2. Other Metals

Fe is another promising metal to catalyze SRR. Zeng et al. reported a highly graphitized carbon tube with rich Fe and N sites (Fe/N—g-CT) to catalyze the electrochemical reactions in Li–S batteries.[175] They found that the introduced Fe promoted the formation of graphitized CT and worked as catalytic sites for SRR with enhanced Li_2S deposition. Due to the high electrical conductivity and catalytic activity, Fe/N—g-CT enabled a high sulfur utilization with an initial specific capacity of 1500 mAh g^{-1} at 0.1 C. Ru has also been confirmed as an effective catalyst for fast conversion from Li_2S_2 to Li_2S. The prepared Ru nanoparticles with a size below 3 nm, decorating porous hollow carbon spheres, were found to reduce the interfacial resistance of sulfur cathodes.[173] Li–S batteries with C—Ru—S cathodes delivered an improved capacity of 1200 mAh g^{-1} at 0.1 C for 100 cycles.

Zuo et al. proposed a modified separator composed of Ketjen-Black-loaded Ir nanoparticles to catalyze the conversion reaction of polysulfides.[172] Ir nanoparticles exhibited a strong chemical interaction with polysulfides, efficiently accelerating the conversion kinetics of polysulfides to Li_2S_2/Li_2S. Li–S batteries with these modified separators achieved an initial capacity of 1508 mAh g^{-1} at 0.2 C. Zhao et al. embedded ultrafine Bi nanoparticles in porous N-doped carbon nanorods (Bi—NC) to construct an efficient sulfur host.[188] The introduced Bi nanoparticles caused the local charge rearrangement of Bi—NC with optimized electronic structure, significantly improving the polysulfide conversion. The resulting Bi—NC/S cathodes delivered an initial capacity of 1157 mAh g^{-1} at 0.5 C. In addition, Ag-decorated N-doped carbon was prepared by Zhang et al. as an interlayer for Li–S batteries.[189] The high conductivity and excellent catalytic conversion to polysulfides allowed sulfur cathodes to offer a superb storage capability of 579 mAh g^{-1} at 5 C.

3.3.3. Alloys

Alloy nanoparticles can integrate the advantages of the separate metal components, achieving enhanced catalytic activities. The excellent catalytic activity of CoFe alloys has attracted tremendous attention. Using a facile carbonization treatment of Prussian blue analogs, Li et al. fabricated FeCo alloys in situ anchored to porous carbon (FeCo—C) acting as good sulfur host material.[190] It was found that the FeCo alloy nanoparticles chemically confined polysulfides by a Lewis acid–base interaction, catalyzed the redox conversion of sulfur species, and provided fast electron transfer pathways for good rate capability. The resulting S/FeCo—C cathodes presented an initial capacity of 792 mAh g^{-1} at 2.0 C and maintained 503 mAh g^{-1} after 500 cycles. FeCo alloys loading other carbon matrices have also been reported. Shi et al. designed a CoFe alloy decorated with mesoporous carbon spheres (CoFe—MCS) to catalyze the polysulfide conversion.[191] The 3D-printable S@CoFe—MCS electrodes achieved a high areal capacity of 6.0 mAh cm^{-2} for Li–S batteries with a sulfur loading of 7.7 mg cm^{-2}. Cao et al. prepared CoFe nanoparticles coated in N-doped carbon shells (E-CoFeCN@C).[192] The uniform Co—Fe alloy catalytic and absorptive sites gave rise to improved redox kinetics of sulfur cathodes. Besides, Gao et al. designed a freestanding 3D porous-carbon-film-embedded CoFe alloy nanoparticle.[193] They demonstrated that CoFe alloys worked as efficient catalyst for fast polysulfide conversion, enabling Li–S batteries with an enhanced capacity of 836 mAh g^{-1} at 0.2 C with a capacity retention rate of 94.5% after 100 cycles at a low temperature of –20 °C.

FeCo-alloy-functionalized separators have also shown catalytic effects on the polysulfide redox conversion.[194,195] By a facile bimetal–organic framework pyrolysis strategy, Hu et al. developed N-doped carbon-layer-enveloped CoFe alloy (CoFeCN@C) nanoparticles as multifunctional separators for Li–S batteries.[195] The synthesized CoFeCN@C was determined to be a body-centered cubic structure of CoFe alloys (**Figure 15**a) with a sphere shape (Figure 15b). The CoFe alloy inner core presented an average size of 12 nm and the thickness of the outer carbon shell was about 7 nm (Figure 15c,d). The EDX mapping (Figure 15e) shows a uniform distribution of Co and Fe within the N-doped carbon shell. Co and Fe K-edge

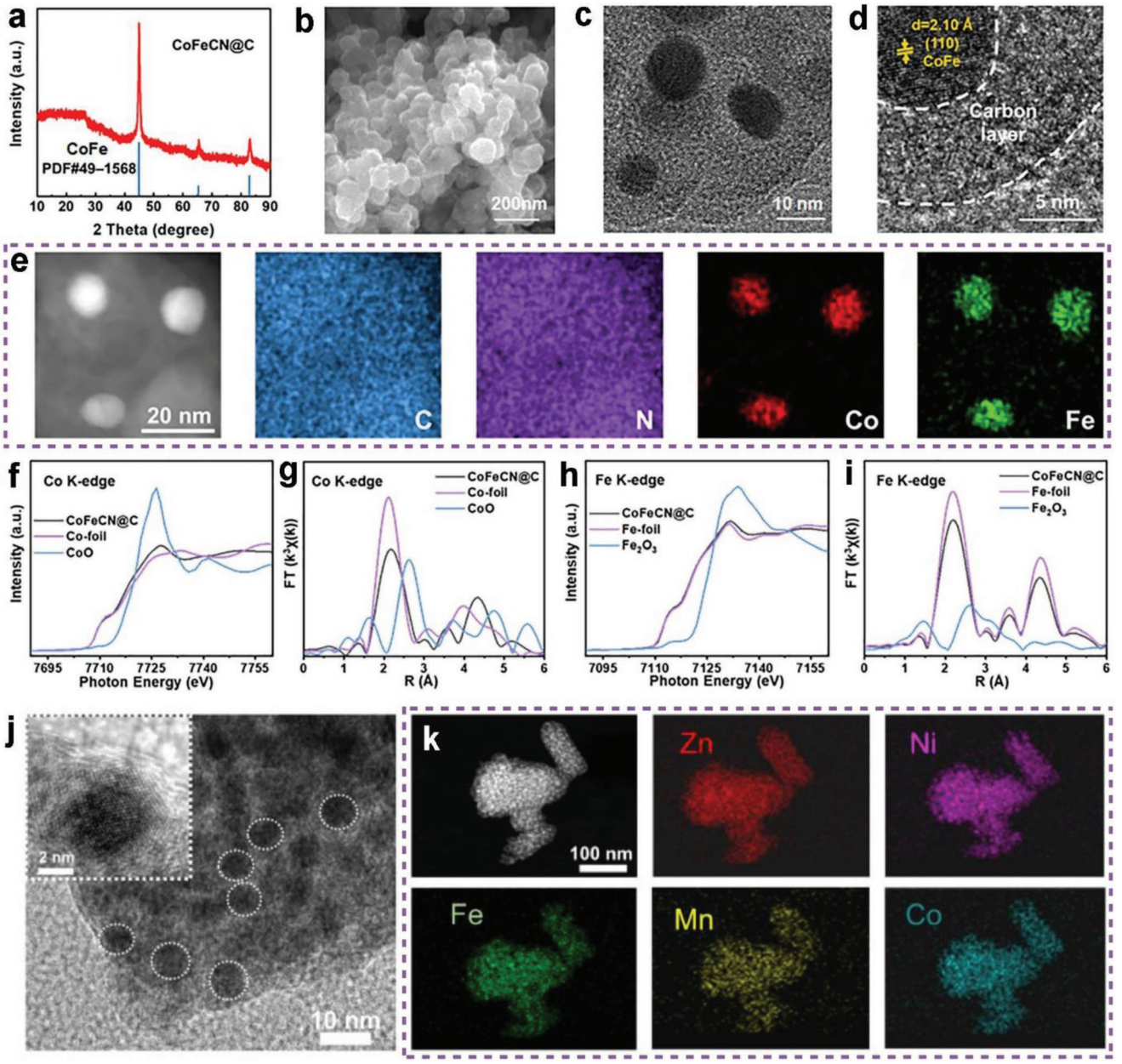

Figure 15. a) XRD pattern, b) SEM, and c) HRTEM images of CoFeCN@C. d) Enlarged image of (c). e) The corresponding EDX mappings of CoFeCN@C. f) Co K-edge XANES and g) FT-EXAFS in *R* space of CoFeCN@C. h) Fe K-edge XANES and i) FT-EXAFS in *R* space of CoFeCN@C. Reproduced with permission.[195] Copyright 2021, Elsevier. j) STEM image showing the dispersed nano-HEA particles (inset: zoom-in STEM image). k) HAADF image and the elemental mappings, showing uniform mixing of five metal components. Reproduced with permission.[199] Copyright 2021, Elsevier.

X-ray absorption fine structure revealed the electronic and coordination structures of CoFeCN@C. As shown in Figure 15f,h, the Co and Fe K-edge XANES spectra of CoFeCN@C display similar pre-edge structures with that of the metal foils, indicating the metallic valence states of Co and Fe in CoFeCN@C. The corresponding Fourier-transformed (FT)-EXAFS spectra of Co and Fe in Figure 15g,i display one main peak at about 2.2 Å, resulting from the oscillation of the first coordination shell of Co—Co/Fe and Fe—Fe/Co bonds. CoFe alloys provided sufficient adsorptive and catalytic sites for sulfur species, simultaneously accelerating the multiphase conversion of SRR. Sulfur cathodes with CoFeCN@C-modified separators delivered an initial discharge capacity of 1264 mAh g^{-1} at 0.2 C.

In addition to CoFe alloys, CoSn,[196] FeNi,[197] and ZnPd[198] alloys have also been applied in Li–S batteries to catalyze the sulfur conversion. All these alloys were supported by carbon matrices to obtain enhanced catalytic effects. Qiao et al. synthesized hollow Co_xSn_y-modified N-doped carbon as sulfur host for Li–S batteries via a stepwise coating–etching approach.[196] The strong chemisorption and electrocatalytic conversion activity for polysulfides allowed sulfur cathodes to reach a high capacity of 1006 mAh g^{-1} after 100 cycles at 0.2 C.

He et al. found that FeNi alloys with a hexagonal close-packed structure showed catalytic activities for polysulfide conversion.[197] Pouch cells fabricated with FeNi/S cathodes achieved stable cycling performance under a low E/S ratio of 4.5 μL mg^{-1}. Zhou et al. reported a MOF-derived ZnPd alloy.[198] They demonstrated that Zn effectively induced the rapid transfer of lithium ions, and Pd enabled adsorption and catalytic conversion of polysulfides.

Xu et al. developed a nano-high-entropy-alloy (nano-HEA) composed of Fe, Co, Ni, Mn, and Zn five elements as catalyst for Li–S batteries.[199] The nano-HEA was prepared through fast carbothermal reduction of a multimetal MOF-74 precursor. As shown in Figure 15j, the nano-HEA particle exhibits an average size of 7–10 nm. Five metal components are homogeneously distributed in the nano-HEA particles (Figure 15k). The enhanced catalytic activities of HEA for SRR were related to the optimized redistribution of surface charges, as demonstrated by the experimental results and DFT calculations. Zn acted as electron reservoir and Mn dominated the conduction band to be the electron consumption center. Ni, Fe, and Co helped to form a uniform charge redistribution at the HEA surface. The synergetic effects contributed to the accelerated multielectron SRR. The resulting Li–S batteries with nano-HEA-modified separators maintained a capacity of 680 mAh g^{-1} after 500 cycles at 2.0 C with 83.3% capacity retention.

3.4. Single Atoms

The introduction of catalyst materials to Li–S batteries can, on the one hand, increase sulfur utilization and, on the other hand, decrease the energy density because of the introduction of nonactive components. The optimal use of catalysts will benefit Li–S batteries to reach a high energy density. Therefore, single atoms (SAs), which are atomically dispersed metal atoms, have attracted high attention due to the maximized atom utilization efficiency. The content of single atoms used in Li–S batteries can be reduced to below 10% in terms of the whole cathode mass. Besides, the unsaturated coordination environment and unique electronic structures allow single atoms distinct advantages in catalysis. As single atoms are extremely active with high free energies, they typically coordinate with other atoms (e.g., N and O) to keep the structural stability. Considering the structural flexibility of carbon materials and their merits when applied in Li–S batteries, single atoms anchored on various carbon substrates display excellent catalytic activities in sulfur redox reactions.[200]

A series of single atoms have been developed via different preparation approaches as catalysts for Li–S batteries, such as single-atom Fe[201–203] and Co.[204–206] Due to the ultrasmall size of single atoms, direct morphology observation is performed by aberration-corrected high-angle annular dark-field scanning transmission electron microscopy (HAADF-STEM) with sub-Ångström resolution. Furthermore, the chemical states and coordination environment of single atoms can be determined by XAS, e.g., XANES and EXAFS. **Table 4** summarizes the various single-atom catalysts that increase the electrochemical performance of Li–S batteries.

3.4.1. Single-Atom Fe

Single-atom Fe dispersed at N-doped carbon has been widely reported to catalyze the electrochemical reaction of sulfur cathodes.[201,207] The typical fabrication method involves pyrolyzing the mixtures of various N-doped carbon sources and metal salts. For example, Wang et al. carbonized PANI-coated carbon with the iron acetate precursor at 700 °C to obtain single-atom Fe catalyst in N-doped carbon.[202] These authors, for the first time, demonstrated the effects of single-atom catalysts on enhancing the electrochemical conversion kinetics in Li–S batteries. When the catalyst was incorporated into nanostructured Li_2S cathodes, the fabricated Li_2S/Li batteries achieved a superior high-rate performance at 12 C and a long cycle life at 5 C. Lu et al. selected g-C_3N_4 as catalyst support to coordinate with single-atom Fe (SAFe@g-C_3N_4).[208] The abundant N sites of g-C_3N_4 enabled a high single-atom loading of 8.5 wt% in the catalyst. DFT calculations revealed that single-atom sites reduced the energy barriers of the polysulfide conversion, thus improving the battery rate capability. Li–S batteries with SAFe@g-C_3N_4 displayed a high reversible specific capacity of 1379 mAh g^{-1} at 0.1 C under a lean-electrolyte condition (a low E/S ratio of 3.8). Zhao et al. dispersed single-atom Fe at N, S-doped porous carbon (FeNSC).[209] The synergy between single-atom Fe and doped sulfur accelerated the reversible electrochemical conversion in Li–S batteries. The FeNSC/S cathodes exhibited a low-capacity decay of only 0.047% per cycle over 1000 cycles at 1.0 C.

The catalytic activity of single atoms strongly depends on the coordination environment. The four-coordinated structure of the $M-N_4$ (M refers to metal) configuration with high structural stability is the typical active site for SRR. For instance, Ma et al. constructed single-atom Fe and Fe_2N nanocrystals codecorated at N-doped graphene (SA-Fe/Fe_2N@NG), in which SA-Fe has a plane-symmetric Fe-4N coordination and Fe_2N has a triangular pyramidal Fe-3N coordination.[210] The SA-Fe and Fe_2N operated as synergistic sites, enhancing the sulfur anchoring and accelerating the liquid–solid conversion between polysulfides and Li_2S. Li–S batteries with SA-Fe/Fe_2N@NG-modified separators exhibited high-capacity retention of 84.1% over 500 cycles at 1.0 C. Despite the structural stability, the four-coordinated configuration of single atoms may not exhibit the most optimal catalytic effect on Li–S batteries. Controlling the coordination environment can further enhance the catalytic activities of single atoms. In this case, Zhang et al. precisely synthesized a novel single-atom catalyst with oversaturated $Fe-N_5$ coordination structure ($Fe-N_5-C$) via a absorption–pyrolysis process using predesigned conjugated micro-/mesoporous polymer precursors.[211] DFT calculations demonstrated that the excessive N coordination number of $Fe-N_5-C$ was expected to show enhanced polysulfide adsorption compared with $Fe-N_4-C$. In addition, the energy barrier of Li-ion migration at the surface of $Fe-N_5-C$ was distinctly lower than $Fe-N_4-C$, implying enhanced ion transfer due to the increased N coordination. Consequently, the S/$Fe-N_5-C$ cathode exhibited an initial capacity of 1224 mAh g^{-1} at 0.2 C and maintained 662 mAh g^{-1} after 500 cycles at 1 C.

In addition to the oversaturated coordination, the deficiency in $Fe-N_4$ coordination can also generate distinct active sites for Li–S batteries.[212] Qiu et al. selected CN as the support

Table 4. Summary of single-atom catalysts increasing the performance of Li–S batteries.

Catalysts	Sulfur content[a)] [wt%]	Sulfur loading [mg cm^{-2}]	Current rate [C]	Cycle number	Initial capacity [mAh g^{-1}]	Retained capacity [mAh g^{-1}]	Refs.
Single-atom Fe	–	2.3	0.2	200	1255	1129	[208]
			2.0	1000	915	624	
Single-atom Fe	52	1.0	1.0	1000	905	477	[209]
Single-atom Fe	70	≈1.5	0.2	200	1242	999	[210]
			1.0	500	951	800	
Single-atom Fe	59	1.0	0.2	100	1124	920	[211]
			1.0	500	907	662	
Single-atom Fe	56	1.3–1.5	0.2	100	1227	1104	[213]
			2.0	2000	795	620	
Single-atom Fe	60	≈1.5	0.2	100	1397	1176	[214]
			1.0	500	899	800	
Single-atom Co	68	2.0	1.0	500	927	681	[204]
Single-atom Co	56	≈1.0	0.5	700	871	571	[205]
Single-atom Co	54	–	0.1	150	1418	1182	[206]
			1.0	500	1113	1003	
Single-atom Co	–	3.5	0.2	600	≈1000	≈500	[218]
Single-atom Co	56	1.2	1.0	1000	1038	675	[220]
		4.9	0.2	120	1062	871	
Single-atom Co	–	2.8	0.5	200	850	682	[221]
		1.0	1.0	500	≈950	700	
Single-atom Ni	–	1.3–1.6	0.5	500	1086	798	[223]
Single-atom Zn	–	1.0	0.2	100	≈1230	1079	[226]
			1.0	800	932	680	
Single-atom Mo	65	2.0	1.0	200	912	≈900	[227]
			2.0	550	831	817	
Single-atom V	68	2.0	0.2	100	≈1200	770	[228]
			0.5	400	780	551	
Single-atom W	75	1.1	1.0	500	1063	691	[229]
Single-atom Ru	64	≈1.2	0.2	100	≈1200	992	[230]
			1.0	800	≈800	≈500	

[a)]Sulfur content in cathodes.

to construct the unsaturated Fe—N_2 coordination structure (Fe—N_2/CN).[213] CN offered abundant and uniform pyridine N to control the coordination of Fe single atoms. The homogeneous distribution of Fe, C, and N elements of Fe—N_2/CN has been demonstrated by elemental mapping (**Figure 16**a). HAADF-STEM in Figure 16b shows numerous individually distributed bright dots in the CN nanosheet, which are identified as dispersed Fe atoms with a size of about 2 Å. The Fe K-edge XANES spectrum of Fe—N_2/CN in Figure 16c indicates the similar absorption near edge to that of Fe_2O_3, suggesting the positive valence state of Fe in Fe—N_2/CN. Furthermore, the Fourier-transformed Fe K-edge EXAFS curve of Fe—N_2/CN (Figure 16d) shows a distinct peak at about 1.5 Å, corresponding to the Fe—N(O) scattering path. The absence of the Fe—Fe peak from the standard Fe foil demonstrated the atomically dispersed Fe atoms in the CN matrix via Fe—N coordination. The calculated coordination number of Fe in Fe—N_2/CN was 2.1 according to the fitting EXAFS curves in Figure 16e,f. Such unsaturated Fe—N_2 sites not only provided strong adsorption toward polysulfides, but also accelerated the reversible conversion from sulfur to Li_2S. Consequently, the Fe—N_2/CN@S composite cathodes delivered a high capacity of 1451 mAh g^{-1} at 0.1 C and a capacity decay of 0.011% per cycle over 2000 cycles at 2.0 C.

The enhanced catalytic activity of coordinatively deficient single-atom Fe—N_2—C configuration has been further validated by Wang et al.[214] The authors selected pristine phthalocyanine iron (FePc, FeN_4) and N-deficient FePc (FeN_2) structures as representatives to predict the adsorption and catalytic activities via DFT calculations. Because of the strong hybridization between the Fe $3d_{zz}$ and S $3p_y$ orbitals, the FeN_2 configuration displayed enhanced polysulfide adsorption and facilitated sulfur conversion kinetics compared to FeN_4. The partial DOS patterns of Fe 3d orbitals in Figure 16g show that the Fe in the FeN_2 configuration reveals a higher d-band center (ε_d) than that in FeN_4. The higher ε_d resulted in an increased antibonding orbital energy, thus enhancing the polysulfide affinity and catalytic conversion kinetics. Moreover, the enhanced polysulfide immobilization of FeN_2 was investigated via the partial DOS of the S p-orbital in Li_2S_6, Li_2S_6—FeN_4, and Li_2S_6—FeN_2 (Figure 16h). The S p-DOS patterns of Li_2S_6—FeN_4 and Li_2S_6—FeN_2 became continuous with considerable distributions around the Fermi

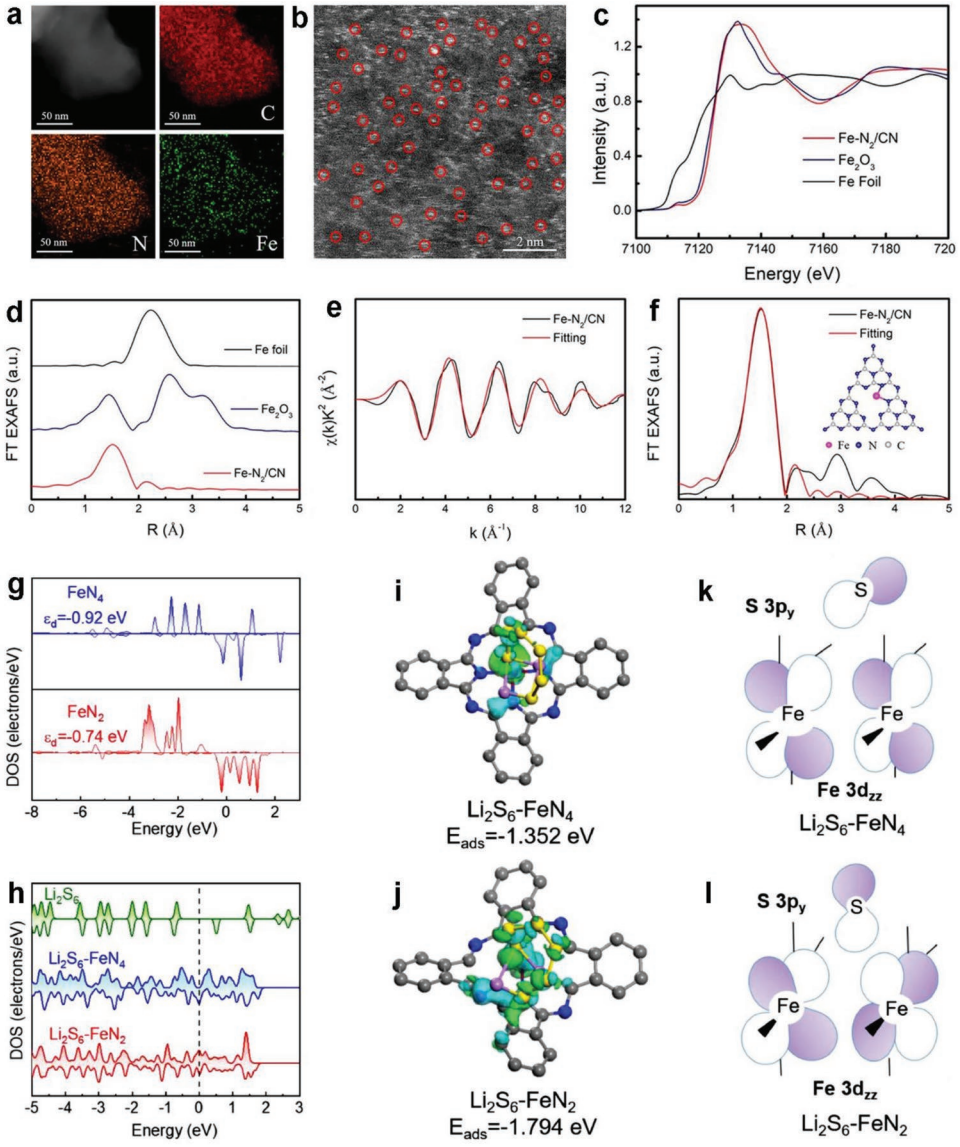

Figure 16. a) Element mapping and b) HAADF-STEM images of Fe—N_2/CN nanosheets, Fe atoms highlighted with red circles. c) Fe K-edge XANES spectra and d) Fourier transforms of Fe K-edge EXAFS spectra of Fe—N_2/CN, Fe foil, and Fe_2O_3. e) Fe *k*-space EXAFS fitting curve and f) *R* space EXAFS fitting curve of Fe—N_2/CN (inset is the top view of the optimized stable Fe—N_2 coordinated structure). Reproduced with permission.[213] Copyright 2020, American Chemical Society. g) Fe 3d DOS profiles of FeN_4 and FeN_2. h) S 2p DOS profiles of Li_2S_6, Li_2S_6—FeN_4, and Li_2S_6—FeN_2. Optimized configuration of i) Li_2S_6—FeN_4 and j) Li_2S_6—FeN_2. Interaction orbital diagram of k) Li_2S_6—FeN_4 and l) Li_2S_6—FeN_2. Reproduced with permission.[214] Copyright 2022, Elsevier.

level after adsorption, implying hybridization with the metal d-orbitals. Based on the stable adsorption configurations of Li_2S_6—FeN_4 and Li_2S_6—FeN_2 (Figure 16i,j), the Li_2S_6—FeN_2 interaction resulted in a much more intensive charge transfer with increased binding energy. Such binding behavior was also revealed from the interaction diagram of Wannier orbitals in Figure 16k,l. The Li_2S_6—FeN_2 couple formed more bonding orbitals, implying a stronger orbital hybridization. The experimental results confirmed the theoretical calculations by designing undercoordinated single-atom Fe catalysts on N-doped carbon (FeN_2—NC). The S—FeN_2—NC cathodes with a high sulfur loading of 5.0 mg cm^{-2} achieved a reversible areal capacity of 4.5 mAh cm^{-2} under a low E/S ratio of 5.3 mL g^{-1}.

3.4.2. Single-Atom Co

Like single-atom Fe, single-atom Co has also been introduced in Li–S batteries for the enhanced electrochemical conversion kinetics, either as host or interlayers.[215–217] The initial exploration of single-atom Co catalysts for enhanced sulfur redox kinetics was performed by Du et al.[204] Monodispersed Co atoms embedded in a N-doped graphene framework (Co—N/G) were prepared by using a heating treatment. Combining XAS with DFT calculations, the authors revealed that the bifunctional Co—N—C coordination centers were responsible for the facilitated conversion between sulfur and Li_2S in the (dis) charge process. The resulting S@Co—N/G cathodes delivered

an initial capacity of 1210 mAh g^{-1} at 0.2 C. Moreover, Huang et al. devised a fibrous carbon skeleton implanted with dispersed single-atom Co—N_x species (Co-PCNF) to regulate sulfur cathodes and lithium anodes simultaneously.[218] Due to the integration of the Co—N_x sites, the lithiophobic fibrous carbon skeleton became lithiophilic, mitigating the dendrite formation of lithium anodes. Simultaneously, the Co—N_x sites enabled the expedited conversion kinetics of the Li–S electrochemistry, effectively inhibiting the polysulfide shuttle. Benefiting from the synergistic effects between single-atom Co—N_x species and the 3D conductive carbon network, Li–S full batteries with a sulfur loading of 6.9 mg cm^{-2} achieved a reversible areal capacity of above 7.0 mAh cm^{-2}.

The coordination number of single-atom Co is key to catalytic activities. The Co—N_4 moiety is a common and stable structure, exhibiting enhanced catalytic conversion for sulfur cathodes.[219] For example, Li et al. reported single-atom Co supported on porous N-doped carbon matrix (Co-SAs@NC) derived from binary ZIF precursors.[215] The binary Co—Zn ZIF precursors successfully prevented the aggregation of Co nanoparticles, resulting in the formation of single-atom Co. The experimental results and theoretical calculations demonstrated that the unique Co—N_4 moiety in Co-SAs@NC acted as active sites to trap polysulfides and catalyze their electrochemical conversion. S@Co-SAs@NC cathodes with a 2.0 mg cm^{-2} sulfur loading delivered a stable capacity of 737 mAh g^{-1} after 600 cycles at 1.0 C.

To maximize the catalytic activities, increasing the content of the loading single-atom catalysts and the exposure of active sites would be successful strategies. In this case, monodispersed single-atom Co embedded in N-doped carbon nanosheets (CoSA—N—C) has been synthesized through a salt-template method, by which a high content of Co up to 15.3 wt% was achieved.[220] The densely populated Co—N_4 moiety functioned as catalytic sites, propelling the redox kinetics of polysulfides and mediating the Li_2S deposition. Sulfur cathodes with CoSA—N—C host exhibited a high capacity of 1574 mAh g^{-1} at 0.05 C and a low fading rate of 0.035% per cycle for 1000 cycles at 1.0 C. Moreover, Wang et al. designed a 3D carbon architecture by cross-linking 2D porous carbon leaves with atomically dispersed Co—N_4 moieties (Co—N_4@2D/3D carbon).[221] Such a hierarchical structure endowed rich interfaces with full exposure of Co—N_4 active sites to improve the adsorption and conversion of sulfur species. Another single-atom Co dispersed at hollow carbon spheres (ACo@HCS) has been reported as efficient polysulfide electrocatalyst due to the presence of abundant Co—N_4 active sites.[206] As shown in **Figure 17**a, SiO_2 nanospheres were chosen as a hard template. Then, the polymerization and controlled pyrolysis process resulted in the formation of ACo@HCS. The prepared nanospheres exhibited a distinct hollow structure without any cracks (Figure 17b–d). When working as sulfur host, ACo@HCS allowed sulfur cathodes to reach a high capacity of 1003 mAh g^{-1} after 500 cycles at 1.0 C.

The precise control of the Co—N coordination number is challenging but key to modulating the catalytic activities of single atoms. Therefore, Fang et al. investigated the relationship between the Co—N coordination environment and the polysulfide redox kinetics.[205] The authors proposed an exfoliation–evaporation strategy to prepare single-atom Co catalysts with different N coordination numbers. As illustrated in Figure 17e, layered Zn, Co—ZIF-L mixed with LiCl and KCl was annealed under Ar protection, leading to the intercalation of Li^+ and K^+ into the interlayers of Zn and Co—ZIF-L, and layer exfoliation. The organic links were subsequently pyrolyzed into NG, and Co and Zn were reduced. The removal of Zn nanoclusters by evaporation created abundant defects in NG and converted Co—N_4 into Co—N_2. DFT calculations concluded that the decreased coordination number of single-atom Co induced the asymmetrical charge distribution and upshifted the d-band center. Such effects benefited the chemical interaction between Co—N_2 and polysulfides, resulting in more efficient redox kinetics of sulfur species. The enhanced sulfur utilization has been validated by experimental results. Li–S batteries with Co—N_2-modified separators exhibited a higher capacity of 1004 mAh g^{-1} than Co—N_4 (951 mAh g^{-1}) at 0.3 C.

3.4.3. Other Single Atoms

In addition to single-atom Fe and Co, other single-atom catalysts have been employed in Li–S batteries, such as Ni,[222,223] Zn,[224–226] Mo,[227] V,[228] W,[229] and Ru.[230] Single-atom Ni has similar physicochemical characteristics when coordinated with N-doped carbon.[231] For example, Zhang et al. prepared single-atom Ni at N-doped graphene (Ni@NG) with Ni—N_4 structure.[222] The oxidized Ni sites in the Ni—N_4 structure reversibly catalyzed the conversion of polysulfides by forming S_x^{2-}—Ni—N bonds. Li–S batteries with Ni@NG modified separators exhibited a high capacity of 1598 mAh g^{-1} at 0.1 C. Furthermore, oversaturated Ni—N_5 moieties have been reported to be an optimal candidate for catalyzing the polysulfide conversion due to the asymmetrical electronic distribution. Based on DFT calculations, Ni—N_5/C showed the smallest kinetic barriers for SRR and moderate adsorption strength for sulfur species. Guided by the theoretical predictions, Zhang et al. synthesized the Ni—N_5 moiety incorporated in hollow N-doped porous carbon (Ni—N_5/HNPC) via a self-templating strategy.[223] When acting as sulfur host, Ni-N_5/HNPC allowed a superior battery rate performance at 4 C with an average specific capacity of 684 mAh g^{-1}.

The introduction of single-atom Zn to Li–S batteries was initiated by Shi et al.[224] The authors developed well-dispersed single-atom Zn-decorated hollow carbon spheres as dual-functional nanoreactors for suppressing the polysulfide shuttle and lithium dendrite formation. The designed Li–S full cell with a high S areal loading of 7.8 mg cm^{-2} delivered a high areal capacity of 8.7 mAh cm^{-2} under a low E/S of 6.4 µL mg^{-1}. Similarly, Song et al. fabricated a Janus separator with double-sided coating materials to regulate the lithium dendrite growth and the shuttle effect of polysulfides.[225] The coating of Bio-MOF-100 with an anionic framework allowed the rapid and uniform deposition of lithium at the anode. At the same time, its derived single-atom Zn catalysts accelerated the polysulfide conversion. Besides, Wang et al. implanted single-atom Zn and Co nanoparticles into N-doped-porous-carbon-nanosheet-grafted CNTs as integrated catalyst for SRR.[226] The strong interaction between Co nanoparticles and Zn—N_4 moieties resulted in optimal charge redistribution. Theoretical and experimental results have indicated that the synergistically active sites of Co

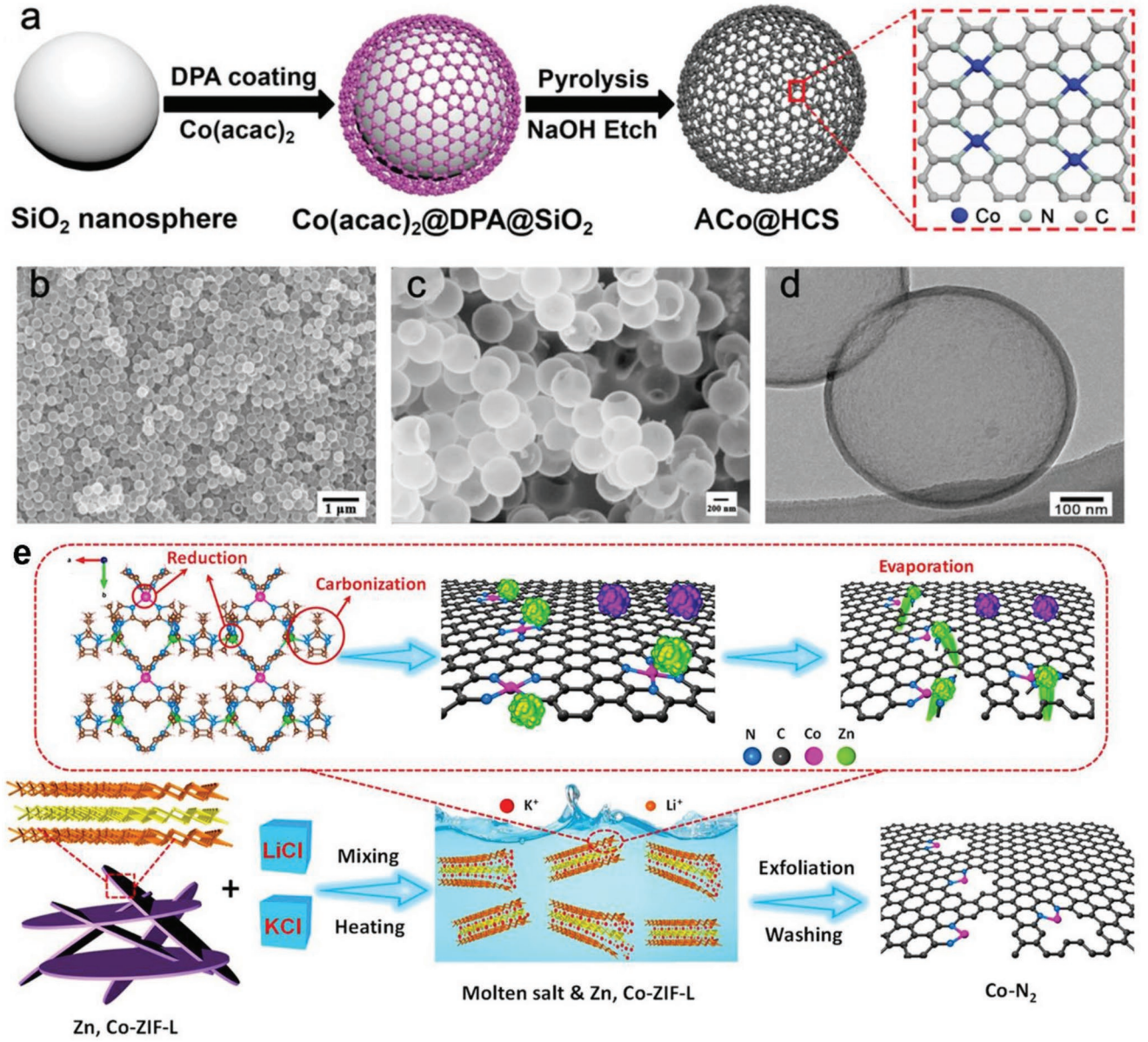

Figure 17. a) Schematic illustration of the fabrication of ACo@HCS host materials. b,c) SEM images of ACo@HCS. d) High-magnification TEM image of ACo@HCS. Reproduced with permission.[206] Copyright 2022, Wiley-VCH. e) Schematic illustration of Co—N_2 composite synthesis. Reproduced with permission.[205] Copyright 2022, American Chemical Society.

and Zn—N_4 strongly confined polysulfides and catalyzed the reduction reaction from Li_2S_2 to Li_2S by reducing the energy barriers. The supported carbon framework with a large surface area allowed adequate exposure of active sites and fast electron/ion pathways. Due to these synergistic effects, the developed catalyst provided Li–S batteries with a high capacity of 1302 mAh g^{-1} at 0.2 C.

Single-atom Mo with Mo—N_2/C sites has been developed to increase the polysulfide adsorption and conversion in Li–S batteries.[227] The Mo—N_2/C sites lowered the activation energy for both the reduction of Li_2S_4 to Li_2S and decomposition of Li_2S, offering Li–S batteries a high reversible capacity of 744 mAh g^{-1} at 5 C. Guided by DFT calculations, Zhou et al. screened single-atom V, which facilitated both the formation and decomposition of Li_2S during the (dis)charging process.[228] Similar conclusions were obtained by Andritsos et al. using DFT calculations.[232] By exploring the conversion mechanism from Li_2S_2 to Li_2S and Gibbs free energy for the reaction pathways from S_8 to Li_2S, the authors found that single-atom V lowered the dissociation barriers of the Li_2S_2 decomposition, leading to the improved reaction kinetics. Based on electronic structure calculations, Han et al. found that the d–p orbital hybridization between single-atom catalysts and sulfur species could act as a descriptor to guide the design of single-atom catalysts for Li–S batteries.[233] Transition metals with low atomic numbers (e.g., Ti) showed fewer filled antibonding states and more effective

Table 5. Summary of characterization techniques for SRR investigations.

Characterization	Applications	Refs.
CV	Study the electron transfer process; determine the Li-ion diffusion coefficient; evaluate the catalytic activities of materials (symmetric CV)	[15, 95, 102, 234]
LSV	Determine the onset potential, reaction overpotential, Tafel plots, and exchange current density	[16, 181]
Li_2S deposition	Study the mechanisms and kinetics of the reduction of polysulfides to Li_2S	[48, 239, 240]
EIS	Determine the charge transfer resistance, lithium-ion diffusion coefficient, and reaction activation energy	[16, 241–243]
In situ XRD	Probe the structural evolution and phase transformation of crystalline sulfur and Li_2S	[240, 246, 255]
In situ Raman	Probe the structural evolution of soluble polysulfide intermediates	[94, 119, 260]
In situ XAS	Identify sulfur species and the content; determine the oxidation states and coordination environment of sulfur species	[204, 263]
HPLC	Identify sulfur and polysulfides quantitatively and qualitatively in the electrolyte	[270, 272, 273]
Binding energy	Study the anchoring effects of catalyst materials toward sulfur species	[215, 282]
Gibbs free energy	Study the specific conversion mechanisms and reaction pathways	[119, 216]

d–p orbital hybridization, increasing the binding to sulfur species and decreasing the energy barriers of sulfur redox reactions.

4. Characterization Techniques and Methods

Various characterization techniques and methods have been developed to investigate the mechanisms and kinetics of SRR. These approaches can be divided into three categories: electrochemical measurements, spectroscopic techniques, and theoretical calculations. **Table 5** summarizes the characterization techniques applied to SRR investigations.

4.1. Electrochemical Measurements

4.1.1. Voltammetry

Voltammetry is one of the most common electrochemical methods used in catalysis and energy research. Two types of voltammetries have been implied in Li–S batteries for investigating the redox and charge transfer processes, e.g., CV and LSV. In Li–S batteries, CV is typically performed in two-electrode cells to get information about reaction mechanisms and kinetics of sulfur cathodes. **Figure 18**a shows a typical CV curve of Li–S batteries. Two reduction peaks are generally found during the lithiation process. Peak A at about 2.35 V is attributed to the reduction of elemental sulfur to soluble polysulfides. Peak B at about 2.0 V represents the further reduction of polysulfides to insoluble Li_2S. The two-step reduction process corresponds to the two discharge plateaus shown in Figure 2. Two oxidation peaks (C and D) during delithiation reveal the reverse reactions. By analyzing the change in the peak potential and current, the reaction kinetics of sulfur cathodes can be determined. In this case, Tian et al. evaluated the catalytic properties of CNT@MoS_2—B for polysulfide conversion by CV.[102] The S/CNT@MoS_2—B cathode showed higher reduction potentials and lower oxidation potential than S/CNT@MoS_2. Furthermore, S/CNT@MoS_2—B revealed a stronger current response for the redox reactions. The CV analyses indicated that the incorporated B significantly improved the redox kinetics of sulfur cathodes.

During the (dis)charging process of Li–S batteries, lithium ions migrate between two electrodes under the electric field and concentration gradient. Due to the sluggish redox kinetics of Li–S batteries, the lithium-ion diffusion in sulfur cathodes is the rate-determining step. Therefore, investigating the lithium-ion diffusion in sulfur cathodes helps understand the reaction kinetics of Li–S batteries. High diffusion coefficients of lithium ions mean high-rate capability for Li–S batteries, which can be estimated by CV. By plotting the CV curves with different scan rates, the relationship between the CV peak currents and the scan rates can be described by the Randles–Sevcik equation, in which the lithium-ion diffusion coefficient can be determined. According to the Randles–Sevcik equation

$$I_p = 269000 n^{3/2} A C D^{1/2} v^{1/2} \quad (8)$$

where I_p is the peak current (A), n is the stoichiometric number of electrons involved in an electrode reaction, A is the surface area of the working electrode (cm^2), C is the molar concentration (mol cm^{-3}) of reacted lithium ions (the amount of reacted lithium ions in moles can be calculated from the integral of the CV curve), D is the lithium-ion diffusion coefficient (cm^2 s^{-1}), and v is the electrode potential scan rate (V s^{-1}). The lithium-ion diffusion coefficient can be calculated by changing the scan rates of the CV. Since n, A, and C can be considered constant in the experiments, plotting I_p versus $v^{1/2}$ yields the lithium-ion diffusion coefficient of the sulfur cathodes from the slope of the I_p–$v^{1/2}$ curves. Such a method has been employed to compare the catalytic effects of different materials on sulfur conversion kinetics.[54,77,95] Note that the lithium-ion diffusion in Li–S batteries is a complex process, which involves phase transitions, interfacial migration, and Li_2S formation and decomposition. Besides, the real surface area of the working electrode is significantly higher than the geometric area. The lithium-ion diffusion coefficient determined by the Randles–Sevcik equation is therefore the apparent diffusion coefficient.

Symmetric cell measurements using CV have been designed to evaluate the catalytic activities of materials for the sulfur redox kinetics.[15] The configuration of symmetric cells typically contains two identical electrodes, which are fabricated by pure catalyst materials without loading sulfur species. Polysulfides (e.g., Li_2S_6), soluble in the electrolyte, function as active materials to

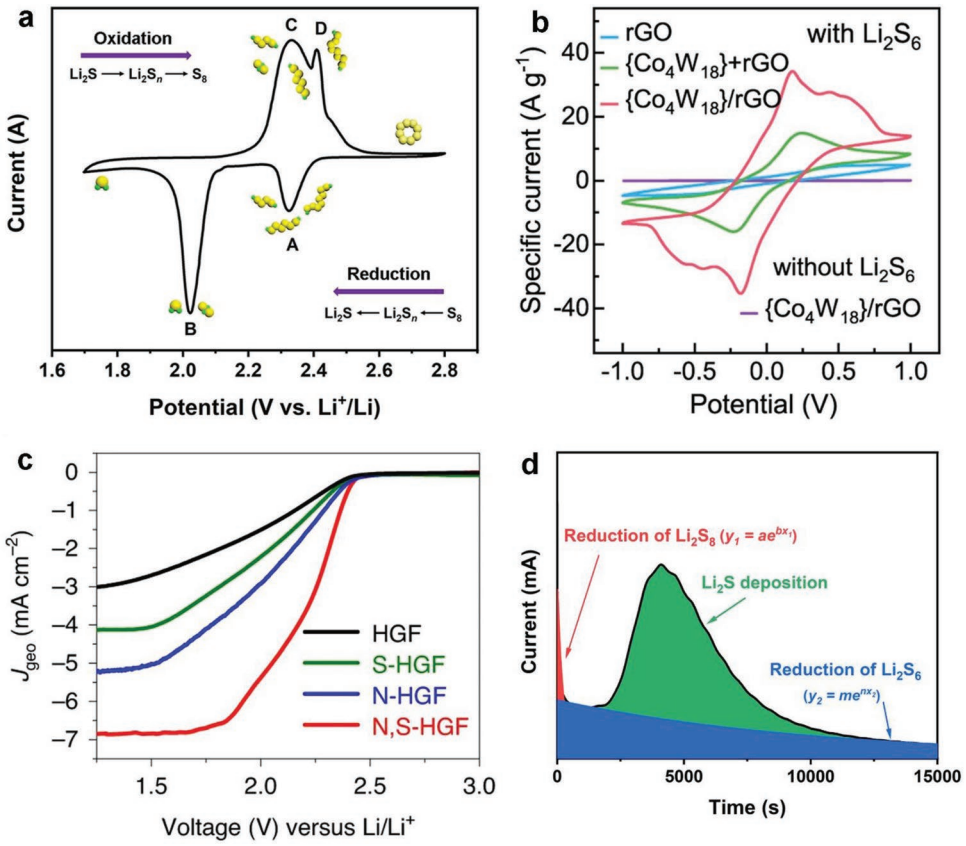

Figure 18. a) Typical cyclic voltammogram for Li–S batteries. b) CV curves of Li_2S_6 symmetric cells with the rGO, Co_4W_{18} + rGO, and Co_4W_{18}/rGO electrodes. Reproduced under the terms of the CC-BY license.[234] Copyright 2022, The Authors, Published by Springer Nature. c) LSV curves of heteroatom-doped HGFs toward sulfur reduction. Reproduced with permission.[16] Copyright 2020, Springer Nature. d) Fitting current transient curves for potentiostatic Li_2S deposition.

facilitate the redox conversion reactions. The catalytic activities are reflected by the current response in the CV curves. If catalyst materials promote the redox reaction of polysulfides, the CV indicates an increased current response. Based on the symmetric cell analyses, Lei et al. explored the conversion kinetics of polysulfides by a single-dispersed molecular cluster catalyst (Co_4W_{18}/rGO) comprised of a polyoxometalate framework embedded in reduced graphene oxide.[234] As shown in Figure 18b, the symmetric cell with Co_4W_{18}/rGO exhibited the highest current response among all CV curves, implying the more rapid conversion kinetics of sulfur species at the electrode/electrolyte interface.

LSV involves a linear scan of either a reducing or oxidizing voltage. It has been widely used in oxygen reduction reaction (ORR) and oxygen evolution reaction to investigate the performance of catalysts.[235,236] LSV is normally performed on a rotating disk electrode with a three-electrode system, which eliminates the polarization effects of the counter electrode. LSV requires a low voltage sweeping speed to keep a steady state on the electrode surface compared with CV. Therefore, some critical parameters can be obtained, such as the onset potential, reaction overpotential, Tafel plots, and exchange current density, indicating the thermodynamic and kinetic properties. The mechanisms and kinetics of Li–S batteries investigated by LSV have been reported by Peng et al.[16] Figure 18c shows SRR polarization curves with different heteroatom-doped HGF catalysts. N, S-HGF exhibited the highest half-wave potential, implying the smallest overpotential for SRR. N, S-HGF catalysts exhibited the smallest Tafel slope, indicating the optimal catalytic performance and accelerated reaction kinetics for SRR (see Figure 5b). According to the Tafel equation

$$\eta = a + b\log(j) \tag{9}$$

where η is the overpotential, a is the constant, b is the Tafel slope, and j is the measured current density. The exchange current density can be obtained by fitting and extrapolating the η versus log(j) plot to zero overpotential. Note that the y-axis of Tafel plots represents the overpotential, i.e., the potential difference between equilibrium potential (E_0) and measured potential (E). It is more convenient to calculate the Tafel slope based on the E instead of η as the function of log(j). However, the exchange current density should be calculated based on η versus log(j) plot (not simply extrapolate E versus log(j) plots to zero potential), since the exchange current density is defined as the current flowing equally in both directions when an electrode reaction is in equilibrium, i.e., at the equilibrium potential when $\eta = 0$. The (quasi)equilibrium potential can be evaluated via galvanostatic intermittent titration technique or potentiostatic intermittent titration technique.[48,237,238]

Due to the close Gibbs free energies of polysulfides, various polysulfide ions coexist over a wide range of states-of-charge. This phenomenon results in difficult separation of the specific electrochemical reaction process. Currently, two typical reaction processes in Li–S batteries are investigated to estimate the Tafel plots, i.e., the solid–liquid reduction from sulfur to polysulfides and liquid–solid Li_2S deposition. The calculated Tafel slope and exchange current are reasonable to indicate the SRR kinetics. Regarding the liquid–liquid reactions with various polysulfides, more advanced characterization and measurement approaches should be developed to separate the electrochemical processes. Therefore, the related electrochemical parameters are possible to be well estimated.

4.1.2. Li_2S Deposition

The potentiostatic Li_2S deposition experiment was developed by Fan et al.[48] Nowadays, it is a traditional approach to investigating the mechanisms and kinetics of the Li_2S deposition. Section 2.3 discussed the factors that affected the nucleation and growth of Li_2S particles. Here, we will formulate how the Li_2S deposition experiment works. The Li_2S deposition is typically carried out in a Li_2S_8 electrolyte as the active species. Tetraglyme is selected as the solvent instead of the traditional mixture of DOL and DME since it is beneficial to the Li_2S deposition.[239] Catalyst materials are loaded on carbon fiber paper as the cathode. The assembled cell is initially galvanostatically discharged to 2.06 V at a small current to consume the long-chain polysulfides. Subsequently, the Li_2S nucleation and growth are carried out potentiostatically at 2.05 V. As illustrated in Figure 18d, the monotonically decreased current can be fitted by two exponential functions, indicating the reduction of Li_2S_8 and Li_2S_6, respectively. The isolated peak therefore is related to the Li_2S deposition. The capacity of the Li_2S deposition can be calculated based on current integration by subtracting the reduction of Li_2S_8 and Li_2S_6. According to this test, Wang et al. demonstrated that NbB_2 nanoparticles significantly facilitated the Li_2S nucleation with a high capacity of Li_2S deposition, catalyzing the liquid–solid reaction of Li–S batteries.[240]

4.1.3. Electrochemical Impedance Spectroscopy

EIS is a powerful technique to analyze specific electrochemical processes, as different electrochemical processes correspond to different response frequencies in EIS.[241] Therefore, EIS applied in Li–S batteries can offer various information about electrodes, such as charge transfer, lithium-ion diffusion, and reaction activation energy. Zhao et al. designed a semi-immobilized molecular catalyst with porphyrin active sites to promote the redox reaction of Li–S batteries.[242] EIS analyses revealed that this catalyst displayed the smallest charge transfer resistance (R_{ct}) compared with its counterparts. Such results were consistent with the LSV measurements, from which porphyrin active sites led to the lowest Tafel slope, implying the enhanced kinetics for SRR. By fitting the Warburg slope of EIS curves, Wang et al. calculated the lithium-ion diffusion coefficient for Li–S batteries with red-phosphorus-nanoparticle-modified separators.[243] The EIS analyses indicated improved lithium-ion diffusion by the addition of red phosphorus nanoparticles, enabling rapid sulfur redox kinetics and high sulfur utilization. In addition, the investigation of the temperature dependence of R_{ct} can give information about the activation energy for SRR. The temperature dependence has been expressed by the Arrhenius equation

$$\ln\left(R_{ct}^{-1}\right) = \frac{-E_a}{RT} + C \tag{10}$$

where E_a (J mol^{-1}) indicates the activation energy, R (8.314 J mol^{-1} K^{-1}) is the universal gas constant, T (K) denotes the absolute temperature, and C is the constant. By fitting $\ln(R_{ct}^{-1})$ as a function of T^{-1}, E_a can be calculated from the slope of the linear dependences. Based on the fitting results, Peng et al. verified that reduction from sulfur to Li_2S underwent gradually sluggish kinetics since the activation energy became increasingly large during SRR (Figure 5a).[16] Our work also reached the same conclusion, from which the Li_2S deposition needed to overcome the highest energy barrier.[77]

4.2. Spectroscopic Techniques

A wide range of spectroscopic techniques has been applied to Li–S batteries to probe the electrode structures and get information about the active sites of catalysts.[244] Due to the complexity of the Li–S electrochemistry and the sensitivity of sulfur species to the air, regular ex situ spectroscopic approaches are difficult to reveal the underlying reaction mechanisms effectively. Therefore, in situ or in operando spectroscopic techniques, which can monitor the battery reaction process in real time, offer detailed insights into the electrode processes and catalyst materials.

4.2.1. In Situ X-Ray Diffraction

In situ X-ray diffraction (XRD) can probe the structural evolution and phase transformation of sulfur species and catalyst materials during battery operation.[153,178,196,245] Nelson et al. initially employed in operando XRD to study structural and morphological changes during the electrochemical charge transfer reactions in Li–S batteries.[246] The authors found that the recrystallization of sulfur was strongly dependent on the cathode preparation technique. No crystalline Li_2S was detected at the end of discharging for the studied cathodes, which was opposite to the published ex situ XRD results.[247,248] The distinctly different findings from previously published reports stress the significance of in operando XRD techniques in the Li–S electrochemistry.

In principle, polysulfides are not detectable by XRD due to the solubility in the electrolyte. However, using in operando XRD, Conder et al. directly observed the evolution of polysulfides in Li–S batteries during operation.[245] They developed reliable approaches to make polysulfides visible by the organized adsorption of long-chain polysulfides at the SiO_2 surface of glass-fiber separators. SiO_2 (fumed silica) was directly used

as an electrolyte additive in Li–S batteries. The formation and evolution of two polysulfide peaks were readily observed in the electrolyte with SiO_2 by in operando XRD. These peaks emerged and showed significant intensities at the end of the upper-voltage plateau, in which the long-chain polysulfides were produced. The interactions between SiO_2 and polysulfides resulted in the specific adsorption of only long-chain polysulfides, forming an organized layer at the surface of glass fibers. Therefore, the broad peaks were generated in the diffractograms. By contrast, no peaks were detected without SiO_2 additives in conventional polyolefin separators. These results have also been demonstrated by SEM, TEM, and XPS analyses for a deep understanding of polysulfide adsorption. The authors then used fumed silica as an electrolyte additive in coin-type cells to examine the practical significance of the long-chain polysulfide adsorption on SiO_2. The results revealed that the presence of SiO_2 in the electrolyte achieved an increase at least 25% in the battery capacity compared to the reference cell with standard electrolytes. The adsorption of polysulfides at the surface of SiO_2 improved the cycling performance and mitigated the aging of the Li–S batteries by scavenging the PS species. In operando XRD worked well in probing the polysulfide adsorbents/scavengers and identifying the roles in the reaction mechanisms.

Figure 19a illustrates an example of in situ XRD equipment. To perform in situ XRD measurements, a mold cell with a sealed window on the cathode side was designed to allow the incident X-ray to transmit the Al foil in cathodes. The cell configuration needed a high sulfur loading, enabling it to measure high diffraction intensities. With such in situ XRD equipment, Wang et al. analyzed the catalytic effects of NbB_2 nanoparticles on the polysulfide conversion and L_2S nucleation.[240] Figure 19b shows a contour map of in situ XRD measurements. The diffraction peaks at 23.06°, 25.8°, 26.7°, and 27.7° were indexed to be the crystalline α-S_8 (JCPDS No. 78-1889). The diffraction peaks of α-S_8 gradually decreased and finally disappeared at 2.1 V during discharging, implying the solid–liquid conversion from sulfur to soluble Li_2S_4. The characteristic peak of Li_2S at 27° (JCPDS No. 77-2145) was detected during further discharging and reached a maximum intensity at 1.7 V, indicating full liquid–solid conversion. In the following charging process, the peak of Li_2S decreased gradually and a series of new diffraction peaks corresponding to β-S_8 appeared. The in situ XRD results demonstrated that NbB_2 nanoparticles significantly accelerated the conversion from sulfur to Li_2S and improved the reversible performance of Li–S batteries.

Luo et al. in situ assembled VS_4 mediators uniformly anchored in a reduced graphene oxide scaffold (VS_4@rGO) to regulate the polysulfide conversion kinetics.[249] Based on the in situ XRD analyses, the authors directly monitored the polysulfide evolution and probed the role of VS_4 in the overall electrochemical reaction process. As shown in Figure 19c, α-S_8 was initially detected in the contour plot. With discharging proceeding, the signal intensities of sulfur continuously decreased until the end of the upper-discharge plateau. Meanwhile, broad peaks at 25°–26° emerged, associated with the long-chain polysulfides from the sulfur reduction. The observation of polysulfides by in situ XRD was well explained by the polysulfide adsorption at the surface of the electrode and separator.[206,245,250] Subsequently, the diffraction peaks upshifted with reduced intensities, suggesting the formation of short-chain polysulfides. At the beginning of the lower-discharge

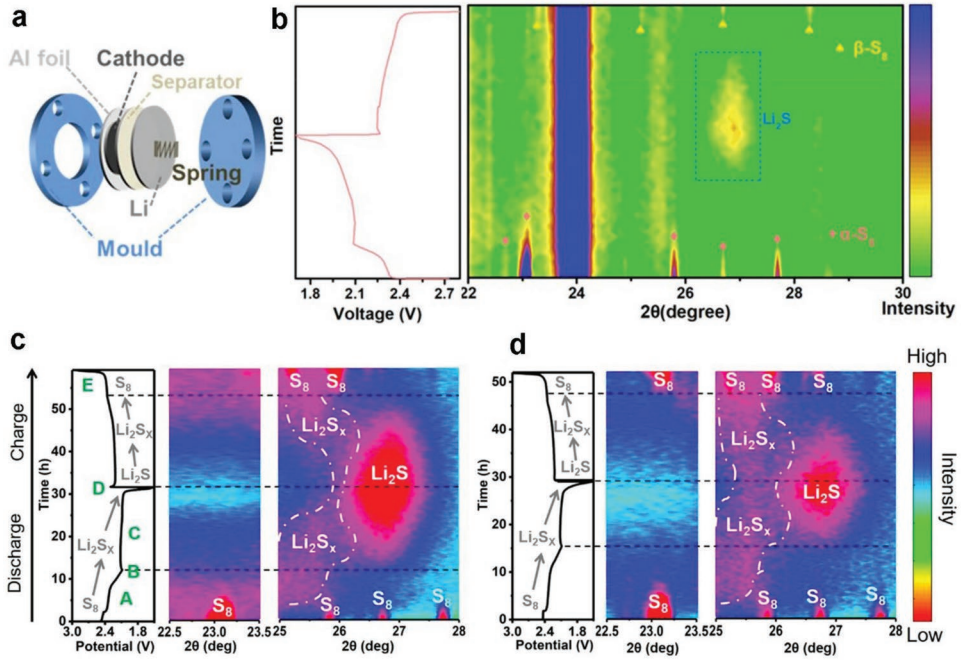

Figure 19. a) Schematic illustration of a cell configuration for in situ XRD measurements. b) In situ XRD contour plots with the corresponding voltage profile curves. Reproduced with permission.[240] Copyright 2022, American Chemical Society. In situ XRD patterns in contour plots of the Li–S cells c) with and d) without VS_4 as a function of discharge/charge during the first cycle. Reproduced with permission.[249] Copyright 2020, American Chemical Society.

plateau, crystalline Li_2S was formed, which indicated the occurrence of liquid–solid phase transitions. By contrast, cells without VS_4 showed much stronger polysulfide signals from in situ XRD (Figure 19d). These results demonstrated that VS_4 possessed effective chemical anchoring and catalytic effects toward polysulfides, greatly alleviating the shuttle effect and accelerating the polysulfide conversion kinetics. The in situ XRD analyses therefore unraveled the phase evolution of sulfur species and confirmed the improved sulfur utilization by VS_4.

Other research on the conversion mechanisms of sulfur species by in situ XRD has been reported.[251,252] For instance, using WS_2 nanopetals as the catalytic center for polysulfide redox reactions, Huang et al. validated that Li_2S began forming at the early stage of discharging, while the β-S_8 nucleation occurred before the upper-voltage plateau during charging, which was distinct from the conventional Li–S electrochemistry.[253] Peng et al. investigated the reaction mechanisms of Li–S batteries under a wide temperature range by in situ XRD.[254] At a higher temperature up to 40 °C, the diffraction intensities of Li_2S enhanced significantly, revealing the accelerated phase transition process and improved sulfur utilization. However, no typical Li_2S signals were detected from in situ XRD at 0 °C, which probably resulted from the little amount of Li_2S formation. Li et al. conducted in situ XRD analyses to confirm the formation of Li_2S_2 at 2.3 V during discharging.[255] The developed TiO_xN_y—TiO_2 quantum dots@carbon sulfur host materials facilitated the conversion from Li_2S_2 to Li_2S. By contrast, the pristine carbon host simply converted sulfur into L_2S_2 at the end of discharging. Since the conversion kinetics of Li_2S is more sluggish without an effective catalyst, the Li_2S diffraction peak will not appear in the in situ XRD spectra. The same phenomenon was also found by Ye et al. They did not detect the Li_2S peak for acetylene black/sulfur composite cathodes during the whole discharging and charging processes.[112] Suitable catalyst materials should facilitate the complete conversion from sulfur to Li_2S, thus mitigating the shuttle effect of polysulfides.[197,256]

4.2.2. In Situ Raman

Since XRD can only detect crystalline sulfur and Li_2S_2/Li_2S, it is difficult to probe the soluble polysulfide intermediates. By contrast, in situ Raman is an excellent complementary technique to in situ XRD, as polysulfides exhibit high Raman responses.[257–259] Due to the overlapping Raman peaks of various polysulfides, in situ Raman is preferred to analyze these sulfur species qualitatively. The Raman shifts of polysulfides are generally below 500 cm^{-1}, but the measured peak positions may vary depending on the chemical environment of polysulfides in Li–S batteries.[260]

He et al. fabricated ReS_2 nanosheets with 1T′-phase grown on CNT (ReS_2@CNT) to catalyze the polysulfide redox reaction.[94] In situ Raman results suggested that strong peaks of polysulfides remained at the end of the discharging in the CNT/S cathode, indicating severe shuttle effects during discharging. However, the ReS_2@CNT/S cathode did not show Li_2S_6 and Li_2S_4 signals, implying high catalytic activities of ReS_2@CNT to the sulfur redox kinetics. Furthermore, He and co-workers employed in situ Raman to investigate the acceleration of a series of Mo-based compounds on the electrochemical conversion of Li–S batteries, including MoS_2,[100] Mo_2C,[119] and $MoTe_2$.[261] **Figure 20**a–d shows the evolution of various polysulfides detected by in situ Raman in two sulfur cathodes with pure CNT and MCN host materials, respectively.[119] The contour plot of the CNT/S cathodes during discharging (Figure 20a) identified distinct Raman signals, corresponding to various long-chain polysulfides (Figure 20c). The characteristic Raman shifts at about 149, 219, and 477 cm^{-1} resulted from the bending and stretching vibrations of S—S in S_8^{2-}. The disappearance of the S_8^{2-} signals during the later discharging revealed the S_8 ring opening occurring near the voltage plateaus of 2.36 V. When discharging continued, the signals of S_6^{2-} at 398 and 509 cm^{-1} gradually increased and reached at the maximum at about 2.1 V. Meanwhile, the S_4^{2-} singles were detected at 202 and 445 cm^{-1}. The coexistence of S_6^{2-} and S_4^{2-} indicated severe diffusion of polysulfides from the CNT/S cathode to the electrolyte during discharging. By contrast, the MCN/S cathodes simply showed weak Raman signals of S_8^{2-}, S_6^{2-}, and S_4^{2-} with decreased intensities throughout the whole discharging process (Figure 20b,d). The in situ Raman analyses confirmed that MCN effectively mitigated the polysulfide shuttle and accelerated the reaction kinetics of SRR.

Shao and co-workers employed in situ Raman to monitor the dynamic variation of sulfur species upon discharging and charging.[177,183] MC-NSs were developed to accelerate the polysulfide conversion.[177] The peaks of S_8 at 150, 219, and 474 cm^{-1} were observed at the open-circuit voltage. With the battery discharging to 2.1 V, the characteristic peaks of Li_2S_6, Li_2S_4, and Li_2S_2 replaced those of S_8. The Li_2S_2 peak dominated at the end of discharging, implying an effective conversion of polysulfides by MC-NS. The subsequent charging process also underwent a complete conversion from Li_2S_2 to the initial S_8. The in situ Raman results revealed that MC-NS enhanced the conversion kinetics of sulfur cathodes and alleviated the shuttle effects of polysulfides.

Shi et al. demonstrated that CoFe alloy catalysts enabled polysulfide conversion and redox kinetics via in operando Raman spectroscopy.[191] To evaluate the confinement of the MoS_2—MoO_3-modified separators on sulfur species, Lei et al. detected sulfur species on the unmodified side of the separator during battery cycling.[145] It was furthermore found by in situ Raman that the unmodified side showed fewer polysulfide signals, which almost disappeared at the end of discharging and charging, suggesting the effective inhibition of the polysulfide shuttle by MoS_2—MoO_3. Based on the in situ Raman analyses, Sun et al. demonstrated that CoP with P vacancies effectively adsorbed polysulfides and promoted their electrochemical conversions.[166] Little soluble polysulfides were detected from the electrolyte at the end of discharging for the batteries with CoP with P vacancies. Yao et al. used in situ Raman to investigate the inhibition effects of the designed separator modification layers on the polysulfide shuttle.[147,167]

4.2.3. In Situ X-Ray Absorption Spectroscopy

XAS is an advanced technique to investigate the electronic structures and chemical environment of electrode materials.

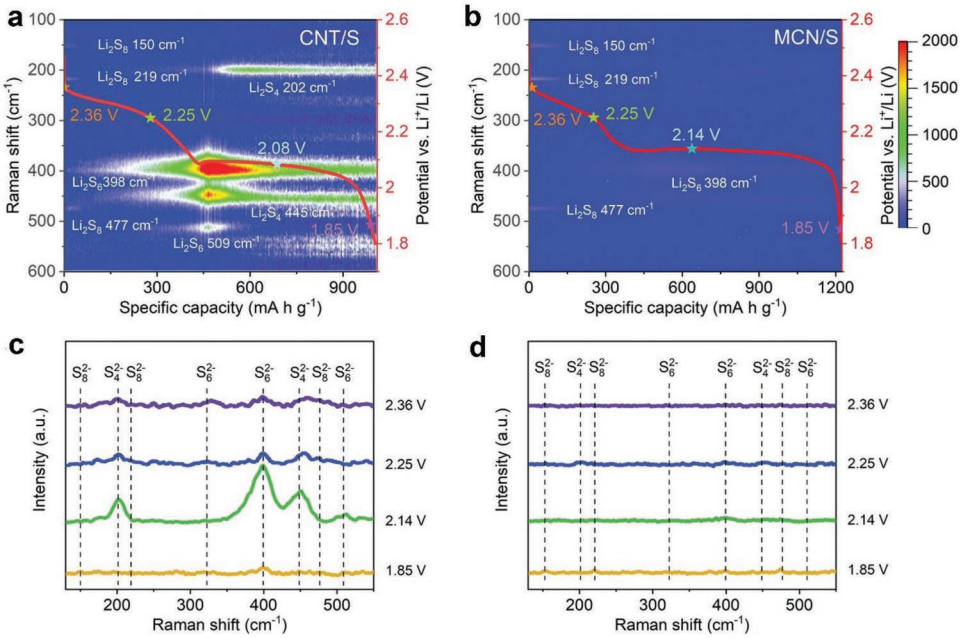

Figure 20. a,b) In situ time-resolved Raman images of the cathode with CNT/S and MCN/S, respectively. c,d) Selected Raman spectra of the CNT/S and MCN/S cathodes, respectively. The insetted red curves in (a) and (b) are voltage profiles of the CNT/S and MCN/S cathodes, respectively. Reproduced with permission.[119] Copyright 2021, Wiley-VCH.

XAS includes XANES and EXAFS, which provide complementary structural information. XANES determines the oxidation states and coordination environment of the absorbing atoms. EXAFS gives information about the interatomic distances and coordination numbers of the absorbing atoms. Therefore, the two methods can effectively probe various sulfur species.[262] The early research on sulfur species using in operando XAS was conducted by Nazar and co-workers.[263] By analyzing the S K-edge XANES, the authors verified that the discharge capacity was mainly restricted by the unreacted sulfur instead of the Li_2S deposit. Moreover, they accessed the formation of sulfur radicals during the cycling of Li–S batteries.[46] The XANES results revealed that radicals were not stable in glyme-based electrolytes. However, $S_3^{\bullet-}$ radicals generated from the dissociation of S_6^{2-} anions in donor solvents, like dimethylacetamide (DMA) and DMSO, were highly concentrated and nonreactive, which allowed full utilization of sulfur and Li_2S.

Since the presence and role of polysulfide radicals are critical to the Li–S electrochemistry, Wujcik et al. combined in situ XAS and first-principle calculations to characterize polysulfide radicals in an ether-based electrolyte.[264] The authors measured the X-ray spectra of chemically equilibrated Li–S batteries at various depths of discharge. The results demonstrated that significant quantities of polysulfide radical species (LiS_3, LiS_4, and LiS_5), as well as $S_3^{\bullet-}$ radical anions were present after initial discharging to the upper-discharge plateau, which was evidenced by a low energy shoulder in the S K-edge XAS below 2469 eV. By analyzing sulfur K-edge XAS, Dominko et al. compared and discussed the discharging mechanisms of sulfur conversion in three different electrolytes of Li–S batteries.[265] In the ether-based electrolytes, the sulfur conversion and formation of polysulfides occurred predominantly during the high-voltage plateau. In the fluorine-based electrolytes, the equilibrium between polysulfides and sulfur dominated the high-voltage plateau, which was similar with that in the ether-based electrolytes. However, reversible SRR in the carbonate-based electrolytes was only possible when sulfur was confined within the ultra-micropores. Zhao et al. employed time-resolved in operando XAS to explore the dynamic behavior of sulfur species at various current rates in Li–S batteries.[266] The results indicated that the whole process of SRR was significantly affected by the discharging rates, especially for the reduction of α-S_8 to long-chain polysulfides.

To reveal the sulfur redox chemistry at the surface of a single-atom Co-embedded N-doped graphene framework (Co—N/G), Du et al. carried out in operando XANES measurements on a Li–S battery upon discharging and charging.[204] The S K-edge spectra obtained at various SoCs were analyzed. An intense peak at 2470.9 eV was visible during cycling, which resulted from the S—S bond. The pre-edge peak at 2469.0 eV was assigned to the terminal sulfur of polysulfides. Besides, two broad peaks at 2471.9 and 2474.7 eV were observed, corresponding to Li_2S. During discharging, the signal intensity of polysulfides initially increased and then decreased, in which a maximum appeared at the beginning of the second voltage plateau at 2.1 V. Particularly, an apparent peak of Li_2S emerged at the beginning of discharging above 2.1 V, implying the early formation of Li_2S. This result differed from previous XANES studies, which confirmed that the formation of Li_2S occurred only at the end of the second voltage plateau. The early Li_2S formation at the initial discharging probed by in operando XANES demonstrated the high catalytic activity of Co—N/G, which significantly improved the conversion kinetics from soluble polysulfides to insoluble lithium sulfides.

By precisely monitoring sulfur species at the electrolyte–anode interface (AEI) and cathodic electrolyte–separator interface in a real-time condition, Jia et al. investigated the migration

of polysulfides across Li–S batteries via in situ XAS.[267] The authors employed a shuttle-suppressing strategy by introducing an electrocatalytic layer of hybrid bismuth sulfide/bismuth oxide nanoclusters in a carbon matrix (BSOC), which greatly improved the sulfur utilization and cycling stability of Li–S batteries. The dynamic polysulfide shuttle in Li–S batteries with and without the modification layers has been examined. **Figure 21**a presents the specifically designed in situ cell for in situ S K-edge XAS observations. Regarding the pristine cell, the 2D S-Kedge spectra (Figure 21c) were nearly constant during discharging, indicating the unchanged sulfur species at AEI during cell operation. This was also validated by the selected spectra under different potentials (Figure 21d), which showed the same profile trends. The characteristic Li_2S peaks at about 2473.2 and 2475.3 eV revealed the sulfur species shuttling from cathodes to anodes during discharging. Besides, SO_4^{2-} species was observed at about 2482.0 eV. The spectra indicated the abundant deposition of Li_2S and Li_2SO_4 species on lithium anodes, producing an insulating layer to block the charge transfer across AEI. These results indicated the irreversible corrosion of metallic lithium by Li_2S due to the shuttle effect. By contrast, Li–S batteries with BSOC layers showed considerably distinct sulfur species. A strong peak at 2480.0 eV was observed (Figure 21f,g), corresponding to the signal of sulfonyl groups in lithium bis(trifluoromethanesulfonyl)imide (LiTFSI) salts. Meanwhile, insoluble Li_2SO_3 species were also observed at about 2478.0 eV. The absence of Li_2S peaks suggested the effective suppression of the shuttle effect by introduced BSOC layers. Based on the in situ XAS analyses, the different AEI structures in two types of Li–S batteries validated an effective polysulfides anchoring by BSOC layers, resulting in enhanced cell performances.

Similarly, Zech et al. employed in operando near-edge X-ray absorption fine structure (NEXAFS) analyses to probe soluble polysulfides at both electrode sides in Li–S batteries.[268] Based on the S K-edge NEXAFS, the authors quantitatively investigated the formation of polysulfides. The results revealed that the polysulfide migration from the anode to the cathode was inhibited during charging, which caused a steady increase in polysulfides at the anode side. This phenomenon was considered as one of the key points for capacity decay. The present quantitative NEXAFS-based technique for in operando characterization of polysulfides did not require significant modifications of the

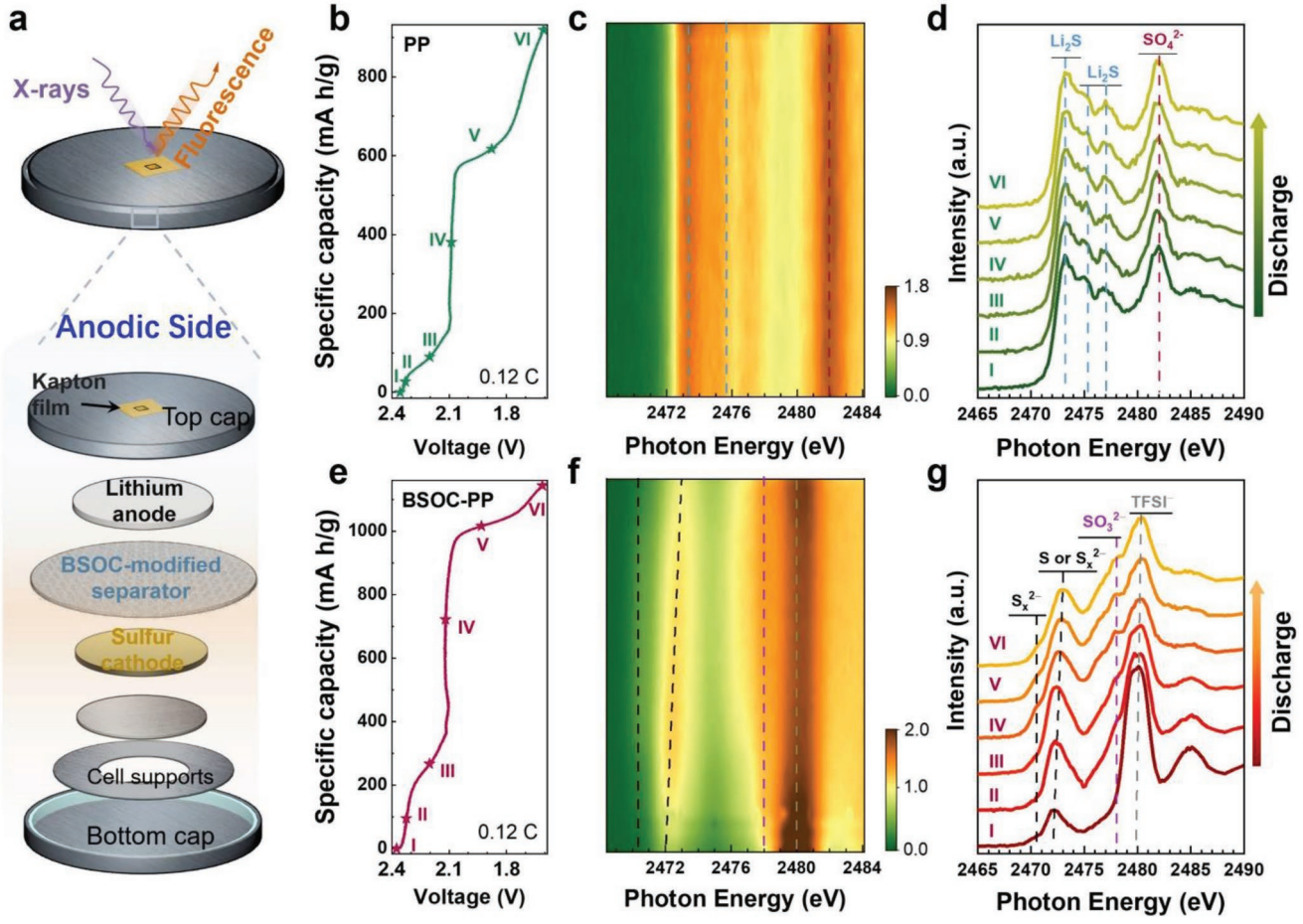

Figure 21. a) Schematic illustration of the coin cell design for AEI observation via in situ XAS studies. b) Initial discharge voltage profile of the pristine Li–S batteries using bare PP at 0.12 C for in situ XAS measurements. c) In situ S K-edge XAS map, and d) representative XAS spectra collected at indicated potentials from (b) with marked stars. e) Initial discharge voltage profile of BSOC-modified Li–S batteries at 0.12 C for in situ XAS measurements. f) In situ S K-edge XAS map, and g) representative XAS spectra collected at indicated potentials from (e) with marked stars. Reproduced with permission.[267] Copyright 2020, Wiley-VCH.

battery structures, which could be carried out in the coin-type cells. Besides, this in operando technique could also be applied to investigate the polysulfide retention by separator materials.

Ex situ XANES has also been used to reveal the redox reaction mechanism of sulfur cathodes.[147,167] Gao et al. employed S K-edge XANES to investigate the catalytic mechanisms of Co-doped SnS_2 (Co−SnS_2) for polysulfide conversion.[269] When sulfur cathodes were discharged from 2.0 to 1.7 V, the signal peak of the S−S bond at 2471.6 eV disappeared, which indicated that Co−SnS_2 promoted the complete conversion of polysulfides to Li_2S. Wang et al. demonstrated that VO_2(P) accelerated the Li_2S formation at 1.7 V.[72] The clear Li_2S peaks at 2471.6 and 2473.3 eV were observed from the S K-edge XANES.

4.2.4. High-Performance Liquid Chromatography

Since polysulfide species with various lengths are soluble in the electrolyte and air-sensitive, reliable approaches are still limited to analyze individual polysulfide intermediates qualitatively and quantitatively. HPLC is a powerful separation technique that is widely applied in qualification and quantitation coupled with MS. By introducing this method to Li–S batteries, researchers have successfully determined various polysulfides in the electrolyte.[270–272] Currently, HPLC has been the sole technique which can identify the concentrations of individual polysulfides with different chain lengths. To accurately analyze polysulfides by HPLC, a derivatization process is needed. Derivatization involves the reaction between polysulfides and proper derivatization reagents, by which the generated compounds keep a similar structure to the pristine polysulfides and are more stable and detectable for HPLC analyses.

Diao et al. employed HPLC–MS to qualitatively and semi-quantitatively analyze polysulfide species in Li–S batteries.[270] It has been concluded that Li_2S_4 and Li_2S_6 were the most stable form of polysulfide intermediates. Compared with the active materials in initial cathodes, the total sulfur content in the form of Li_2S_4 and Li_2S_6 that remained was about 20% in the electrolyte when discharging finished. However, 45% sulfur was preserved in the electrolyte mainly in the form of Li_2S_6 at the end of charging. Although sulfur cathodes experienced a serious capacity decay in the early cycles, the content of total sulfur, Li_2S_4, and Li_2S_6 in the electrolyte only changed slightly. It revealed that the transition of polysulfides between the liquid and solid phase maintained a balance. Therefore, the loss of active materials in the electrolyte took the limited responsibility for the capacity decay of Li–S batteries. HPLC–MS provides a critical technique to evaluate the effects of the polysulfide dissolution in the electrolyte on the capacity fading of Li–S batteries.

To qualitatively separate and quantitatively analyze sulfur and various soluble polysulfides, Zheng et al. performed a series of research using HPLC in tandem with other techniques, like UV and MS.[30,271–274] By using HPLC with a UV detector, the authors systematically determined the elemental sulfur solubility in 12 different organic solvents and 22 different electrolytes.[271] It was found that the solubility of elemental sulfur relied on the polarity and the Lewis basicity of solvents. Sulfur showed higher solubility in a nonpolar solvent than in a polar one. A solvent with high Lewis basicity was beneficial to the solubility of sulfur. In the electrolyte systems, the sulfur solubility was greatly influenced by the concentration of supporting salts. Compared with the solubility of sulfur in the pure solvent, sulfur displayed decreased solubility with the increase in the salt concentration in the electrolyte. For example, the sulfur solubility decreased an average of 12.5% and 53.4% in the 0.1 and 1.0 M LiTFSi electrolytes compared with the corresponding solvents, respectively.

Furthermore, Zheng et al. used a novel derivatization reagent to separate polysulfide species in the electrolyte of Li–S batteries. The derivatized polysulfide species were effectively analyzed by HPLC electrospray ionization/mass spectroscopy (electrospray ionization (ESI)/MS).[272] Polysulfide species were well derivatized by 4-(dimethylamino)benzoyl chloride via bonding with two 4-(dimethylamino)benzoyl groups. The formed covalent compounds had retention in a reverse phase HPLC column and were effectively ionized during the ESI process. The collision-induced dissociation (CID) spectra demonstrated the parent ions with m/z 393 ($[RS_3R + H]^+$). The carbon–sulfur bond in the derivatized polysulfides was broken, generating daughter ions of 4-(dimethylamino)benzoyl cation with m/z 148 during the CID process. Based on the ESI/MS analyses, it was concluded that the polysulfides were efficiently derivatized by 4-(dimethylamino)benzoyl chloride, and HPLC ESI/MS achieved the effective separation and detection of the derivatized polysulfides. The polysulfide distribution in the electrolyte was therefore quantitatively and reliably determined. HPLC–MS provides a reliable tool to analyze polysulfides in Li–S batteries, which is critical to revealing the electrochemical mechanisms of sulfur.

HPLC has also been employed to investigate the chemical stability of battery components with polysulfide species by Zheng et al.[274] By monitoring the total sulfur intensity and polysulfide distribution in the HPLC chromatogram, the authors examined the chemical stabilities of five current collectors (Al, Cu, stainless steel (SS304), Ni, and Ti), one polypropylene separator, Celgard 2400), and two binders carboxymethyl cellulose and polyvinylidene fluoride) against polysulfides at different times. **Figure 22**a presents the chromatograms of the polysulfide mixtures after contacting five current collectors for 180 days. Compared with the chromatogram of the stock polysulfides without contacting current collectors, the chromatograms of contacted counterparts displayed distinct distributions of derivatized polysulfides and sulfur. Al, SS304, and Ti current collectors basically maintained the identical chromatograms to the stock one, implying the relative stability with the polysulfide mixture. However, no peaks of either the derivatized polysulfides or the elemental sulfur were observed from Cu, while the distribution of the polysulfide species changed substantially for Ni. These results suggested that Cu and Ni were not chemically stable with polysulfides in the electrolyte. Figure 22b compares the chromatographic results of PP separators (Celgard 2400) and CMC and PVDF binders contacting polysulfide species for 180 days. The polysulfide distribution for the three components did not change evidently. The total sulfur intensities for the three components were constant and identical to one for the stock mixture during the measurement. Combined with other spectroscopic observations, it was concluded that the three components were chemically stable with polysulfides for 180 days at room temperature. This work significantly expands the applications of HPLC techniques in Li–S batteries.

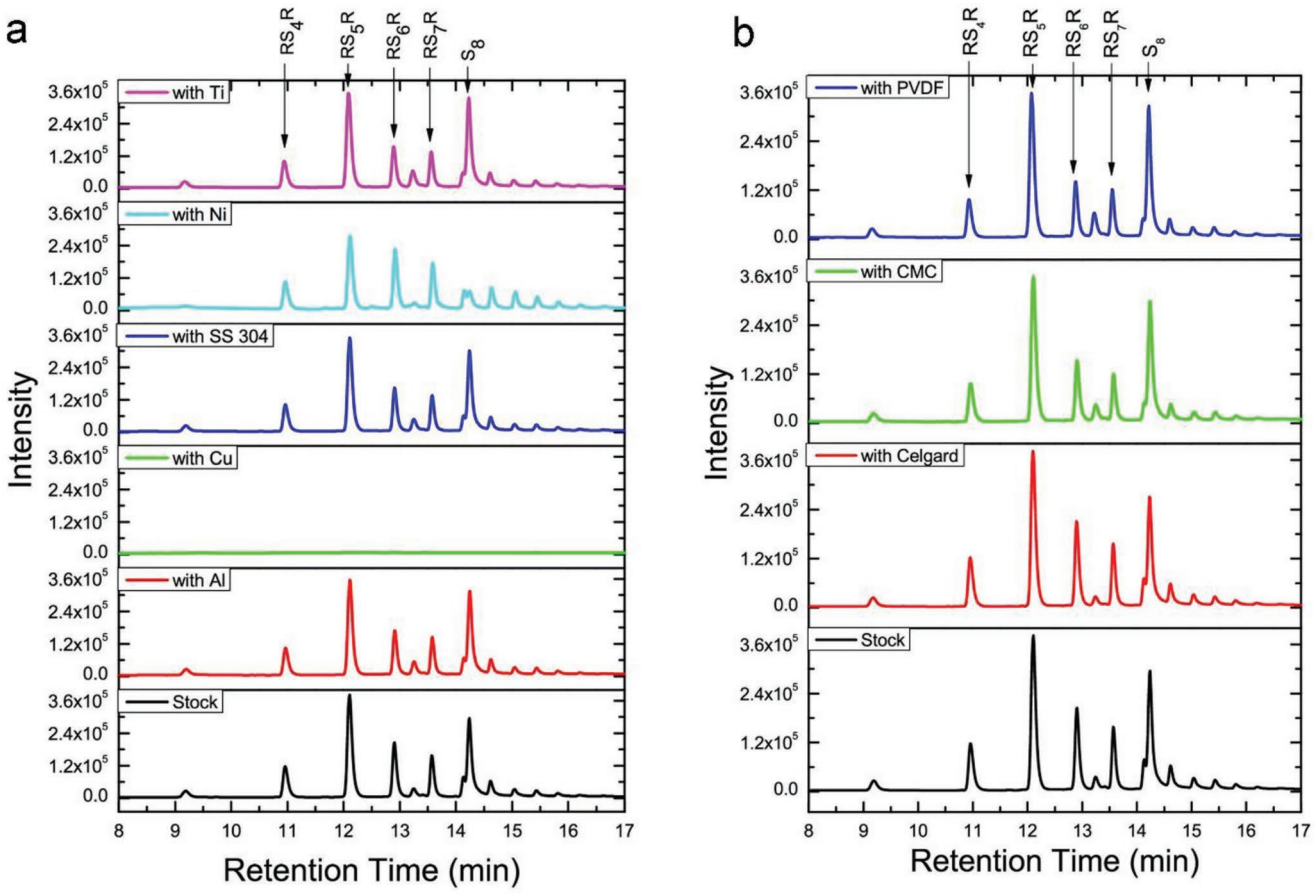

Figure 22. HPLC/UV chromatograms for electrolytes with polysulfides contacting a) different current collectors and b) binders and a separator for 180 days, and for stock electrolytes with polysulfides after resting for 180 days. Reproduced with permission.[274] Copyright 2022, American Chemical Society.

4.3. Theoretical Calculations

Theoretical calculations have been widely employed in energy and catalysis research.[275–277] Compared with experimental methods, theoretical calculations allow people to understand the electrochemical reaction mechanisms and unravel the active sites of catalysts on an atomic scale. The calculation results are highly beneficial to the design and screening of promising electrode materials and catalysts. In Li–S batteries, theoretical calculations typically involve the binding energy of sulfur species and the Gibbs free energy change for SRR. The former provides information about the adsorption interaction between sulfur species and host materials, which is critical to inhibit the shuttle effect of polysulfides.[176,278,279] The latter unravels the conversion kinetics and reaction pathways of SRR, which are highly valuable to evaluate the catalytic activity of materials.[91,156,204]

4.3.1. Binding Energy

Due to the severe dissolution and diffusion of soluble polysulfides into the electrolyte, the introduction of host materials to Li–S batteries, which can adsorb and anchor sulfur species, has been considered an effective strategy to mitigate the polysulfide shuttle.[15,17,280] These materials display the proper binding interaction with sulfur species, significantly enhancing the sulfur utilization upon battery cycling. In contrast to the experimental attempts, calculating the binding energy between host materials and sulfur species can provide quantitative insights into the anchoring effects of host materials. The binding energy based on DFT calculations therefore has been a critical factor in predicting, screening, and designing desirable sulfur host materials for high-performance Li–S batteries. By using DFT calculations, researchers have investigated various materials to demonstrate their adsorption toward sulfur species. Generally, carbon materials show weak binding energy for sulfur species. By contrast, polar materials exhibit strong adsorption toward sulfur species by chemical interactions.[281] For example, Nazar and co-workers calculated the binding energies for different sulfur species at the surface of nonpolar graphite and on three Co_9S_8 surfaces.[282] The results indicated that sulfur species showed considerably stronger binding energy on Co_9S_8 surfaces, which enabled the improved utilization of sulfur cathodes. Cui and co-workers systematically investigated the adsorption of various 2D layered materials (oxides, sulfides, and chlorides) toward polysulfides.[283] As a result, the too strong adsorption of V_2O_5 or MoM_3 to polysulfides with binding energy of more than 2. 0 eV was not beneficial to Li–S batteries since it led to the decomposition of polysulfide species. The

authors concluded that host materials with moderate adsorption would achieve the balance between the binding interaction and structural integrity of sulfur species.

To determine the adsorption of Co-SAs@NC toward sulfur species, Li et al. performed DFT calculations to compare the adsorption energies of Li_2S and Li_2S_6 on the pure carbon (001), N-doped carbon (N—C), and CoN_4—carbon (CoN_4—C) surfaces, respectively.[215] **Figure 23** illustrates the optimized adsorption configurations with the calculated adsorption energies. CoN_4—C revealed stronger adsorption toward Li_2S and Li_2S_6 than pure carbon and N—C, showing that sulfur species could be effectively anchored on Co-SAs@NC. Moreover, the authors also calculated the adsorption energies on the (111) surface of metallic Co. The binding energies of Li_2S and Li_2S_6 on Co were –4.18 and –8.67 eV. Such strong adsorption may break the Li—S bond of polysulfides, resulting in the partial sulfurization of Co nanoparticles. The calculation results were validated by performing battery experiments, where CoN_4—C showed optimal electrochemical performance. Binding energies of sulfur species on carbides,[119,120] nitrides,[128,129] selenides,[112] and tellurides[261,284] have also been reported.

4.3.2. Gibbs Free Energy

The SRR involves the solid–liquid–solid phase transformation with multistep electron transfer. The sluggish conversion kinetics severely impedes the utilization of sulfur species and the rate capability of Li–S batteries. Catalysts which can accelerate the electrochemical reduction process and optimize the reaction pathway are beneficial to the SRR kinetics. The Gibbs free energy of electrode systems can indicate the specific reaction pathway for each step. By calculating the Gibbs free energy for the whole SRR process on the catalyst substrate, several fundamental reaction properties can be obtained, such as the spontaneous exothermic and rate-determining steps. Therefore, the Gibbs free energy for SRR offers a better understanding of the reaction mechanisms and the design of more efficient catalyst materials.

It has been concluded that the initial solid–liquid reduction from S_8 to Li_2S_8 was a spontaneous exothermic process, in which the Gibbs free energy decreased significantly. The following liquid–liquid reduction steps of soluble polysulfides were either endothermic or nearly thermoneutral due to their highly close Gibbs free energies. The final Li_2S deposition typically showed the positive Gibbs free energy, indicating the endothermic process. Catalysts, such as heteroatom-doped carbon,[16,62] single-atom transition metals,[204,210,223,224] sulfides,[102,147] and selenides[115] have been confirmed theoretically to decrease the Gibbs free energy for SRR, leading to thermodynamically more favorable reaction process.

Yu et al. investigated the reduction pathways of sulfur species at Mo_2C and CNT.[119] **Figure 24** shows the optimized configurations and free energy profiles. The sulfur reduction pathways were endothermic except for the conversion from S_8 to Li_2S_8.

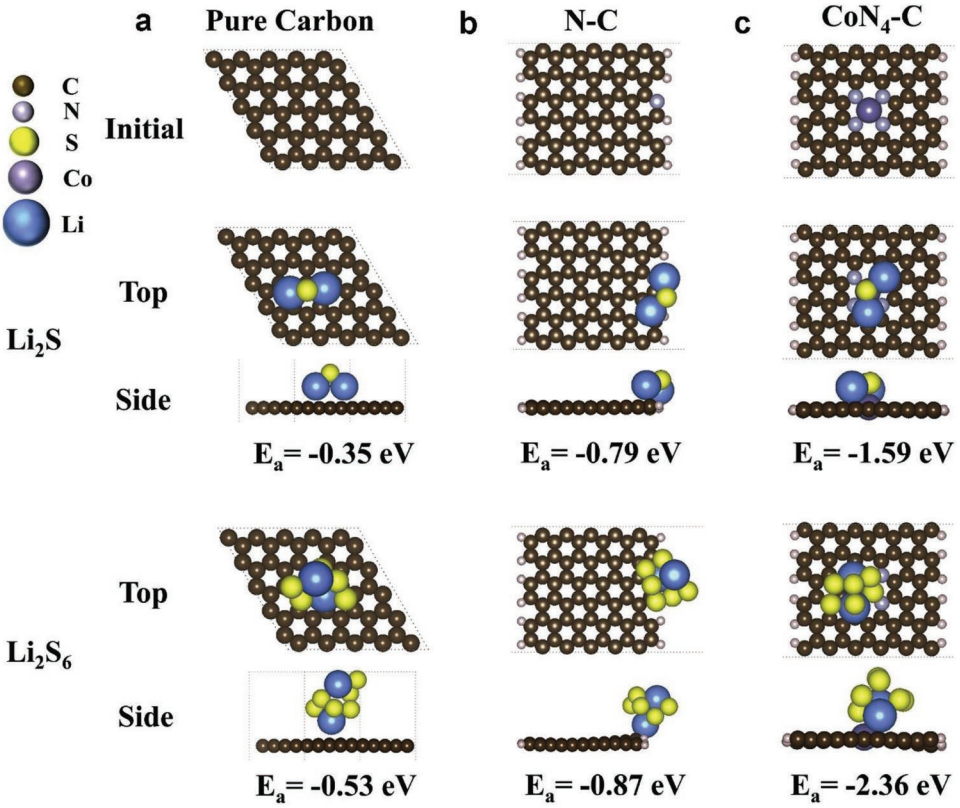

Figure 23. The most stable atomic configurations and the corresponding adsorption energies of Li_2S and Li_2S_6 at a) pure carbon (001), b) N—C, and c) CoN_4—C surfaces. Reproduced with permission.[215] Copyright 2020, Elsevier.

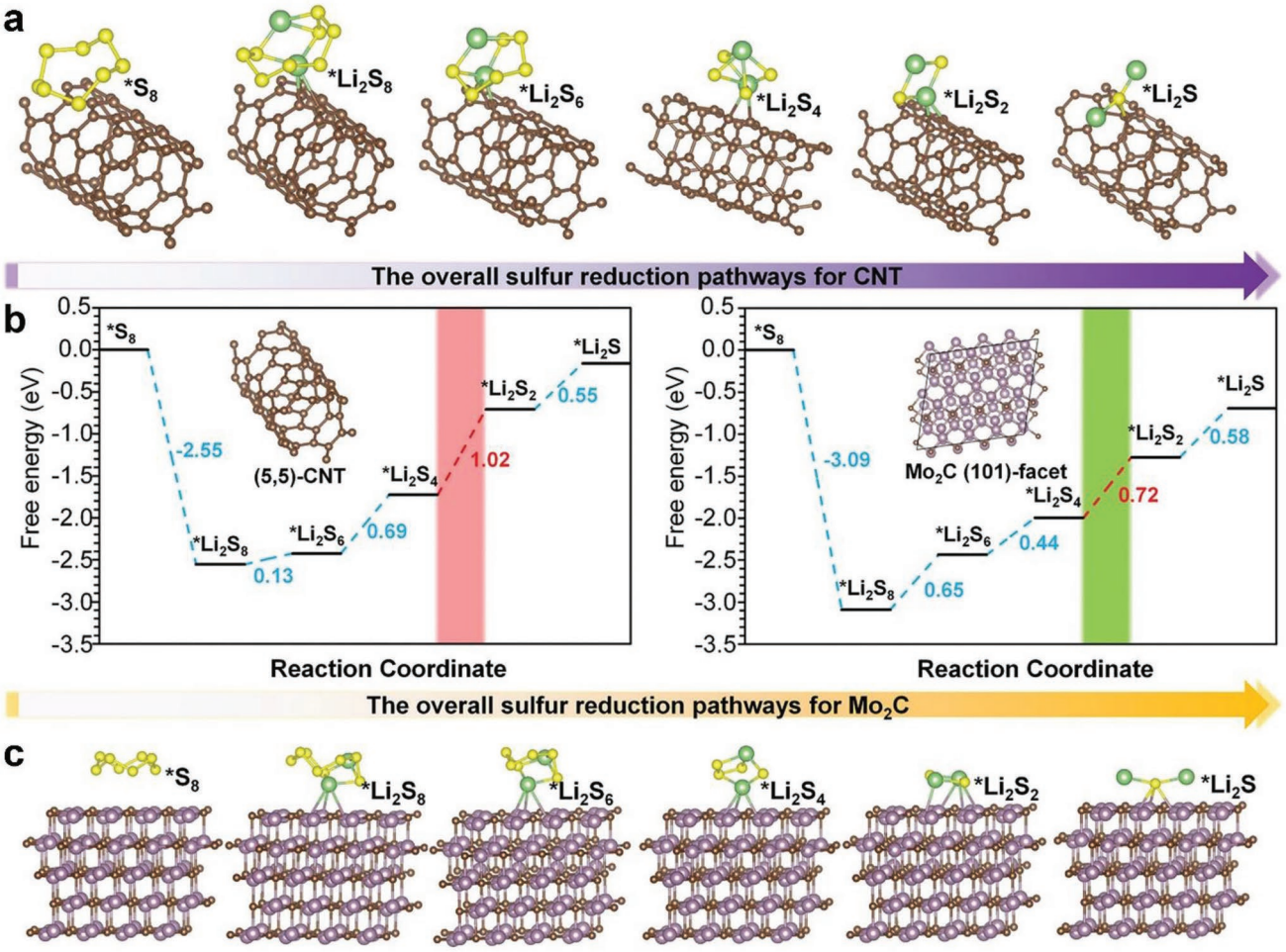

Figure 24. a) Optimized atomic configurations for the binding of Li_2S_n (n = 1, 2, 4, 6, 8) and S_8 to (5,5)-CNT. b) Energy profiles for the reduction of sulfur species at (5,5)-CNT and Mo_2C(101) facet, where the red dashed line represents the potential limiting step. c) Optimized atomic configurations for the binding of Li_2S_n (n = 1, 2, 4, 6, 8) and S_8 to Mo_2C(101) surface. Reproduced with permission.[119] Copyright 2021, Wiley-VCH.

The reduction of Li_2S_4 to Li_2S_2 revealed the most positive Gibbs free energy at CNT and Mo_2C, which was the rate-determining step during the SRR. By contrast, Mo_2C decreased the energy barrier of the rate-determining step from 1.02 to 0.72 eV. This indicates that Mo_2C accelerated the reduction kinetics. On the other hand, research showed that the reduction of Li_2S_2 to Li_2S was the rate-determining step. Single-atom Co and NbB_2 nanoparticles were determined to decrease the conversion barriers, promoting the nucleation and growth of Li_2S.[216,240]

5. Conclusions and Outlook

In this review, we systematically summarize the critical issues of the SRR in Li–S batteries. The conversion mechanisms and reaction pathways of the sulfur reduction have been introduced and correspond to two stages: the solid–liquid reduction from sulfur to polysulfides and Li_2S deposition. The former presents a relatively easy conversion process, whereas the latter needs to overcome high energy barriers, leading to sluggish kinetics. The Li_2S deposition process can therefore be considered as the rate-determining step throughout the SRR. The reaction mechanisms and kinetics strongly rely on the solvent system and electrode structure. This fact offers promising opportunities to explore and design efficient catalysts for enhanced SRR kinetics. Recent advances in catalyst materials for SRR have therefore been discussed. Ideal catalysts should possess good conductivity, proper adsorption toward sulfur species, and abundant catalytic sites. Besides, the high structural stability of catalysts is a prerequisite for prolonged battery cycle life.

The current research on catalysts for SRR has been divided into four classes: carbon, metal compounds, metals, and single atoms. Although tremendous progress has been made to design better catalytic materials for SRR, the current four classes of catalysts still have not addressed the fundamental issues of SRR due to their intrinsic properties. The advantages and disadvantages of various catalytic materials are summarized as follows.

Carbon-based catalysts own large specific surface areas to assist the uniform adsorption of sulfur species and to provide adequate space for the deposition of insoluble Li_2S_2/Li_2S. Good conductivity is beneficial to charge transfer and SRR kinetics. The favorably tunable structures and morphology

allow carbon-based catalysts to achieve effective chemical modulation/doping, which can further enhance the catalytic activities for SRR. Besides, carbon-based materials have facile fabrication strategies with low costs, showing great potential for commercialization. The main disadvantage is the intrinsic chemical inertness of carbon atoms. Pure carbon displays few catalytic effects on SRR due to the weak chemical adsorption, but this can be improved by structural modulation. The introduction of doped heteroatoms, such as N, P, B, and S, significantly changes the electronic structures of carbon. Various heteroatom-doped carbon structures have been demonstrated to catalyze the electrochemical reduction of sulfur species effectively. The doped heteroatoms induce charge redistribution at the adjacent carbon atoms, which can be considered the probable catalytic sites for SRR.

Metal compound catalysts exhibit diverse catalytic properties for SRR compared to carbon. For one thing, metal compounds possess effective chemical adsorption toward sulfur species, which is critical to the catalytic reaction. Another advantage is the abundant active sites at the surface of metal compounds. This significantly enlarges the catalyst activities with a small amount used in sulfur cathodes. However, some of metal compounds, like oxides, show relatively low conductivity, hindering the charge transfer kinetics of SRR. A series of strategies, such as heterostructures, morphology optimization, and defect engineering have been developed to enhance the catalytic activities, which are discussed in this review. In addition, too strong chemical adsorption of some metal compounds is harmful to the desorption process of SRR, since the interaction may destroy the structures of sulfur species and cause the loss of active materials.

Metal catalysts show excellent catalytic activities for SRR. Metal nanoparticles generally possess relatively high surface energies due to the small size effects. This advantage benefits the chemical adsorption and activation of sulfur species during catalytic reactions, which decreases the reaction barriers for sulfur reduction. Moreover, their good electrical conductivity accelerates the conversion kinetics of sulfur species. Some noble metals (e.g., Pt and Ir), transition metals (e.g., Fe, Co, and Ni), and alloys have been introduced to Li–S batteries. The principal issue that decreases the catalytic activities of metals is structural stability. The possible agglomeration of metal nanoparticles limits the sufficient exposure of active sites. Alternatively, metal nanoparticles are typically combined with various carbon substrates to enlarge the number of active sites, which can therefore achieve the optimal catalytic performance of SRR. Another disadvantage for metal catalysts is the cost. Since some noble metals are expensive, their applications on a large scale are therefore limited.

Single atoms exhibit considerable potential for accelerating the SRR kinetics as emerging catalysts. Single-atom catalysts can maximize the atomic utilization efficiency and achieve full exposure of active sites. The adequate utilization of single-atom catalysts will yield higher energy density Li–S batteries. Furthermore, the metal content in single-atom catalysts is relatively low, considerably decreasing the application cost compared with metals. The challenging problem is the complicated fabrication of high-quality single-atom catalysts, as single atoms show the high tendency for agglomeration. Besides, the structural stability of single-atom catalysts is still unclear during battery cycling.

To understand the reaction mechanisms of SRR and catalyst activities, the output of different characterization approaches must be integrated. Therefore, the current techniques applied to SRR in terms of electrochemical measurements, spectroscopic techniques, and theoretical calculations, were systematically reviewed. The typical features and functions of these techniques have been presented. Electrochemical measurements can provide valuable information about electrode reactions, such as the charge transfer processes, reaction overpotentials, and activation energies. These properties allow scientists to analyze and compare the catalytic effects of materials with respect to the SRR kinetics. Spectroscopic techniques, especially in situ or in operando spectroscopic techniques, can monitor battery reaction processes in real time. By probing the structural evolution of sulfur species, they will give detailed insights into the reaction mechanisms of SRR and catalyst activities. In addition, theoretical calculations will help to improve our understanding of electrochemical reaction mechanisms and catalytic active sites on an atomic scale. These calculation results offer improved design and screening of promising electrode materials and catalysts.

As discussed in this review, many attempts have been made to understand the SRR in Li–S batteries. However, due to the complexity of the multistep electron transfer reaction, research on SRR is still in its infancy. Both challenges and opportunities will be present in future research on the mechanisms of SRR and catalyst activities. The first key point is the fundamental understanding of the catalytic mechanisms of SRR in Li–S batteries. The complicated conversion process poses a significant challenge in identifying the specific reaction pathways of electrocatalytic sulfur reduction. Current research mainly focuses on the reduction kinetics of Li_2S deposition. However, more attention should be drawn to the formation and conversion of sulfur intermediates, such as various soluble polysulfides and insoluble Li_2S_2, despite the considerable difficulties in probing the reduction process. Determining and optimizing their reaction pathways and kinetics is essential since the final Li_2S deposition process depends heavily on these sulfur intermediates.

Another critical point is to seek rational solutions for fairly evaluating and comparing catalyst activities. Many reports have shown that various materials exhibit excellent catalytic activities for SRR. The straightforward criteria for evaluating the catalyst activities are the electrochemical performance of the resulting Li–S batteries, such as the specific capacity, rate capability, and cycling stability. An excellent SRR catalyst can significantly improve the electrode reaction kinetics and mitigate the polysulfide shuttle. Therefore, a higher discharging capacity and stronger rate performance are achieved. In addition, based on the intrinsic properties of catalyst materials, they can decrease the reaction activation energies. Several electrochemical parameters are available to estimate the catalyst activities for SRR in the equivalent experimental conditions, such as the reaction overpotential and Tafel slopes for SRR. Also, the activation energies for each reduction step of sulfur and the capacity for Li_2S deposition are important to reflect the catalyst performance. Besides, the change of reaction pathways for SRR obtained

from spectroscopic analyses and theoretical calculations would be another valuable guideline for catalyst evaluation.

However, it is not easy to compare different reports about catalyst activities because they are evaluated under different conditions. By contrast, ORR and hydrogen evolution reaction have unified evaluation criteria, such as the onset potential, overpotential, and Tafel slope. These parameters can be directly compared with the benchmark. In Li–S batteries, these values obtained from different experimental conditions are difficult to make a direct comparison, since the battery configuration and electrolyte components are generally distinct. Therefore, rational evaluation strategies are also beneficial for designing and screening highly efficient catalysts for SRR. Finally, developing more efficient and straightforward characterization approaches is critical to accurately detect various sulfur species and unravel the complex conversion pathways during SRR. It is highly recommended to develop more advanced in situ characterization approaches for SRR, which can reflect the real-time evolution of sulfur species.

In conclusion, this review provides a cutting-edge insight into SRR in Li–S batteries. Recent advances have demonstrated enhanced SRR kinetics of various catalyst materials. However, more studies need to be performed to clarify the underlying mechanisms, design more efficient catalysts, and develop advanced characterization approaches. It is believed that the fundamental understanding of SRR will further increase practical applications of high-performance Li–S batteries.

Acknowledgements

This work was supported by the Natural Science Foundation of Jiangsu Province, China (Grant No. BK20220540) and the Research Foundation for Advanced Talents of Jiangsu University, China (Grant No. 22JDG010).

Conflict of Interest

The authors declare no conflict of interest.

Keywords

catalysts, characterization, lithium–sulfur batteries, mechanisms, sulfur reduction reaction

Received: June 21, 2022
Revised: August 17, 2022
Published online: September 18, 2022

[1] M. Armand, J. M. Tarascon, *Nature* **2008**, *451*, 652.
[2] S. Chu, Y. Cui, N. Liu, *Nat. Mater.* **2017**, *16*, 16.
[3] F. Duffner, N. Kronemeyer, J. Tübke, J. Leker, M. Winter, R. Schmuch, *Nat. Energy* **2021**, *6*, 123.
[4] J. M. Tarascon, M. Armand, *Nature* **2001**, *414*, 359.
[5] P. G. Bruce, S. A. Freunberger, L. J. Hardwick, J. M. Tarascon, *Nat. Mater.* **2012**, *11*, 19.
[6] Q. Pang, X. Liang, C. Y. Kwok, L. F. Nazar, *Nat. Energy* **2016**, *1*, 16132.
[7] Y. Chen, T. Wang, H. Tian, D. Su, Q. Zhang, G. Wang, *Adv. Mater.* **2021**, *33*, 2003666.
[8] M. A. Pope, I. A. Aksay, *Adv. Energy Mater.* **2015**, *5*, 1500124.
[9] A. Manthiram, Y. Fu, Y. Su, *Acc. Chem. Res.* **2013**, *46*, 1125.
[10] D. Lin, Y. Liu, Y. Cui, *Nat. Nanotechnol.* **2017**, *12*, 194.
[11] X.-B. Cheng, R. Zhang, C.-Z. Zhao, Q. Zhang, *Chem. Rev.* **2017**, *117*, 10403.
[12] B. Liu, J.-G. Zhang, W. Xu, *Joule* **2018**, *2*, 833.
[13] X. Ji, K. T. Lee, L. F. Nazar, *Nat. Mater.* **2009**, *8*, 500.
[14] Z. W. Seh, W. Li, J. J. Cha, G. Zheng, Y. Yang, M. T. McDowell, P. C. Hsu, Y. Cui, *Nat. Commun.* **2013**, *4*, 1331.
[15] Z. Yuan, H. J. Peng, T. Z. Hou, J. Q. Huang, C. M. Chen, D. W. Wang, X. B. Cheng, F. Wei, Q. Zhang, *Nano Lett.* **2016**, *16*, 519.
[16] L. Peng, Z. Wei, C. Wan, J. Li, Z. Chen, D. Zhu, D. Baumann, H. Liu, C. S. Allen, X. Xu, A. I. Kirkland, I. Shakir, Z. Almutairi, S. Tolbert, B. Dunn, Y. Huang, P. Sautet, X. Duan, *Nat. Catal.* **2020**, *3*, 762.
[17] L. Zhou, D. L. Danilov, R. A. Eichel, P. H. L. Notten, *Adv. Energy Mater.* **2021**, *11*, 2001304.
[18] S. Bai, X. Liu, K. Zhu, S. Wu, H. Zhou, *Nat. Energy* **2016**, *1*, 16094.
[19] H. Ye, J. Y. Lee, *Small Methods* **2020**, *4*, 1900864.
[20] H. Al Salem, G. Babu, C. V. Rao, L. M. Arava, *J. Am. Chem. Soc.* **2015**, *137*, 11542.
[21] H. Lin, L. Yang, X. Jiang, G. Li, T. Zhang, Q. Yao, G. W. Zheng, J. Y. Lee, *Energy Environ. Sci.* **2017**, *10*, 1476.
[22] D. Liu, C. Zhang, G. Zhou, W. Lv, G. Ling, L. Zhi, Q. H. Yang, *Adv. Sci.* **2018**, *5*, 1700270.
[23] Q. He, Y. Gorlin, M. U. M. Patel, H. A. Gasteiger, Y.-C. Lu, *J. Electrochem. Soc.* **2018**, *165*, A4027.
[24] A. Evans, M. I. Montenegro, D. Pletcher, *Electrochem. Commun.* **2001**, *3*, 514.
[25] Y. Jung, S. Kim, B.-S. Kim, D.-H. Han, S.-M. Park, J. Kwak, *Int. J. Electrochem. Sci.* **2008**, *3*, 566.
[26] N. S. Manan, L. Aldous, Y. Alias, P. Murray, L. J. Yellowlees, M. C. Lagunas, C. Hardacre, *J. Phys. Chem. B* **2011**, *115*, 13873.
[27] D.-H. Han, B.-S. Kim, S.-J. Choi, Y. Jung, J. Kwak, S.-M. Park, *J. Electrochem. Soc.* **2004**, *151*, E283.
[28] Y.-C. Lu, Q. He, H. A. Gasteiger, *J. Phys. Chem. C* **2014**, *118*, 5733.
[29] P. Schön, F. Hintz, U. Krewer, *Electrochim. Acta* **2019**, *295*, 926.
[30] D. Zheng, X. Zhang, J. Wang, D. Qu, X. Yang, D. Qu, *J. Power Sources* **2016**, *301*, 312.
[31] P. Andrei, C. Shen, J. P. Zheng, *Electrochim. Acta* **2018**, *284*, 469.
[32] G.-Y. Du, C.-Y. Liu, E. Y. Li, *Catalysts* **2020**, *10*, 911.
[33] V. Thangavel, A. Mastouri, C. Guéry, M. Morcrette, A. A. Franco, *Batteries Supercaps* **2021**, *4*, 152.
[34] P. Schön, U. Krewer, *Electrochim. Acta* **2021**, *373*, 137523.
[35] T. Danner, A. Latz, *Electrochim. Acta* **2019**, *322*, 134719.
[36] Q. Zou, Y. C. Lu, *J. Phys. Chem. Lett.* **2016**, *7*, 1518.
[37] D. Zheng, G. Wang, D. Liu, J. Si, T. Ding, D. Qu, X. Yang, D. Qu, *Adv. Mater. Technol.* **2018**, *3*, 1700233.
[38] C. Barchasz, F. Molton, C. Duboc, J. C. Lepretre, S. Patoux, F. Alloin, *Anal. Chem.* **2012**, *84*, 3973.
[39] D. Zheng, D. Liu, J. B. Harris, T. Ding, J. Si, S. Andrew, D. Qu, X. Q. Yang, D. Qu, *ACS Appl. Mater. Interfaces* **2017**, *9*, 4326.
[40] A. Kawase, S. Shirai, Y. Yamoto, R. Arakawa, T. Takata, *Phys. Chem. Chem. Phys.* **2014**, *16*, 9344.
[41] M. Vijayakumar, N. Govind, E. Walter, S. D. Burton, A. Shukla, A. Devaraj, J. Xiao, J. Liu, C. Wang, A. Karim, S. Thevuthasan, *Phys. Chem. Chem. Phys.* **2014**, *16*, 10923.
[42] Q. Wang, J. Zheng, E. Walter, H. Pan, D. Lv, P. Zuo, H. Chen, Z. D. Deng, B. Y. Liaw, X. Yu, X. Yang, J.-G. Zhang, J. Liu, J. Xiao, *J. Electrochem. Soc.* **2015**, *162*, A474.
[43] Z. Liu, D. Hubble, P. B. Balbuena, P. P. Mukherjee, *Phys. Chem. Chem. Phys.* **2015**, *17*, 9032.

[44] Y. X. Ren, T. S. Zhao, M. Liu, P. Tan, Y. K. Zeng, *J. Power Sources* **2016**, *336*, 115.
[45] S. Y. Lang, Y. Shi, Y. G. Guo, D. Wang, R. Wen, L. J. Wan, *Angew. Chem., Int. Ed.* **2016**, *55*, 15835.
[46] M. Cuisinier, C. Hart, M. Balasubramanian, A. Garsuch, L. F. Nazar, *Adv. Energy Mater.* **2015**, *5*, 1401801.
[47] H. Pan, J. Chen, R. Cao, V. Murugesan, N. N. Rajput, K. S. Han, K. Persson, L. Estevez, M. H. Engelhard, J.-G. Zhang, K. T. Mueller, Y. Cui, Y. Shao, J. Liu, *Nat. Energy* **2017**, *2*, 813.
[48] F. Y. Fan, W. C. Carter, Y. M. Chiang, *Adv. Mater.* **2015**, *27*, 5203.
[49] F. Y. Fan, Y.-M. Chiang, *J. Electrochem. Soc.* **2017**, *164*, A917.
[50] Z. Li, Y. Zhou, Y. Wang, Y.-C. Lu, *Adv. Energy Mater.* **2019**, *9*, 1802207.
[51] R. Fang, K. Chen, L. Yin, Z. Sun, F. Li, H. M. Cheng, *Adv. Mater.* **2019**, *31*, 1800863.
[52] H. Shi, W. Lv, C. Zhang, D.-W. Wang, G. Ling, Y. He, F. Kang, Q.-H. Yang, *Adv. Funct. Mater.* **2018**, *28*, 1800508.
[53] J. Wang, K. Jiang, B. Shen, M. Zhen, *ACS Sustainable Chem. Eng.* **2020**, *8*, 749.
[54] Y. Zou, D. Guo, B. Yang, L. Zhou, P. Lin, J. Wang, X. Chen, S. Wang, *ACS Appl. Mater. Interfaces* **2021**, *13*, 50093.
[55] S. C. Jo, J. W. Hong, I. H. Choi, M. J. Kim, B. G. Kim, Y. J. Lee, H. Y. Choi, D. Kim, T. Kim, K. J. Baeg, J. W. Park, *Small* **2022**, *18*, 2200326.
[56] H. Ci, M. Wang, Z. Sun, C. Wei, J. Cai, C. Lu, G. Cui, Z. Liu, J. Sun, *J. Energy Chem.* **2022**, *66*, 474.
[57] Y. Liu, H. Guo, B. Zhang, G. Wen, R. Vajtai, L. Wu, P. M. Ajayan, L. Wang, *Batteries Supercaps* **2020**, *3*, 1201.
[58] Q. Xiao, G. Li, M. Li, R. Liu, H. Li, P. Ren, Y. Dong, M. Feng, Z. Chen, *J. Energy Chem.* **2020**, *44*, 61.
[59] M. Zhang, Z. Zhang, F. Li, H. Mao, W. Liu, D. Ruan, X. Jia, Y. Yang, X. Yu, *Electrochim. Acta* **2021**, *397*, 139268.
[60] J. Lin, Y. Mo, S. Li, J. Yu, *J. Mater. Chem. A* **2022**, *10*, 690.
[61] L. Du, Q. Wu, L. Yang, X. Wang, R. Che, Z. Lyu, W. Chen, X. Wang, Z. Hu, *Nano Energy* **2019**, *57*, 34.
[62] H. Xu, Q. Jiang, B. Zhang, C. Chen, Z. Lin, *Adv. Mater.* **2020**, *32*, 1906357.
[63] Z. Jin, T. Lin, H. Jia, B. Liu, Q. Zhang, L. Li, L. Zhang, Z. M. Su, C. Wang, *ACS Nano* **2021**, *15*, 7318.
[64] M.-e. Zhong, J. Guan, J. Sun, H. Guo, Z. Xiao, N. Zhou, Q. Gui, D. Gong, *Electrochim. Acta* **2019**, *299*, 600.
[65] D. Wu, J. Liu, J. Chen, H. Li, R. Cao, W. Zhang, Z. Gao, K. Jiang, *J. Mater. Chem. A* **2021**, *9*, 5497.
[66] K. Zou, W. Jing, X. Dai, X. Chen, M. Shi, Z. Yao, T. Zhu, J. Sun, Y. Chen, Y. Liu, Y. Liu, *Small* **2022**, *18*, 2107380.
[67] L. Zhang, W. Zhao, S. Yuan, F. Jiang, X. Chen, Y. Yang, P. Ge, W. Sun, X. Ji, *J. Energy Chem.* **2021**, *60*, 531.
[68] X. Liu, J. Q. Huang, Q. Zhang, L. Mai, *Adv. Mater.* **2017**, *29*, 1601759.
[69] B. Yan, X. Li, W. Xiao, J. Hu, L. Zhang, X. Yang, *J. Mater. Chem. A* **2020**, *8*, 17848.
[70] J. Xu, T. Lawson, H. Fan, D. Su, G. Wang, *Adv. Energy Mater.* **2018**, *8*, 1702607.
[71] X. Liang, C. Hart, Q. Pang, A. Garsuch, T. Weiss, L. F. Nazar, *Nat. Commun.* **2015**, *6*, 5682.
[72] S. Wang, J. Liao, X. Yang, J. Liang, Q. Sun, J. Liang, F. Zhao, A. Koo, F. Kong, Y. Yao, X. Gao, M. Wu, S.-Z. Yang, R. Li, X. Sun, *Nano Energy* **2019**, *57*, 230.
[73] L. Zhou, H. Li, X. Wu, Y. Zhang, D. L. Danilov, R.-A. Eichel, P. H. L. Notten, *ACS Appl. Energy Mater.* **2019**, *2*, 8153.
[74] G. Liu, K. Feng, H. Cui, J. Li, Y. Liu, M. Wang, *Chem. Eng. J.* **2020**, *381*, 122652.
[75] B. Jiang, D. Tian, Y. Qiu, X. Song, Y. Zhang, X. Sun, H. Huang, C. Zhao, Z. Guo, L. Fan, N. Zhang, *Nano-Micro Lett.* **2022**, *14*, 40.
[76] Y. He, S. Yao, M. Bi, H. Yu, A. Majeed, X. Shen, *Electrochim. Acta* **2021**, *394*, 139126.
[77] L. Zhou, D. L. Danilov, F. Qiao, R.-A. Eichel, P. H. L. Notten, *Electrochim. Acta* **2022**, *414*, 140231.
[78] Y. He, M. Bi, H. Yu, C. Zhang, A. Majeed, X. Shen, S. Yao, *ChemElectroChem* **2021**, *8*, 4564.
[79] J. Liu, M. Zhu, Z. Shen, T. Han, T. Si, C. Hu, H. Zhang, *Small* **2021**, *17*, 2103051.
[80] C. Zhou, M. Li, M. Hong, N. Hu, Z. Yang, L. Zhang, Y. Zhang, *Chem. Eng. J.* **2021**, *421*, 129707.
[81] T. Xiao, L. Zhao, H. Ge, M. Yang, W. Liu, G. Li, M. Ren, X. Zhang, Z. Zhou, *Chem. Eng. J.* **2022**, *439*, 135790.
[82] B. Z. Yang, P. Xie, Q. Luo, Z. W. Li, C. Y. Zhou, Y. H. Yin, X. B. Liu, Y. S. Li, Z. P. Wu, *Adv. Funct. Mater.* **2022**, *32*, 2110665.
[83] F. Liu, G. Sun, H. B. Wu, G. Chen, D. Xu, R. Mo, L. Shen, X. Li, S. Ma, R. Tao, X. Li, X. Tan, B. Xu, G. Wang, B. S. Dunn, P. Sautet, Y. Lu, *Nat. Commun.* **2020**, *11*, 5215.
[84] W. Hua, H. Li, C. Pei, J. Xia, Y. Sun, C. Zhang, W. Lv, Y. Tao, Y. Jiao, B. Zhang, S. Z. Qiao, Y. Wan, Q. H. Yang, *Adv. Mater.* **2021**, *33*, 2101006.
[85] H. Li, C. Chen, Y. Yan, T. Yan, C. Cheng, D. Sun, L. Zhang, *Adv. Mater.* **2021**, *33*, 2105067.
[86] T. Sun, X. Zhao, B. Li, H. Shu, L. Luo, W. Xia, M. Chen, P. Zeng, X. Yang, P. Gao, Y. Pei, X. Wang, *Adv. Funct. Mater.* **2021**, *31*, 2101285.
[87] Y. Liu, Z. Ma, G. Yang, Z. Wu, Y. Li, J. Gu, J. Gautam, X. Gong, A. N. Chishti, S. Duan, C. Chen, M. Chen, L. Ni, G. Diao, *Adv. Funct. Mater.* **2021**, *32*, 2109462.
[88] W. Sun, Y.-C. Lu, Y. Huang, *J. Mater. Chem. A* **2021**, *9*, 21184.
[89] Y. Guo, T. Park, J. W. Yi, J. Henzie, J. Kim, Z. Wang, B. Jiang, Y. Bando, Y. Sugahara, J. Tang, Y. Yamauchi, *Adv. Mater.* **2019**, *31*, 1807134.
[90] M. Shi, Z. Liu, S. Zhang, S. Liang, Y. Jiang, H. Bai, Z. Jiang, J. Chang, J. Feng, W. Chen, H. Yu, S. Liu, T. Wei, Z. Fan, *Adv. Energy Mater.* **2022**, *12*, 2103657.
[91] J. Yu, J. Xiao, A. Li, Z. Yang, L. Zeng, Q. Zhang, Y. Zhu, L. Guo, *Angew. Chem., Int. Ed.* **2020**, *59*, 13071.
[92] J.-L. Yang, S.-X. Zhao, X.-T. Zeng, Y.-M. Lu, G.-z. Cao, *Adv. Mater. Interfaces* **2019**, *7*, 1901420.
[93] Y. Zhang, G. Xu, Q. Kang, L. Zhan, W. Tang, Y. Yu, K. Shen, H. Wang, X. Chu, J. Wang, S. Zhao, Y. Wang, L. Ling, S. Yang, *J. Mater. Chem. A* **2019**, *7*, 16812.
[94] J. He, A. Bhargav, H. Yaghoobnejad Asl, Y. Chen, A. Manthiram, *Adv. Energy Mater.* **2020**, *10*, 2001017.
[95] Y. Li, J. Xu, D. Xu, Y. He, X. Sun, D. Niu, X. Zhang, *ChemElectroChem* **2021**, *8*, 1642.
[96] Q. Yuan, Y. Chen, M. Jia, J. Guan, P. Zhao, H. Zheng, H. Qiu, M. Jia, H. Song, *ACS Appl. Mater. Interfaces* **2021**, *13*, 38229.
[97] G. Babu, N. Masurkar, H. Al Salem, L. M. Arava, *J. Am. Chem. Soc.* **2017**, *139*, 171.
[98] J. He, G. Hartmann, M. Lee, G. S. Hwang, Y. Chen, A. Manthiram, *Energy Environ. Sci.* **2019**, *12*, 344.
[99] W. Yang, W. Yang, L. Dong, X. Gao, G. Wang, G. Shao, *J. Mater. Chem. A* **2019**, *7*, 13103.
[100] B. Yu, Y. Chen, Z. Wang, D. Chen, X. Wang, W. Zhang, J. He, W. He, *J. Power Sources* **2020**, *447*, 227364.
[101] H. Lin, S. Zhang, T. Zhang, H. Ye, Q. Yao, G. W. Zheng, J. Y. Lee, *Adv. Energy Mater.* **2019**, *9*, 1902096.
[102] D. Tian, X. Song, Y. Qiu, X. Sun, B. Jiang, C. Zhao, Y. Zhang, X. Xu, L. Fan, N. Zhang, *ACS Nano* **2021**, *15*, 16515.
[103] J. Xu, W. Zhang, H. Fan, F. Cheng, D. Su, G. Wang, *Nano Energy* **2018**, *51*, 73.
[104] C. Shen, K. Zhang, Y. You, H. Wang, R. Ning, Y. Qi, N. Li, C. Ding, K. Xie, B. Wei, *Nanoscale* **2020**, *12*, 13980.

[105] H. Zhang, M. Zou, W. Zhao, Y. Wang, Y. Chen, Y. Wu, L. Dai, A. Cao, *ACS Nano* **2019**, *13*, 3982.
[106] J. Liu, Y. Song, C. Lin, Q. Xie, D.-L. Peng, R.-J. Xie, *Sci. China Mater.* **2022**, *65*, 947.
[107] C. Y. Zhang, G. W. Sun, Z. De Shi, Q. Y. Liu, J. L. Pan, Y. C. Wang, H. Zhao, G. Z. Sun, X. P. Gao, X. J. Pan, J. Y. Zhou, *Energy Storage Mater.* **2021**, *43*, 471.
[108] Q. Zhao, R. Wang, J. Wen, X. Hu, Z. Li, M. Li, F. Pan, C. Xu, *Nano Energy* **2022**, *95*, 106982.
[109] H. Yuan, H.-J. Peng, B.-Q. Li, J. Xie, L. Kong, M. Zhao, X. Chen, J.-Q. Huang, Q. Zhang, *Adv. Energy Mater.* **2019**, *9*, 1802768.
[110] L. He, D. Yang, H. Zhao, L. Wei, D. Wang, Y. Wang, G. Chen, Y. Wei, *Chem. Eng. J.* **2022**, *440*, 135820.
[111] D. Cai, B. Liu, D. Zhu, D. Chen, M. Lu, J. Cao, Y. Wang, W. Huang, Y. Shao, H. Tu, W. Han, *Adv. Energy Mater.* **2020**, *10*, 1904273.
[112] Z. Ye, Y. Jiang, L. Li, F. Wu, R. Chen, *Adv. Mater.* **2020**, *32*, 2002168.
[113] C. Zhang, J. J. Biendicho, T. Zhang, R. Du, J. Li, X. Yang, J. Arbiol, Y. Zhou, J. R. Morante, A. Cabot, *Adv. Funct. Mater.* **2019**, *29*, 1903842.
[114] W. Tian, B. Xi, Z. Feng, H. Li, J. Feng, S. Xiong, *Adv. Energy Mater.* **2019**, *9*, 1901896.
[115] C. Li, W. Ge, S. Qi, L. Zhu, R. Huang, M. Zhao, Y. Qian, L. Xu, *Adv. Energy Mater.* **2022**, *12*, 2103915.
[116] C. Zhang, B. Fei, D. Yang, H. Zhan, J. Wang, J. Diao, J. Li, G. Henkelman, D. Cai, J. J. Biendicho, J. R. Morante, A. Cabot, *Adv. Funct. Mater.* **2022**, *32*, 2201322.
[117] R. Razaq, D. Sun, Y. Xin, Q. Li, T. Huang, L. Zheng, Z. Zhang, Y. Huang, *Nanotechnology* **2018**, *29*, 295401.
[118] R. Razaq, N. Zhang, Y. Xin, Q. Li, J. Wang, Z. Zhang, *EcoMat* **2020**, *2*, e12020.
[119] B. Yu, A. Huang, D. Chen, K. Srinivas, X. Zhang, X. Wang, B. Wang, F. Ma, C. Liu, W. Zhang, J. He, Z. Wang, Y. Chen, *Small* **2021**, *17*, 2100460.
[120] W. Li, X. Jin, L. Xiao, X. Li, Q. Xu, J. Weng, J. Xu, *J. Mater. Chem. A* **2021**, *9*, 26051.
[121] K. Wu, Y. Hu, Z. Cheng, P. Pan, M. Zhang, L. Jiang, J. Mao, C. Ni, Y. Zhang, Z. Wang, X. Gu, X. Zhang, *J. Alloys Compd.* **2020**, *847*, 156443.
[122] X.-J. Hong, C.-L. Song, Z.-M. Wu, Z.-H. Li, Y.-P. Cai, C.-X. Wang, H. Wang, *Chem. Eng. J.* **2021**, *404*, 126566.
[123] T. Wang, D. Luo, Y. Zhang, Z. Zhang, J. Wang, G. Cui, X. Wang, A. Yu, Z. Chen, *ACS Nano* **2021**, *15*, 19457.
[124] B. Hao, H. Li, W. Lv, Y. Zhang, S. Niu, Q. Qi, S. Xiao, J. Li, F. Kang, Q.-H. Yang, *Nano Energy* **2019**, *60*, 305.
[125] M. Zhao, H. J. Peng, Z. W. Zhang, B. Q. Li, X. Chen, J. Xie, X. Chen, J. Y. Wei, Q. Zhang, J. Q. Huang, *Angew. Chem., Int. Ed.* **2019**, *58*, 3779.
[126] Z. Sun, S. Vijay, H. H. Heenen, A. Y. S. Eng, W. Tu, Y. Zhao, S. W. Koh, P. Gao, Z. W. Seh, K. Chan, H. Li, *Adv. Energy Mater.* **2020**, *10*, 1904010.
[127] W. Zhang, B. Xu, L. Zhang, W. Li, S. Li, J. Zhang, G. Jiang, Z. Cui, H. Song, N. Grundish, K. Shi, B. Zhang, Y. Fan, F. Pan, Q. Liu, L. Du, *Small* **2022**, *18*, 2105664.
[128] X. Yang, S. Chen, W. Gong, X. Meng, J. Ma, J. Zhang, L. Zheng, H. D. Abruna, J. Geng, *Small* **2020**, *16*, 2004950.
[129] F. Li, M. Zhang, W. Chen, X. Cai, H. Rao, J. Chang, Y. Fang, X. Zhong, Y. Yang, Z. Yang, X. Yu, *ACS Appl. Mater. Interfaces* **2021**, *13*, 30746.
[130] T. Zhou, W. Lv, J. Li, G. Zhou, Y. Zhao, S. Fan, B. Liu, B. Li, F. Kang, Q.-H. Yang, *Energy Environ. Sci.* **2017**, *10*, 1694.
[131] P. Xue, K. Zhu, W. Gong, J. Pu, X. Li, C. Guo, L. Wu, R. Wang, H. Li, J. Sun, G. Hong, Q. Zhang, Y. Yao, *Adv. Energy Mater.* **2022**, *12*, 2200308.
[132] L. Jiao, C. Zhang, C. Geng, S. Wu, H. Li, W. Lv, Y. Tao, Z. Chen, G. Zhou, J. Li, G. Ling, Y. Wan, Q. H. Yang, *Adv. Energy Mater.* **2019**, *9*, 1900219.
[133] D. Li, H. Li, S. Zheng, N. Gao, S. Li, J. Liu, L. Hou, J. Liu, B. Miao, J. Bai, Z. Cui, N. Wang, B. Wang, Y. Zhao, *J. Colloid Interface Sci.* **2022**, *607*, 655.
[134] L. Ma, L.-J. Yu, J. Liu, Y.-Q. Su, S. Li, X. Zang, T. Meng, S. Zhang, J. Song, J. Wang, X. Zhao, Z. Cui, N. Wang, Y. Zhao, *Energy Storage Mater.* **2022**, *44*, 180.
[135] Y. Yao, H. Wang, H. Yang, S. Zeng, R. Xu, F. Liu, P. Shi, Y. Feng, K. Wang, W. Yang, X. Wu, W. Luo, Y. Yu, *Adv. Mater.* **2020**, *32*, 1905658.
[136] S. Wang, S. Feng, J. Liang, Q. Su, F. Zhao, H. Song, M. Zheng, Q. Sun, Z. Song, X. Jia, J. Yang, Y. Li, J. Liao, R. Li, X. Sun, *Adv. Energy Mater.* **2021**, *11*, 2003314.
[137] D. Yang, Z. Liang, C. Zhang, J. J. Biendicho, M. Botifoll, M. C. Spadaro, Q. Chen, M. Li, A. Ramon, A. O. Moghaddam, J. Llorca, J. Wang, J. R. Morante, J. Arbiol, S. L. Chou, A. Cabot, *Adv. Energy Mater.* **2021**, *11*, 2101250.
[138] T. Zhu, Y. Sha, H. Zhang, Y. Huang, X. Gao, M. Ling, Z. Lin, *ACS Appl. Mater. Interfaces* **2021**, *13*, 20153.
[139] G. Liu, Q. Zeng, X. Hua, Z. Fan, X. Lv, W. Zhang, Z. Zhang, *Mater. Chem. Phys.* **2022**, *277*, 125578.
[140] R. Chu, T. T. Nguyen, Y. Bai, N. H. Kim, J. H. Lee, *Adv. Energy Mater.* **2022**, *12*, 2102805.
[141] J. Pu, W. Gong, Z. Shen, L. Wang, Y. Yao, G. Hong, *Adv. Sci.* **2022**, *9*, 2104375.
[142] D.-Q. Cai, J.-L. Yang, T. Liu, S.-X. Zhao, G. Cao, *Nano Energy* **2021**, *89*, 106452.
[143] J. L. Yang, D. Q. Cai, X. G. Hao, L. Huang, Q. Lin, X. T. Zeng, S. X. Zhao, W. Lv, *ACS Nano* **2021**, *15*, 11491.
[144] Z. Cao, J. Guo, S. Chen, Z. Zhang, Z. Shi, Y. Yin, M. Yang, X. Wang, S. Yang, *J. Mater. Chem. A* **2021**, *9*, 21867.
[145] D. Lei, W. Shang, X. Zhang, Y. Li, S. Qiao, Y. Zhong, X. Deng, X. Shi, Q. Zhang, C. Hao, X. Song, F. Zhang, *ACS Nano* **2021**, *15*, 20478.
[146] W. Wang, L. Huai, S. Wu, J. Shan, J. Zhu, Z. Liu, L. Yue, Y. Li, *ACS Nano* **2021**, *15*, 11619.
[147] W. Yao, W. Zheng, J. Xu, C. Tian, K. Han, W. Sun, S. Xiao, *ACS Nano* **2021**, *15*, 7114.
[148] B. Qin, Y. Cai, P. Wang, Y. Zou, J. Cao, J. Qi, *Energy Storage Mater.* **2022**, *47*, 345.
[149] Z. Shi, M. Li, J. Sun, Z. Chen, *Adv. Energy Mater.* **2021**, *11*, 2100332.
[150] H. Lin, S. Zhang, T. Zhang, H. Ye, Q. Yao, G. W. Zheng, J. Y. Lee, *Adv. Energy Mater.* **2018**, *8*, 1801868.
[151] Y. Wang, R. Zhang, J. Chen, H. Wu, S. Lu, K. Wang, H. Li, C. J. Harris, K. Xi, R. V. Kumar, S. Ding, *Adv. Energy Mater.* **2019**, *9*, 1900953.
[152] H. Zhang, L. Yang, P. Zhang, C. Lu, D. Sha, B. Yan, W. He, M. Zhou, W. Zhang, L. Pan, Z. Sun, *Adv. Mater.* **2021**, *33*, 2008447.
[153] K. Lv, P. Wang, C. Wang, Z. Shen, Z. Lu, H. Zhang, M. Zheng, P. He, H. Zhou, *Small* **2020**, *16*, 2000870.
[154] J. Wang, L. Jia, H. Liu, C. Wang, J. Zhong, Q. Xiao, J. Yang, S. Duan, K. Feng, N. Liu, W. Duan, H. Lin, Y. Zhang, *ACS Appl. Mater. Interfaces* **2020**, *12*, 12727.
[155] W. Wang, Y. Zhao, Y. Zhang, J. Wang, G. Cui, M. Li, Z. Bakenov, X. Wang, *ACS Appl. Mater. Interfaces* **2020**, *12*, 12763.
[156] L. Niu, T. Wu, D. Zhou, J. Qi, Z. Xiao, *Energy Storage Mater.* **2022**, *45*, 840.
[157] K. Zou, X. Chen, W. Jing, X. Dai, P. Wang, Y. Liu, R. Qiao, M. Shi, Y. Chen, J. Sun, Y. Liu, *Energy Storage Mater.* **2022**, *48*, 133.
[158] K. Zou, T. Zhou, Y. Chen, X. Xiong, W. Jing, X. Dai, M. Shi, N. Li, J. Sun, S. Zhang, C. Zhang, Y. Liu, Z. Guo, *Adv. Energy Mater.* **2022**, *12*, 2103981.
[159] Q. Zhang, X. Zhang, M. Li, J. Liu, Y. Wu, *Appl. Surf. Sci.* **2019**, *487*, 452.
[160] H. Lin, S. Zhang, T. Zhang, S. Cao, H. Ye, Q. Yao, G. W. Zheng, J. Y. Lee, *ACS Nano* **2019**, *13*, 7073.

[161] H.-E. Wang, X. Li, N. Qin, X. Zhao, H. Cheng, G. Cao, W. Zhang, *J. Mater. Chem. A* **2019**, *7*, 12068.
[162] Y. Tian, G. Li, Y. Zhang, D. Luo, X. Wang, Y. Zhao, H. Liu, P. Ji, X. Du, J. Li, Z. Chen, *Adv. Mater.* **2020**, *32*, 1904876.
[163] M. Wang, Z. Sun, H. Ci, Z. Shi, L. Shen, C. Wei, Y. Ding, X. Yang, J. Sun, *Angew. Chem., Int. Ed.* **2021**, *60*, 24558.
[164] H.-J. Li, K. Xi, W. Wang, S. Liu, G.-R. Li, X.-P. Gao, *Energy Storage Mater.* **2022**, *45*, 1229.
[165] Y. Boyjoo, H. Shi, E. Olsson, Q. Cai, Z. S. Wu, J. Liu, G. Q. Lu, *Adv. Energy Mater.* **2020**, *10*, 2000651.
[166] R. Sun, Y. Bai, Z. Bai, L. Peng, M. Luo, M. Qu, Y. Gao, Z. Wang, W. Sun, K. Sun, *Adv. Energy Mater.* **2022**, *12*, 2102739.
[167] W. Yao, C. Tian, C. Yang, J. Xu, Y. Meng, I. Manke, N. Chen, Z. Wu, L. Zhan, Y. Wang, R. Chen, *Adv. Mater.* **2022**, *34*, 2106370.
[168] R. Meng, Q. Du, N. Zhong, X. Zhou, S. Liu, S. Yin, X. Liang, *Adv. Energy Mater.* **2021**, *11*, 2102819.
[169] X. Wang, J. Han, C. Luo, B. Zhang, J. Ma, Z. Li, Y. B. He, Q. H. Yang, F. Kang, W. Lv, *Small* **2021**, *17*, 2101538.
[170] C. Zhang, R. Du, J. J. Biendicho, M. Yi, K. Xiao, D. Yang, T. Zhang, X. Wang, J. Arbiol, J. Llorca, Y. Zhou, J. R. Morante, A. Cabot, *Adv. Energy Mater.* **2021**, *11*, 2100432.
[171] B. Yu, F. Ma, D. Chen, K. Srinivas, X. Zhang, X. Wang, B. Wang, W. Zhang, Z. Wang, W. He, Y. Chen, *J. Mater. Sci. Technol.* **2021**, *90*, 37.
[172] P. Zuo, J. Hua, M. He, H. Zhang, Z. Qian, Y. Ma, C. Du, X. Cheng, Y. Gao, G. Yin, *J. Mater. Chem. A* **2017**, *5*, 10936.
[173] R. Pongilat, K. Nallathamby, *ACS Appl. Mater. Interfaces* **2018**, *10*, 38853.
[174] M. Yu, S. Zhou, Z. Wang, Y. Wang, N. Zhang, S. Wang, J. Zhao, J. Qiu, *Energy Storage Mater.* **2019**, *20*, 98.
[175] P. Zeng, J. Peng, H. Yu, X. Zhou, K. Wang, J. Liu, Z. Zhou, M. Chen, C. Miao, X. Guo, B. Chang, X. Wang, *Carbon* **2022**, *192*, 418.
[176] D. Fang, Y. Wang, C. Qian, X. Liu, X. Wang, S. Chen, S. Zhang, *Adv. Funct. Mater.* **2019**, *29*, 1900875.
[177] J. Li, C. Chen, Y. Chen, Z. Li, W. Xie, X. Zhang, M. Shao, M. Wei, *Adv. Energy Mater.* **2019**, *9*, 1901935.
[178] J. Qian, F. Wang, Y. Li, S. Wang, Y. Zhao, W. Li, Y. Xing, L. Deng, Q. Sun, L. Li, F. Wu, R. Chen, *Adv. Funct. Mater.* **2020**, *30*, 2000742.
[179] R. Wang, J. Yang, X. Chen, Y. Zhao, W. Zhao, G. Qian, S. Li, Y. Xiao, H. Chen, Y. Ye, G. Zhou, F. Pan, *Adv. Energy Mater.* **2020**, *10*, 1903550.
[180] D. Wang, K. Ma, J. Hao, W. Zhang, C. Wang, C. Xu, H. Shi, Z. Ji, X. Yan, Y. Gu, *Nano Energy* **2021**, *89*, 106426.
[181] H. Ye, J. Sun, S. Zhang, H. Lin, T. Zhang, Q. Yao, J. Y. Lee, *ACS Nano* **2019**, *13*, 14208.
[182] Y. Li, W. Wang, B. Zhang, L. Fu, M. Wan, G. Li, Z. Cai, S. Tu, X. Duan, Z. W. Seh, J. Jiang, Y. Sun, *Nano Lett.* **2021**, *21*, 6656.
[183] J. Li, Y. Chen, S. Zhang, W. Xie, S. M. Xu, G. Wang, M. Shao, *ACS Appl. Mater. Interfaces* **2020**, *12*, 49519.
[184] M. Wang, X. Zhou, X. Cai, H. Wang, Y. Fang, X. Zhong, *J. Energy Chem.* **2020**, *50*, 106.
[185] B. Fan, D. Zhao, W. Xu, Q. Wu, W. Zhou, W. Lei, X. Liang, L. Li, *Electrochim. Acta* **2021**, *383*, 138371.
[186] L. Su, J. Zhang, Y. Chen, W. Yang, J. Wang, Z. Ma, G. Shao, G. Wang, *Nano Energy* **2021**, *85*, 105981.
[187] C. Yuan, P. Zeng, C. Cheng, T. Yan, G. Liu, W. Wang, J. Hu, X. Li, J. Zhu, L. Zhang, *CCS Chem.* **2021**, *3*, 2826.
[188] T. Zhao, J. Chen, M. Yuan, K. Dai, J. Zhang, S. Li, H. He, Z. Liu, G. Zhang, *J. Mater. Chem. A* **2021**, *9*, 7566.
[189] K. Zhang, W. Cai, Y. Liu, G. Hu, W. Hu, Y. Kong, X. Zhang, L. Wang, G. Li, *Chem. Eng. J.* **2022**, *427*, 130897.
[190] H. Li, L. Fei, R. Zhang, S. Yu, Y. Zhang, L. Shu, Y. Li, Y. Wang, *J. Energy Chem.* **2020**, *49*, 339.
[191] Z. Shi, Z. Sun, J. Cai, Z. Fan, J. Jin, M. Wang, J. Sun, *Adv. Funct. Mater.* **2021**, *31*, 2006798.
[192] X. Cao, M. Zhang, F. Zhu, X. Zhang, *J. Alloys Compd.* **2022**, *895*, 162609.
[193] N. Gao, Y. Zhang, C. Chen, B. Li, W. Li, H. Lu, L. Yu, S. Zheng, B. Wang, *J. Mater. Chem. A* **2022**, *10*, 8378.
[194] P. Zeng, C. Liu, X. Zhao, C. Yuan, Y. Chen, H. Lin, L. Zhang, *ACS Nano* **2020**, *14*, 11558.
[195] Y. Hu, C. Cheng, T. Yan, G. Liu, C. Yuan, Y. Yan, Z. Gu, P. Zeng, L. Zheng, J. Zhang, L. Zhang, *Chem. Eng. J.* **2021**, *421*, 129997.
[196] Z. Qiao, F. Zhou, Q. Zhang, F. Pei, H. Zheng, W. Xu, P. Liu, Y. Ma, Q. Xie, L. Wang, X. Fang, D.-L. Peng, *Energy Storage Mater.* **2019**, *23*, 62.
[197] J. He, A. Bhargav, A. Manthiram, *ACS Nano* **2021**, *15*, 8583.
[198] H.-J. Zhou, X.-L. Zhang, M.-Y. Zou, S.-T. Gu, Y.-P. Cai, X.-J. Hong, *ACS Appl. Energy Mater.* **2021**, *4*, 13183.
[199] H. Xu, R. Hu, Y. Zhang, H. Yan, Q. Zhu, J. Shang, S. Yang, B. Li, *Energy Storage Mater.* **2021**, *43*, 212.
[200] F. Wang, J. Li, J. Zhao, Y. Yang, C. Su, Y. L. Zhong, Q.-H. Yang, J. Lu, *ACS Mater. Lett.* **2020**, *2*, 1450.
[201] Z. Liu, L. Zhou, Q. Ge, R. Chen, M. Ni, W. Utetiwabo, X. Zhang, W. Yang, *ACS Appl. Mater. Interfaces* **2018**, *10*, 19311.
[202] J. Wang, L. Jia, J. Zhong, Q. Xiao, C. Wang, K. Zang, H. Liu, H. Zheng, J. Luo, J. Yang, H. Fan, W. Duan, Y. Wu, H. Lin, Y. Zhang, *Energy Storage Mater.* **2019**, *18*, 246.
[203] H. Ye, J. Sun, S. Zhang, T. Zhang, Y. Zhao, C. Song, Q. Yao, J. Y. Lee, *Chem. Eng. J.* **2021**, *410*, 128284.
[204] Z. Du, X. Chen, W. Hu, C. Chuang, S. Xie, A. Hu, W. Yan, X. Kong, X. Wu, H. Ji, L.-J. Wan, *J. Am. Chem. Soc.* **2019**, *141*, 3977.
[205] D. Fang, P. Sun, S. Huang, Y. Shang, X. Li, D. Yan, Y. V. Lim, C.-Y. Su, B.-J. Su, J.-Y. Juang, H. Y. Yang, *ACS Mater. Lett.* **2022**, *4*, 1.
[206] Z. Wang, J. Shen, X. Xu, J. Yuan, S. Zuo, Z. Liu, D. Zhang, J. Liu, *Small* **2022**, *18*, 2106640.
[207] C. Wang, H. Song, C. Yu, Z. Ullah, Z. Guan, R. Chu, Y. Zhang, L. Zhao, Q. Li, L. Liu, *J. Mater. Chem. A* **2020**, *8*, 3421.
[208] C. Lu, Y. Chen, Y. Yang, X. Chen, *Nano Lett.* **2020**, *20*, 5522.
[209] H. Zhao, B. Tian, C. Su, Y. Li, *ACS Appl. Mater. Interfaces* **2021**, *13*, 7171.
[210] C. Ma, Y. Zhang, Y. Feng, N. Wang, L. Zhou, C. Liang, L. Chen, Y. Lai, X. Ji, C. Yan, W. Wei, *Adv. Mater.* **2021**, *33*, 2100171.
[211] Y. Zhang, J. Liu, J. Wang, Y. Zhao, D. Luo, A. Yu, X. Wang, Z. Chen, *Angew. Chem., Int. Ed.* **2021**, *60*, 26622.
[212] Y. Wang, D. Adekoya, J. Sun, T. Tang, H. Qiu, L. Xu, S. Zhang, Y. Hou, *Adv. Funct. Mater.* **2019**, *29*, 1807485.
[213] Y. Qiu, L. Fan, M. Wang, X. Yin, X. Wu, X. Sun, D. Tian, B. Guan, D. Tang, N. Zhang, *ACS Nano* **2020**, *14*, 16105.
[214] J. Wang, W. Qiu, G. Li, J. Liu, D. Luo, Y. Zhang, Y. Zhao, G. Zhou, L. Shui, X. Wang, Z. Chen, *Energy Storage Mater.* **2022**, *46*, 269.
[215] Y. Li, G. Chen, J. Mou, Y. Liu, S. Xue, T. Tan, W. Zhong, Q. Deng, T. Li, J. Hu, C. Yang, K. Huang, M. Liu, *Energy Storage Mater.* **2020**, *28*, 196.
[216] Y. Li, P. Zhou, H. Li, T. Gao, L. Zhou, Y. Zhang, N. Xiao, Z. Xia, L. Wang, Q. Zhang, L. Gu, S. Guo, *Small Methods* **2020**, *4*, 1900701.
[217] Q. Lin, B. Ding, S. Chen, P. Li, Z. Li, Y. Shi, H. Dou, X. Zhang, *ACS Appl. Energy Mater.* **2020**, *3*, 11206.
[218] T. Huang, Y. Sun, J. Wu, J. Jin, C. Wei, Z. Shi, M. Wang, J. Cai, X. T. An, P. Wang, C. Su, Y. Y. Li, J. Sun, *ACS Nano* **2021**, *15*, 14105.
[219] J. Xie, B. Q. Li, H. J. Peng, Y. W. Song, M. Zhao, X. Chen, Q. Zhang, J. Q. Huang, *Adv. Mater.* **2019**, *31*, 1903813.
[220] Y. Li, J. Wu, B. Zhang, W. Wang, G. Zhang, Z. W. Seh, N. Zhang, J. Sun, L. Huang, J. Jiang, J. Zhou, Y. Sun, *Energy Storage Mater.* **2020**, *30*, 250.
[221] R. Wang, R. Wu, C. Ding, Z. Chen, H. Xu, Y. Liu, J. Zhang, Y. Ha, B. Fei, H. Pan, *Nano-Micro Lett.* **2021**, *13*, 151.
[222] L. Zhang, D. Liu, Z. Muhammad, F. Wan, W. Xie, Y. Wang, L. Song, Z. Niu, J. Chen, *Adv. Mater.* **2019**, *31*, 1903955.
[223] S. Zhang, X. Ao, J. Huang, B. Wei, Y. Zhai, D. Zhai, W. Deng, C. Su, D. Wang, Y. Li, *Nano Lett.* **2021**, *21*, 9691.

[224] H. Shi, X. Ren, J. Lu, C. Dong, J. Liu, Q. Yang, J. Chen, Z. S. Wu, *Adv. Energy Mater.* **2020**, *10*, 2002271.
[225] C. L. Song, Z. H. Li, L. Y. Ma, M. Z. Li, S. Huang, X. J. Hong, Y. P. Cai, Y. Q. Lan, *ACS Nano* **2021**, *15*, 13436.
[226] R. Wang, R. Wu, X. Yan, D. Liu, P. Guo, W. Li, H. Pan, *Adv. Funct. Mater.* **2022**, *32*, 2200424.
[227] F. Ma, Y. Wan, X. Wang, X. Wang, J. Liang, Z. Miao, T. Wang, C. Ma, G. Lu, J. Han, Y. Huang, Q. Li, *ACS Nano* **2020**, *14*, 10115.
[228] G. Zhou, S. Zhao, T. Wang, S. Z. Yang, B. Johannessen, H. Chen, C. Liu, Y. Ye, Y. Wu, Y. Peng, C. Liu, S. P. Jiang, Q. Zhang, Y. Cui, *Nano Lett.* **2020**, *20*, 1252.
[229] P. Wang, B. Xi, Z. Zhang, M. Huang, J. Feng, S. Xiong, *Angew. Chem., Int. Ed.* **2021**, *60*, 15563.
[230] Y. Li, T. Gao, D. Ni, Y. Zhou, M. Yousaf, Z. Guo, J. Zhou, P. Zhou, Q. Wang, S. Guo, *Adv. Mater.* **2022**, *34*, 2107638.
[231] S. Xie, X. Chen, C. Wang, Y. R. Lu, T. S. Chan, C. H. Chuang, J. Zhang, W. Yan, S. Jin, H. Jin, X. Wu, H. Ji, *Small* **2022**, *18*, 2200395.
[232] E. I. Andritsos, C. Lekakou, Q. Cai, *J. Phys. Chem. C* **2021**, *125*, 18108.
[233] Z. Han, S. Zhao, J. Xiao, X. Zhong, J. Sheng, W. Lv, Q. Zhang, G. Zhou, H. M. Cheng, *Adv. Mater.* **2021**, *33*, 2105947.
[234] J. Lei, X. X. Fan, T. Liu, P. Xu, Q. Hou, K. Li, R. M. Yuan, M. S. Zheng, Q. F. Dong, J. J. Chen, *Nat. Commun.* **2022**, *13*, 202.
[235] Y. Liang, Y. Li, H. Wang, J. Zhou, J. Wang, T. Regier, H. Dai, *Nat. Mater.* **2011**, *10*, 780.
[236] D.-C. Xia, L. Zhou, S. Qiao, Y. Zhang, D. Tang, J. Liu, H. Huang, Y. Liu, Z. Kang, *Mater. Res. Bull.* **2016**, *74*, 441.
[237] N. Meethong, H. Y. S. Huang, S. A. Speakman, W. C. Carter, Y. M. Chiang, *Adv. Funct. Mater.* **2007**, *17*, 1115.
[238] B. Yang, H. Jiang, Y. Zhou, Z. Liang, T. Zhao, Y. C. Lu, *ACS Appl. Mater. Interfaces* **2019**, *11*, 25940.
[239] L. Zhou, H. Li, Y. Zhang, M. Jiang, D. L. Danilov, R.-A. Eichel, P. H. L. Notten, *Mater. Today Commun.* **2021**, *26*, 102133.
[240] B. Wang, L. Wang, B. Zhang, S. Zeng, F. Tian, J. Dou, Y. Qian, L. Xu, *ACS Nano* **2022**, *16*, 4947.
[241] S. Waluś, C. Barchasz, R. Bouchet, F. Alloin, *Electrochim. Acta* **2020**, *359*, 136944.
[242] C. X. Zhao, X. Y. Li, M. Zhao, Z. X. Chen, Y. W. Song, W. J. Chen, J. N. Liu, B. Wang, X. Q. Zhang, C. M. Chen, B. Q. Li, J. Q. Huang, Q. Zhang, *J. Am. Chem. Soc.* **2021**, *143*, 19865.
[243] Z. Wang, M. Feng, H. Sun, G. Li, Q. Fu, H. Li, J. Liu, L. Sun, A. Mauger, C. M. Julien, H. Xie, Z. Chen, *Nano Energy* **2019**, *59*, 390.
[244] E. Zhao, K. Nie, X. Yu, Y. S. Hu, F. Wang, J. Xiao, H. Li, X. Huang, *Adv. Funct. Mater.* **2018**, *28*, 1707543.
[245] J. Conder, R. Bouchet, S. Trabesinger, C. Marino, L. Gubler, C. Villevieille, *Nat. Energy* **2017**, *2*, 17069.
[246] J. Nelson, S. Misra, Y. Yang, A. Jackson, Y. Liu, H. Wang, H. Dai, J. C. Andrews, Y. Cui, M. F. Toney, *J. Am. Chem. Soc.* **2012**, *134*, 6337.
[247] Y. Wang, Y. Huang, W. Wang, C. Huang, Z. Yu, H. Zhang, J. Sun, A. Wang, K. Yuan, *Electrochim. Acta* **2009**, *54*, 4062.
[248] H. S. Ryu, Z. Guo, H. J. Ahn, G. B. Cho, H. Liu, *J. Power Sources* **2009**, *189*, 1179.
[249] L. Luo, J. Li, H. Yaghoobnejad Asl, A. Manthiram, *ACS Energy Lett.* **2020**, *5*, 1177.
[250] Q. Zhang, R. Gao, Z. Li, B. Zhou, A. Tang, J. Wang, J.-J. Zou, H. Yang, *Small* **2022**, *18*, 2105661.
[251] M. Ding, S. Huang, Y. Wang, J. Hu, M. E. Pam, S. Fan, Y. Shi, Q. Ge, H. Y. Yang, *J. Mater. Chem. A* **2019**, *7*, 25078.
[252] W. Zhao, Y. Lei, Y. Zhu, Q. Wang, F. Zhang, X. Dong, H. N. Alshareef, *Nano Energy* **2021**, *86*, 106120.
[253] S. Huang, Y. Wang, J. Hu, Y. V. Lim, D. Kong, Y. Zheng, M. Ding, M. E. Pam, H. Y. Yang, *ACS Nano* **2018**, *12*, 9504.
[254] G. Peng, C. Hai, C. Sun, Y. Zhou, Y. Sun, Y. Shen, X. Li, G. Zhang, J. Zeng, S. Dong, *ACS Appl. Mater. Interfaces* **2021**, *13*, 55007.
[255] H. Li, S. Ma, J. Li, F. Liu, H. Zhou, Z. Huang, S. Jiao, Y. Kuang, *Energy Storage Mater.* **2020**, *26*, 203.
[256] B. Wang, L. Wang, B. Zhang, Z. Kong, S. Zeng, M. Zhao, Y. Qian, L. Xu, *Energy Storage Mater.* **2022**, *45*, 130.
[257] J.-J. Chen, R.-M. Yuan, J.-M. Feng, Q. Zhang, J.-X. Huang, G. Fu, M.-S. Zheng, B. Ren, Q.-F. Dong, *Chem. Mater.* **2015**, *27*, 2048.
[258] Y. He, Y. Qiao, Z. Chang, X. Cao, M. Jia, P. He, H. Zhou, *Angew. Chem., Int. Ed.* **2019**, *58*, 11774.
[259] L. Xue, Y. Li, A. Hu, M. Zhou, W. Chen, T. Lei, Y. Yan, J. Huang, C. Yang, X. Wang, Y. Hu, J. Xiong, *Small Struct.* **2022**, *3*, 2100170.
[260] J. Hannauer, J. Scheers, J. Fullenwarth, B. Fraisse, L. Stievano, P. Johansson, *ChemPhysChem* **2015**, *16*, 2709.
[261] B. Yu, A. Huang, K. Srinivas, X. Zhang, F. Ma, X. Wang, D. Chen, B. Wang, W. Zhang, Z. Wang, J. He, Y. Chen, *ACS Nano* **2021**, *15*, 13279.
[262] Y. Yan, C. Cheng, L. Zhang, Y. Li, J. Lu, *Adv. Energy Mater.* **2019**, *9*, 1900148.
[263] M. Cuisinier, P.-E. Cabelguen, S. Evers, G. He, M. Kolbeck, A. Garsuch, T. Bolin, M. Balasubramanian, L. F. Nazar, *J. Phys. Chem. Lett.* **2013**, *4*, 3227.
[264] K. H. Wujcik, T. A. Pascal, C. D. Pemmaraju, D. Devaux, W. C. Stolte, N. P. Balsara, D. Prendergast, *Adv. Energy Mater.* **2015**, *5*, 1500285.
[265] R. Dominko, A. Vizintin, G. Aquilanti, L. Stievano, M. J. Helen, A. R. Munnangi, M. Fichtner, I. Arcon, *J. Electrochem. Soc.* **2017**, *165*, A5014.
[266] E. Zhao, J. Wang, F. Li, Z. Jiang, X. Q. Yang, F. Wang, H. Li, X. Yu, *Chem. Commun.* **2019**, *55*, 4993.
[267] L. Jia, J. Wang, S. Ren, G. Ren, X. Jin, L. Kao, X. Feng, F. Yang, Q. Wang, L. Pan, Q. Li, Y. s. Liu, Y. Wu, G. Liu, J. Feng, S. Fan, Y. Ye, J. Guo, Y. Zhang, *Energy Environ. Mater.* **2020**, *4*, 222.
[268] C. Zech, P. Hönicke, Y. Kayser, S. Risse, O. Grätz, M. Stamm, B. Beckhoff, *J. Mater. Chem. A* **2021**, *9*, 10231.
[269] X. Gao, X. Yang, M. Li, Q. Sun, J. Liang, J. Luo, J. Wang, W. Li, J. Liang, Y. Liu, S. Wang, Y. Hu, Q. Xiao, R. Li, T.-K. Sham, X. Sun, *Adv. Funct. Mater.* **2019**, *29*, 1806724.
[270] Y. Diao, K. Xie, S. Xiong, X. Hong, *J. Electrochem. Soc.* **2012**, *159*, A421.
[271] D. Zheng, X. Zhang, C. Li, M. E. McKinnon, R. G. Sadok, D. Qu, X. Yu, H.-S. Lee, X.-Q. Yang, D. Qu, *J. Electrochem. Soc.* **2014**, *162*, A203.
[272] D. Zheng, D. Qu, X.-Q. Yang, X. Yu, H.-S. Lee, D. Qu, *Adv. Energy Mater.* **2015**, *5*, 1401888.
[273] D. Zheng, D. Qu, *J. Electrochem. Soc.* **2014**, *161*, A1164.
[274] D. Zheng, D. Qiu, T. Ding, D. Qu, *Ind. Eng. Chem. Res.* **2022**, *61*, 3055.
[275] Q. He, B. Yu, Z. Li, Y. Zhao, *Energy Environ. Mater.* **2019**, *2*, 264.
[276] S. Feng, Z. H. Fu, X. Chen, Q. Zhang, *InfoMat* **2022**, *4*, e12304.
[277] J. K. Nørskov, J. Rossmeisl, A. Logadottir, L. Lindqvist, J. R. Kitchin, T. Bligaard, H. Jónsson, *J. Phys. Chem. B* **2004**, *108*, 17886.
[278] C. Zhao, G. L. Xu, Z. Yu, L. Zhang, I. Hwang, Y. X. Mo, Y. Ren, L. Cheng, C. J. Sun, Y. Ren, X. Zuo, J. T. Li, S. G. Sun, K. Amine, T. Zhao, *Nat. Nanotechnol.* **2021**, *16*, 166.
[279] J. Liu, L. Zhu, Z. Shen, M. Zhang, T. Han, H. Zhang, *ACS Appl. Energy Mater.* **2021**, *4*, 10998.
[280] X. Tao, J. Wang, C. Liu, H. Wang, H. Yao, G. Zheng, Z. W. Seh, Q. Cai, W. Li, G. Zhou, C. Zu, Y. Cui, *Nat. Commun.* **2016**, *7*, 11203.
[281] Q. Pang, X. Liang, C. Kwok, L. F. Nazar, *J. Electrochem. Soc.* **2015**, *162*, A2567.
[282] Q. Pang, D. Kundu, L. F. Nazar, *Mater. Horiz.* **2016**, *3*, 130.
[283] Q. Zhang, Y. Wang, Z. W. Seh, Z. Fu, R. Zhang, Y. Cui, *Nano Lett.* **2015**, *15*, 3780.
[284] X. Song, D. Tian, Y. Qiu, X. Sun, B. Jiang, C. Zhao, Y. Zhang, L. Fan, N. Zhang, *Adv. Funct. Mater.* **2022**, *32*, 2109413.

Lei Zhou received his Ph.D. degree from the Eindhoven University of Technology (TU/e), The Netherlands in 2021. He served as a Guest Researcher at the Institute of Energy and Climate Research (IEK-9), Forschungszentrum Jülich, Germany from 2017 to 2021. After that, he joined the Jiangsu University, China as a Lecturer. His research interests focus on advanced battery technologies, battery failure analysis, and modeling of battery systems.

Dmitri L. Danilov, Ph.D., has a background in Physics and Mathematics and obtained his MSc at the Saint-Petersburg University in 1993. In 2003, he got Ph.D. degree from the University of Tilburg. In 2002, he joined the Eurandom Institute at TU/e, being involved in various national and international research projects. His current research interests include mathematical modeling of complex electrochemical systems, including Li-ion and NiMH batteries, aging and degradation processes, thin-film batteries, and advanced characterization methods. Starting 2017, he joined the IEK-9 in the Forschungszentrum Jülich. He has published as author and coauthor more than 70 papers and book contributions.

Junfeng Wang is the Dean of School of Energy and Power Engineering of the Jiangsu University. He received his Ph.D. degree from the Jiangsu University in 2002. His main research fields are charged multiphase flow and its applications in engineering including new energy, environment protection, energy saving, etc. He is also engaged in the basic theory studies on electrostatic atomization, multiphase flow, non-Newtonian fluids, and spray technology in industry and agriculture.

Peter H. L. Notten joined the Philips Research Laboratories (Eindhoven, The Netherlands) from 1975 to 2010. He received his Ph.D. degree from the Eindhoven University in 1989. He focuses on energy storage research, including hydrogen and lithium storage materials, new battery technologies, modeling electrochemical systems, and design of battery-management algorithms. In 2000, he was appointed as Professor at TU/e heading the group Energy Materials and Devices. In 2014, he has been appointed as International Adjunct Faculty at the Amrita University, Coimbatore (India), as Group Leader at the Forschungszentrum Jülich, and in 2018 as Honorary Professor at the University of Technology Sydney.